A Novel Sensory System for the 3D Surface Profiling of Small Complex Objects

by

Veronica E. Marin

A thesis submitted in conformity with the requirements
for the degree of Doctor of Philosophy

Mechanical and Industrial Engineering
University of Toronto

A Novel Sensory System for the 3D Surface Profiling of Small Complex Objects

Veronica E. Marin

Doctor of Philosophy

Mechanical and Industrial Engineering
University of Toronto

2016

Abstract

Structured-light (SL) techniques are noncontact approaches for measuring 3D complex objects in various applications including robotics, manufacturing and reverse engineering. An SL system is based on a triangulation configuration between the object of interest, a projector and one or more cameras. The 3D surface profile of the object is obtained from the deformation of light patterns projected onto the object. The performance of SL systems is determined by the hardware components, their triangulation configuration and the patterns used. This thesis focuses on developing, implementing and evaluating SL systems for measuring small (0.5 – 100 mm) complex objects. The contributions of this thesis are: 1) a design methodology for determining the optimal triangulation configuration to reduce reconstruction errors, and to maximize unique pixel-to-pixel correspondences and coverage of the measurement volume, 2) a design methodology for optimizing the pattern sequence to minimize random noise in 3D reconstruction, 3) design methodologies for SL system for micro-scale measurements using image focus fusion to increase the effective measurement volume, and 4) a novel calibration procedure for SL systems using robust regression models with the lowest predictive errors. Experiments are conducted with a variety of micro-scale objects to validate the effectiveness of the proposed methodologies for designing SL systems for micro-scale measurements.

Acknowledgments

I would like to express my deepest gratitude to my supervisor, Professor Nejat, who has provided me with a wonderful opportunity to work in such a complex project in my PhD years and to share my work with the community in conferences and journals. Thank you, Professor, for your time and advice in every one of our meetings discussing my progress and the challenges of making a novel sensor using cutting-edge knowledge, skills and technology. I also would like to thank you for the wonderful opportunity of letting me work with, teach and supervise undergraduate and graduate students that collaborated in my project.

I would also like to express my gratitude to Professor Mills and Professor Benhabib who always provided me with insightful feedback in every meeting and for their continuous support for this project. I would like to specially thank Professor Benhabib for letting us use the facilities of his lab for calibrating the first prototypes of the SL system.

I would like to thank NSERC through the CANRIMT project for funding and making this project possible. I also thank all the CANRIMT members for their support, especially to: Hay Azulay, Masih Mahmoodi, Adam Lee, Fu Shao, Mario Luces, Wayne Chang, Sean Fung.

A special gratitude I give to all the summer and undergraduate students for their contribution in automating the data acquisition and integrating the hardware components, especially to Yuma Tsuboi, Evgeny Nuger, Sanjana Seerala, Andrew Louis, Simon Han, Michelle Lee, Eric DuHun, Eugene Du and Yisap Shiwakoti. A special thanks goes to my graduate team mates, Wayne Chang and Pieter Luitjens, whose contribution in integrating the hardware components of microscope lenses and image focus fusion implementation, helped me to develop the SL system for micro-scale measurements. My thanks will also go to my lab mates at the Autonomous Systems and Biomechatronics Laboratory.

Most importantly, I would like to express my greatest gratitude to God, my parents, my husband, and my entire family and friends for always supporting me to complete this project. I would like to give my special thanks to my husband and my parents for their unconditional support during these past five years, their encouragement, love and understanding helped me to achieve this goal.

Table of Contents

List of Tables

List of Figures

List of Appendices

Chapter 1
Introduction

This thesis presents the concept design, development and implementation of the design methodologies needed to develop and integrate sensory systems for measuring complex objects. In this chapter the motivation, research objective and challenges are described.

1.1 Motivation

In recent years, there has been significant interest in the use of accurate non-contact sensory systems for measuring a variety of different 3D objects [1-2]. Traditional contact-based technologies such as Coordinate Measurement Machines (CMMs) are being increasingly replaced by optical, non-contact methods, which can provide higher measurement speeds than CMMs [3]. Non-contact sensing systems have been used in a wide variety of application domains such as manufacturing [4], reverse engineering [5-6], product inspection [7-8], optics [9], biomedical [10], and robot navigation [11]. In these applications, non-contact 3D measurement techniques have played an important role in measuring objects made of brittle materials or deformable structures [12], with complex and discontinuous 3D surface profiles [7], in hostile environments [2], and/or providing fast 3D measurements for real-time applications [13]. Such non-contact techniques utilize various optical methods for 3D reconstruction, including time-of-flight [14], stereo vision [15], laser stripe scanning [16] and structured-light [17]. Among these methods, structured-light (SL) techniques have been emerging as a popular method for 3D measurements due to several advantages including: 1) providing full-field measurements of the entire surface of an object in one acquisition without the need for scanning [1], 2) the ability to provide real-time and accurate measurements [18], and 3) the use of off-the-shelf hardware components [19].

SL sensing uses an active triangulation-based method that is widely used for visual inspection, object recognition, material characterization and recovering 3D shapes of objects [20]. In general, an SL system consists of one or more cameras and active light sources. These light sources, or projectors, illuminate the object of interest with a known light spot, line or pattern while the cameras capture the pattern deformation caused by the object surface profile. Due to their fast measurement speed, low cost, high-precision surface metrology capabilities, SL systems have been used for 3D off-line measurements of large complex objects [2, 4, 7]; and for off-line

measurements of flat MEMS objects [2, 18, 21]. In addition, the non-contact, non-destructive nature of SL systems makes them attractive for manufacturing inspection of objects. For example, in [2], 3D measurements obtained from various SL systems were reported for objects such as a thin-film sensor, a screw, a car door, among others, demonstrating the potential of SL technique for industrial applications. In [4], a pattern-based SL technique was used to obtain 3D profiles of large manufactured parts such as a car door and a windshield. In [7], accurate 3D surface profiles were obtained using black/white patterns for the accurate inspection of cylindrical specular industrial objects. In [18] and [22], discrete patterns were used to reconstruct the surface profile of MEMS parts such as micro-mirror array. Even though SL systems have been successfully implemented and applied to different applications, previous work has not presented yet theoretically sound guidelines or methodologies on how to design such systems in order to achieve the highest measurement accuracy for small complex objects.

The accuracy of an SL system is influenced significantly by the characteristics of the projection and capturing hardware components, and by the triangulation configuration between these components and the measured object. In addition, the pattern design of the SL system determines the performance of the technique in terms of resolution, accuracy, and efficiency. Therefore, SL systems need to be designed in terms of the hardware triangulation configuration and the structured-light patterns themselves in order to achieve the target measurement specifications.

1.1.1 SL System Configuration Design

Different approaches have been proposed in order to increase the accuracy of SL systems beyond the current state of the art. In [4], an improving system accuracy was suggested by designing application-specific black/white patterns to compensate measurement errors caused by surface texture and ambient light for inspection of an automotive pillar/door assembly. In [23], the effects of system calibration on accuracy were considered, and a linearized irradiance model was introduced to compensate for the non-linearity of the controllable light source. Using this proposed model, it was shown that the accuracy of depth reconstruction could be improved significantly. In [24], the effects of hardware geometric configurations were investigated by developing a set of analytical relationships of measurement errors based on triangulation geometry of a simple idealized SL system, with a planar geometric configuration between hardware components and an object of interest. Based on a qualitative parametric study, they concluded that the relative distance

and orientation of the imaging and projection components influence system error, the working depth of field and the overall sensory system size. Previous work showed that the measurement accuracy of a SL system is mainly determined by the characteristics of the projection and capture hardware, and by the triangulation configuration between the camera, projector and the object. Hence, the hardware setup needs to be carefully designed to achieve the desired resolution, precision, and target object size. However, no methodology has been proposed in the literature for designing SL system configuration for measuring objects with a desired accuracy.

1.1.2 Pattern Sequence Design for SL Systems

Different structured-light patterns have been proposed in order to increase the accuracy of SL systems beyond the current state of the art. In [17], the influence of the structured-light patterns on the reconstruction errors was investigated by comparing the implementation of discrete and continuous SL techniques, using the same SL hardware set-up and triangulation configuration, on measuring a known complex object and a flat plane. The comparison results showed that the accuracy and the measurement time of an SL system are a result of numerous factors including the number and type of the patterns used, the surface characteristics of the measured object and the number of 3D reconstruction points that are obtained. However, no design methodology has been proposed for optimizing the patterns to reduce the measurement errors.

1.1.3 Challenges in Designing a Novel SL System

Potential target applications of this thesis work include the fields of manufacturing, reverse engineering and product inspection of innovative small complex devices in the size range of 0.5 – 100 mm for biomedical, aerospace, optics and automotive applications. Since this size range encompasses commonly accepted definitions for micro, meso and macro scales, for simplicity in this thesis we will refer to these innovative devices as macro-scale objects and micro-scale objects, if their sizes are in the range of 10 – 100 mm and 0.10 – 10 mm, respectively. In order to measure complex [12], micro-scale objects, the size and the shape complexity of the objects impose certain requirements in the optical specifications of the SL system. In particular, the larger magnifications required to image 0.5 – 10 mm objects result in shallow depth of field for measuring the entire object in focus, while also making the system more sensitive to noise and vibrations. Hence, before an SL system can be used for reliable measurements of small complex objects, some technical challenges need to be addressed, regarding both the hardware and the software of the sensory

system: 1) determining the triangulation configuration of the hardware components, and 2) designing the light patterns to measure the target objects.

In [23-24], it was discussed that the accuracy of an SL system is highly dependent on the triangulation configuration of the hardware components. However, the triangulation configuration also affects the effective measurement volume, i.e., the region in the scene where both the camera and the projector are in focus. While the size of measurement volume is maximized by reducing the angle between the optical axes of the camera and projector, this reduces the accuracy of the system and increases its sensitivity to noise, since it goes against the working principle of the sensor, i.e., estimating depth using a triangulation. The design challenge lies on optimizing the system configuration to meet the stated requirements for both accuracy and measurement volume, given any arbitrary set of hardware components and its optical specifications.

In [17], both the accuracy and the speed of an SL system were defined to depend on the light patterns that are projected during measurement. In practice, this imposes restrictions in the number and type of patterns to be projected. The number of patterns that must be projected to measure an object is related to the measurement acquisition speed for a given frame rate. In addition, the type of patterns projected and the algorithms used to post-process them have also a significant effect on the computational requirements and, ultimately, on the accuracy and resolution of the sensor. Furthermore, for measuring small complex objects with surface discontinuities, the type of pattern and post-processing algorithms also affect the ability of the sensor to accurately resolve sharp object features, such as edges, holes and other discontinuities. From the design point of view, the challenge lies on designing a minimal set of light patterns that are able to measure complex objects with the required accuracy, and that can be post-processed with low computational cost.

In order to develop accurate SL systems for measuring small complex objects, these challenges need to be addressed. Hence, this thesis will address these challenges by developing novel design methodologies for SL systems with high accuracy using off-the-shelf hardware components.

1.2 Problem Statement and Thesis Objective

Accurate 3D object reconstruction has become essential to provide feedback for control and manufacturing processes of small complex objects. Structured-light systems provide a non-contact, compact approach to obtain high density and accurate measurements of objects at an

affordable cost. Recent hardware developments have made it possible to use the advantages of SL systems for real-time measurement of macro-scale complex objects [2, 4, 7] as well as simple objects at micro-scale [2, 18, 21]. However, current SL systems are not capable of obtaining the surface profile of small objects with a wide range of geometric surface complexities, such as propeller blades of a capsule endoscope [25], curvature of micro lenses [12], gears used in micro air vehicles [26]. Hence, the objective of this thesis is to develop an overall novel design methodology for the development of SL sensory systems, in both hardware and software, capable of providing 3D surface reconstruction of small (0.5 – 100 mm) objects with complex shapes. A detailed design methodology will be presented that uniquely provides a guide to determine the optimal design of the hardware and software of accurate SL systems. The proposed approach focuses on minimizing measurement errors in order to obtain accurate 3D reconstruction results. This is achieved by optimizing: 1) the SL system configuration of the hardware components, and 2) the sequence of fringe patterns for the optimal SL system configuration.

1.3 Proposed Methodology and Tasks

This thesis presents the overarching design methodology needed for the development, implementation and evaluation of SL sensory systems that use phase-shifted patterns to provide accurate 3D surface profiles of small complex objects. In particular, the following contributions are made in each thesis chapter.

1.3.1 Literature Review

Chapter 2 presents an extensive review of the literature on the state of the art regarding the important research areas for designing and developing accurate SL systems: 1) the configuration design of SL systems, 2) the pattern sequence design for SL systems, and 3) the SL techniques proposed for measuring micro-scale objects. The latter will particularly provide a comprehensive overview of literature on the proposed SL systems for micro-scale measurements. This will help to summarize the different approaches implemented for measuring micro-scale objects and will also highlight the challenges that are still remaining to overcome.

1.3.2 Design Methodology for SL System Configurations

The contributions of Chapter 3 is the development of a novel design methodology for determining the optimal triangulation configurations for SL systems measuring complex objects, including both

the optical specifications and the geometric organization of the hardware components. The design methodology determines the optimal configuration of the hardware components based on the following multiple performance metrics: 1) minimizing the 3D reconstruction errors, 2) maximizing the pixel-to-pixel correspondence between the projector and camera, and 3) maximizing the dispersion of the measured 3D points within a required measurement volume. In addition, design constraints are defined in order to assess the feasibility of physically implementing an optimal SL configuration in terms of the hardware specifications.

1.3.3 Pattern Sequence Design Methodology for SL Systems

The contribution of Chapter 4 is the development of a novel design methodology for determining the optimal pattern sequence for SL systems using sinusoidal phase-shifting techniques. The number of fringes used in the projected light patterns has a direct effect on the 3D reconstruction errors. The proposed methodology uniquely considers both the number of patterns that are needed in the pattern sequence as well as the number of fringes for each pattern in order to reduce the reconstruction errors caused by random noise in the captured patterns.

1.3.4 Design Methodologies for Micro-Scale Measurements

The contribution of Chapter 5 is the development of an SL technique for measuring micro-scale objects. Typically, microscope lenses have a shallow depth of field, thus making it difficult to measure small objects with complex surface profiles using large magnifications. The design methodologies for SL system measuring micro-scale are developed considering the image focus fusion of the images of the patterns, which effectively increasing the depth-of-field of the SL system. In addition, a novel calibration approach is proposed which provides calibration models that have the best predictive capabilities for a given calibration data set within the entire measurement volume.

1.3.5 Implementation Experiments on SL System Configuration Design for Macro-Scale Measurements

The contribution of Chapter 6 is the experimental verification of the design methodology presented in Chapter 3, which was used to determine a set of optimal system configurations for a given set of hardware components of an SL system. Experimental measurement performance of an optimal system configuration is compared with a non-optimal hardware configuration.

1.3.6 Implementation Experiments on Pattern Sequence Design for SL Systems for Macro-Scale Measurements

The contribution of Chapter 7 is the implementation of the pattern sequence obtained by the design methodology presented in Chapter 4, which minimizes the noise in the reconstruction measurements. The pattern sequence is implemented on an SL system and its performance is compared to a commonly used approach. A variety of test objects are measured with the patterns of both approaches.

1.3.7 Implementation Experiments on Design Methodologies for Micro-Scale Measurements

The contribution of Chapter 8 is the development and implementation of an SL system using the novel SL with image focus fusion technique presented in Chapter 5. The SL system is calibrated to measure micro-scale objects within a measurement volume of 0.5x0.5x0.5 mm^3. Different small complex objects are measured to demonstrate the performance of the SL system when measuring micro-scale objects.

1.3.8 Conclusions

Finally, Chapter 9 presents concluding remarks on the developed SL sensory systems and experimental results, summarizing the contributions to the state of the art and describes future possible research directions.

Chapter 2
Literature Review

In order to provide accurate 3D surface reconstruction of small complex objects, a novel SL sensory system needs to be carefully designed in terms of its system configuration and pattern sequence. In Section 2.1, a brief description of SL sensory systems is provided, prior to a discussion in Section 2.2 on existing design guidelines for SL systems that have been presented in the literature for system configuration (Section 2.2.1) and pattern sequence (Section 2.2.2). Finally, Section 2.3 describes previous works on the design and implementation of SL systems for micro-scale measurements.

2.1 SL Sensory Systems

An SL sensory system utilizes an active triangulation-based method consisting of a controllable light source such as a projector to illuminate an object of interest with a predefined light pattern, and at least one camera to capture the deformation of the pattern as a result of the surface profile of the object [27]. Namely, the 3D reconstruction of the surface profile of an object is obtained by the triangulation relationship between the projector, the camera and the measured object. A pattern coding strategy is used to project a texture pattern onto the surface of the object to unequivocally determine the projector-camera correspondence for each 3D point on the object's surface [17]. Once this correspondence is established, the 3D surface profile is obtained by determining the 3D point for each projector-camera pair using the triangulation relationship of the SL hardware configuration.

In general, SL techniques can be classified as discrete or continuous according to the nature of the coded patterns they use. Discrete SL techniques use patterns with profiles of distinct intensity or color levels, e.g. black/white Gray-code fringe patterns [19, 28], De Bruijn based colored patterns [29], and pseudorandom 2D M-arrays [30]. On the other hand, continuous SL techniques utilize patterns that present smooth variations in intensity or color throughout the pattern profile, e.g., grayscale patterns with sinusoidal [13, 31] or trapezoidal [32] profiles, or rainbow-colored patterns [33]. Furthermore, discrete and continuous SL techniques can be categorized depending on the way the pattern is encoded, i.e. multiplexing in time, frequency or spatial domains. Time multiplexing techniques encode information for a point in the pattern by a temporal sequence of

intensity/color projections [3, 32], while frequency multiplexing patterns use one or two periodic continuous patterns that are analyzed in the frequency domain [34-35], and spatial multiplexing techniques use only one pattern and decode each point in the pattern based on the intensity level or color of the surrounding points [29-30]. In general, continuous SL techniques are more robust to variations in ambient light and reflectivity, particularly time multiplexing implementations such as phase shifting, which can suppress the effect of the measured object's albedo [17].

Based on the pattern coding strategy used, the projector-camera correspondence can be established by comparing the projected patterns with the captured deformed patterns. In order to obtain the 3D surface profile of a measured object, a geometric triangulation model between the projector, camera and measured object is required to transform the 2D information obtained from the captured deformed patterns into 3D points representing the object's surface profile. Geometric triangulation models for determining this 3D reconstruction can either be based on optical geometry, which rely on modelling the properties of the lenses of the camera and projector [24, 36], or on calibration matrices, which are empirically determined by measuring a set of known objects of interest [37]. Triangulation models based on optical geometry use orthogonal [38] or perspective [24, 39] projection, and require precise knowledge of optical parameters of the camera and projector, such as focal lengths, apertures, pixel sizes and resolutions. On the other hand, models based on calibration matrices rely on measuring a set of objects with known surface profiles, which are located at pre-defined positions within an SL system's measurement volume [37]. Based on measurement data obtained from calibration, a polynomial regression model is defined for each camera pixel to determine the 3D coordinates of the measured point as a function of its corresponding projector pixel [40]. Although triangulation models based on calibration matrices can deal with optical non-linearities, they require the estimation of a large number of parameters obtained from accurate calibration experiments. Triangulation models based on optical geometry, on the other hand, only require the estimation of a small set of optical and geometrical parameters for the camera and projector. The latter models have the added advantage of explicitly determining the effects of the model parameters on the accuracy of the 3D reconstructed points, while in the calibration-based models these effects are coupled and expressed implicitly in the calibration matrices [40].

2.2 Design of SL Sensory Systems

Over the past few decades, the development of SL systems has focused on two important goals [41]: 1) reducing measurement time, and 2) decreasing reconstruction errors. These goals are achieved by investigating both the geometric triangulation model and the pattern coding strategy used for 3D reconstruction.

2.2.1 Configuration Design of SL Systems

In [38], the influence of triangulation configuration on the reconstruction errors of an SL system was estimated when considering the curvature of an object. An optical geometric-based model was used to assess the performance of different triangulation configurations, in which the projector was considered as a reverse camera with the same focal length and pixel size as the camera. Both the projector and the camera were assumed to be coplanar as well as having mirrored orientations with respect to the measured object, i.e., forming an isosceles triangulation with the object. The reconstruction errors were modelled to include the effects caused by the: 1) discrete nature of the camera sensor, 2) object feature location errors due to unfocused captured images, and 3) system modelling error introduced by the orthographic projection model for the camera and the projector, which corresponds to an infinite focal length. A single-variable parametric simulation study was conducted to examine the effect that a triangulation configuration, characterized only by the angle between the optical axes of the camera and projector, had on the reconstruction errors for surface curvature. Results of the study showed that triangulation configurations have a significant effect on reconstruction errors. The results also suggested that an optimal angle could be found between the optical axes of the camera and projector to either reduce the error due to surface orientation or surface curvature, but not both simultaneously.

In [24], the reconstruction errors of an SL system were modelled and simulated using an optical geometric triangulation model. The model was represented as a function of the optical hardware specifications of the SL system and potential triangulation configurations between the camera, the projector and the measured object. The chosen configuration for the SL system was determined through a parametric sensitivity analysis based on a simplified planar triangulation model considering the projector and the camera with identical optics placed on an arbitrary isosceles triangle. Namely, a parametric study was conducted by varying each SL system parameter (e.g., orientation of the camera and projector) and observing its influence on the reconstruction errors,

while other system parameters (e.g., distance to target object, focal lengths) were held constant at arbitrary values. Results of the sensitivity analysis showed that the reconstruction errors were influenced by the relative distance between the camera and the projector and their orientation with respect to the measured object. The final selected triangulation configuration was the one that provided the smallest reconstruction errors based on the sensitivity analysis.

To date, the design guidelines presented in the literature for determining the triangulation configuration of SL systems have been based on simplified geometric triangulation models [24, 38]. These models use coplanar isosceles triangulation configurations for the hardware set-up and identical optics for the projector and camera, and therefore assume matching pixel size and resolution for these components. Furthermore, they do not consider the non-linear interactions between the system parameters due to the triangulation configuration. However, the majority of implemented SL sensory systems consist of projector and camera hardware components that do not have the same pixel size and/or resolution, and therefore require different optics [19, 24, 42-44]. A 3D geometric triangulation model needs to be developed that explicitly considers the different optical specifications (e.g., focal lengths), pixel sizes and/or resolution for the projection and capturing hardware. These existing differences result in 3D triangulation configurations for which this hardware may no longer be coplanar. Therefore, there is a need for a design methodology that uses a general 3D triangulation model that does not assume identical optics for the camera and projector.

2.2.2 Pattern Sequence Design for SL Systems

Over the years, many SL techniques have been developed, differing mostly on the type of light pattern projected onto the object, e.g. discrete or continuous, and the coding strategy, e.g., multiplexing in spatial, time or frequency domain. The reader is referred to [17] for a recent review of SL techniques. In [17], the influence of pattern coding strategies on the aforementioned goals was investigated by comparing the implementation of three discrete and three continuous SL techniques, using the same SL hardware set-up and triangulation configuration, on measuring a known complex object and a flat plane. The techniques used were time, frequency or spatial – based multiplexing, and were compared with respect to their measurement time and their reconstruction errors. The measurement time was observed to be correlated to the density of the 3D reconstruction. In this regard, the spatial-based multiplexing discrete technique provided less

dense 3D reconstructions in the shortest measurement time, while the time-multiplexing continuous technique resulted in the densest 3D reconstructions with the longest measurement time. In terms of the reconstruction errors, the time multiplexing methods, either discrete or continuous, presented the most accurate 3D reconstructions but required the projection of many patterns, making them mainly suitable for static objects. Continuous patterns based on frequency multiplexing provided dense 3D reconstruction requiring at most two pattern projections making them appropriate for moving objects, however, they had the highest sensitivity to the surface characteristics (e.g. color, reflectivity) of the measured object and to the optical non-linearities (e.g. lens distortion) of the camera. It was also found that discrete and continuous spatial-multiplexing techniques presented high sensitivity to an object's color as well as background illumination, as the decoding of each pixel was also affected by localized intensity levels from neighboring pixels. Overall, the comparison that was presented showed that the accuracy and the measurement time of an SL system are a result of numerous factors including the number and type of the texture patterns used by the coding strategy, the surface characteristics of the measured object and the number of 3D reconstruction points that are obtained. More recent work presented in [45] has demonstrated that the direction of the projected patterns is an important factor that could affect measurement accuracy. In [45], the fringe angle of a multi-frequency phase-shifting approach was determined by comparing the phase differences of the top and bottom surfaces of an object. Results are shown for a step height block and a sculpture.

This thesis focuses on continuous time-multiplexing techniques, namely on sinusoidal phase-shifting which has been widely used due to its robustness to both variations in object surface reflectivity and ambient lighting when compared to discrete fixed patterns [27]. This technique consists of projecting a sequence of continuous fringe patterns with phase-shifted sinusoidal intensity profiles in order to establish the projector-camera pixel correspondence. When multiple fringes are projected, the periodic nature of the phase obtained from the multi-fringe patterns does not provide a unique projector-camera pixel correspondence for 3D reconstruction. Therefore, in SL systems that use active phase unwrapping, a one-fringe pattern set is used to unwrap the phase obtained from a multi-fringe pattern set and to determine matching projector-camera pixel correspondences. The pixel phase values provided by the one-fringe patterns are used to determine the fringe order [46], i.e., the specific fringe number for a given pixel in the multi-fringe pattern. This information is used to establish unique projector-camera correspondences for multi-fringe

patterns in a process defined as phase unwrapping, which is discussed in detail in Section 4.1.2. The number of fringes used within the multi-fringe pattern has a significant effect on reducing the 3D reconstruction errors. Namely, these 3D reconstruction errors result from inaccurate projector-camera pixel correspondences caused by random noise in the phase values as well as fringe order errors during phase unwrapping [46-51]. Therefore, multiple active phase unwrapping steps can be used to further reduce these errors [47, 50].

Several methods have been proposed to compensate for phase unwrapping errors, either by determining the phase value of a pixel of interest by using phase values from neighboring pixels [46, 52-53] or by directly reducing the random noise in phase [49-51, 54]. With respect to the latter, the random noise in the unwrapped phase can be reduced by either: 1) increasing the number of phase-shifted patterns used [50-51, 54], 2) averaging repeated phase measurements [54], and/or 3) increasing the number of phase unwrapping steps [49-50]. The first two approaches for reducing the random noise in phase require the acquisition and processing of a larger number of phase-shifted pattern images of the target object, leading to longer computation times which are not compatible with measuring dynamic objects. In addition, these approaches are not robust to the fringe order errors that are caused by measuring discontinuous object surface profiles with multi-fringe patterns [45-46]. In such cases, the signal-to-noise ratio can be low [46]. Alternatively, the third approach of increasing the number of phase unwrapping steps has shown to have the potential to reduce the random noise in phase, although the magnitude of this noise reduction is sensitive to the number of fringes of each multi-fringe pattern used at each phase unwrapping step [50, 53].

This thesis also focuses on increasing the number of phase unwrapping steps as a means to reduce the random noise in phase. As discussed above, when multiple phase unwrapping steps are used, the accuracy of the absolute phase values is related to the number of fringes used in each pattern and the number of unwrapping steps used during sequential active phase unwrapping. To date, approaches that have been reported in the literature for defining sinusoidal patterns for SL sensors using active phase unwrapping have either focused on reducing measurement noise by: 1) increasing the number of fringes [47, 49], or 2) determining the steps for sequential phase unwrapping [50-51].

In [47], a phase shifting technique using multi-fringe patterns was presented in order to simultaneously measure 3D surface profiles of various slow-moving objects with arbitrary height

changes. The proposed algorithm used sequential unwrapping with a set of multi-fringe patterns in which the number of fringes was increased by a factor of 2 at each unwrapping step, starting from a single fringe pattern. This phase unwrapping approach was verified by simultaneously measuring two sculptures and a human face in the same scene. Results demonstrated this technique is less sensitive to motion and provides lower noise levels than when only using a single fringe pattern. However, no criterion was presented regarding how to determine the number of phase unwrapping steps, or the rationale for increasing the number of fringes by a factor of 2 in each unwrapping step.

In [49], the sequential unwrapping approach of [47] was further extended by applying a Gaussian filter to the relative phase values to remove noise before phase unwrapping. Six unwrapping steps were used, each increasing the number of fringes by a factor of 2. The filtered phase values were used for determining the fringe order for each pixel, which were then used to unwrap the raw (unfiltered) phase values from the patterns. Regions with erroneous phase values were identified and filled based on the phase values of adjacent pixels. Experiments measuring a human face demonstrated the ability of the proposed framework to reduce the random noise in the phase.

In [50], the set of multi-fringe patterns was experimentally selected for reducing 3D reconstruction errors. Several arbitrary sequences of increasing numbers of fringes were empirically tested to reduce the standard deviation of the 3D measurements of various objects. Results found that there was an optimal sequence of multi-fringe patterns to minimize the error suggesting that a mathematical model would be needed to determine this optimal sequence. In [51], the same authors presented a procedure to determine the number of fringes for a single-step phase unwrapping using a mathematical model. Namely, stochastic analysis and analytical models were used to determine the descriptive statistics of the noise in phase values caused by the image intensity noise that was experimentally observed during measurements of an object of interest. The model considered the standard deviation of the relative phase as a function of the number of fringes and the random noise value in the relative phase for an object of interest. In addition, a numerical approach based on a Monte Carlo statistical simulation was presented to create a plot of the standard deviation of the unwrapped phase values as a function of the number of fringes in the multi-fringe pattern. Based on the analytical and numerical models, guidelines were proposed to estimate the optimal number of fringes which corresponds to the minimum standard deviation of the unwrapped phase

values. If the optimal number of fringes obtained from the numerical and analytical models were not equal, the designer was left to choose which number of fringes to use.

In summary, previous work has provided guidelines about how to select the number of fringes which minimizes 3D reconstruction errors when using a single step of active phase unwrapping, and has shown how multiple unwrapping steps based on patterns with an increasing number of fringes can reduce unwrapping errors caused by random noise in relative phase. However, there is an optimal number of fringes after which no further reduction in noise is achieved in multiple unwrapping steps. Hence, optimizing the selection of both the number of phase unwrapping steps and the number of fringes in each multi-fringe pattern will reduce measurement errors without unnecessarily increasing the number of pattern images that need to be captured of the target object. Therefore, there is a need to develop a formal methodology that considers selecting the number of fringes for each pattern of a multi-fringe pattern set when using sequential multi-step active phase unwrapping (i.e., using *multiple* phase unwrapping steps) to minimize the measurement errors caused by random noise in phase values.

2.3 SL Systems for Micro-scale Measurements

In this section, structured-light systems that have been developed for micro-scale measurements are presented, focusing on the general software and hardware components of such systems. Then the calibration approaches used in the literature for these systems are discussed.

2.3.1 Development of Micro-scale Systems

A comprehensive overview of the literature on the proposed SL systems for micro-scale measurements is presented in order to summarize the existing approaches. Each approach is discussed and the specifications of the system developed are presented. Finally, the limitations of existing approaches are highlighted.

In [55], a system for 3D microscopy was presented. The system used a stereo-microscope in which one of the light paths was modified to use a collimated LED light source and a sinusoidal grating to project fringe patterns, while the other light path was used for a CCD camera for imaging. A stereoscopic angle of 12° was used as the triangulation angle necessary for obtaining 3D measurements. Four phase-shifted sinusoidal patterns with a wavelength of 1/6 mm were projected onto a field-of-view (FOV) of 5.8 x 5.8 mm, with 30 fringes. The phases were unwrapped with a

reliability-based approach, i.e., a path-dependent approach that unwraps the phase value of pixels in order of their reliability, which is estimated based on the differences in phase values with respect to neighboring pixels, local changes in intensity modulation, among other metrics. A second order polynomial regression model was used for mapping the unwrapped phase values to the depth of the scene with respect to a reference plane. As an illustration of the system's capabilities, a coin (a United States one-cent coin) was measured.

In [56], a microscope-based structured-light system was developed for 3D reconstruction of specular reflecting surfaces with very low surface roughness and low local slopes (smoothly varying surface profiles). The projected patterns consisted of an array of light dots generated by a matrix-shaped array of pinholes with a pinhole radius of 20 μm and a pinhole pitch of 120 μm, and a density of 35,000 dots/mm^2 when projected onto the object surface. The CCD imaging sensor had a resolution of 1280 x 960 pixels and a pixel size of 3.5 μm. The surface profile of an object was measured by capturing a stack of images, scanning the object as it was moved to different positions along the optical axis (corresponding to the z coordinate in the world coordinate system) using precision stages. Based on the resulting stack of images with different focuses, which are indexed to the positions of the stages when the image was taken, the surface profile of the object was determined. To this end, at a given pixel, a Gaussian distribution function was fitted to the set of image intensity values obtained for different object positions. Then, the location of the object surface was determined as the location of the peak value of the fitted Gaussian distribution function, the rationale being that the presence of the reflective surface results in the highest image intensity captured during the measurement procedure. A similar procedure was used to estimate the image coordinates (x, y) of the pixel, in order to correct for the apparent lateral movements of objects between images taken at different focus levels. The repeatability of the system was tested by measuring a flat mirror, and determined to be 0.01 μm in (x, y) , and by 0.03 μm in z, based on 10 repeated measurements. The system was then used to measure a polished glass reflective sphere. Deviations between measured 3D points and the nominal sphere dimensions were found to have a mean of 2 μm and a standard deviation of 0.3 μm.

In [57], a structured-light system for measuring micro-scale objects was presented. The system consisted of an LCD projector with a resolution of 832 x 624 pixels used to project a sequence of four phase-shifted sinusoidal intensity patterns through a long working distance (LWD) microscope lens, and a CCD camera also with a LWD microscope lens to capture pattern

deformation. Based on the images of the deformed patterns, the relative phase map is obtained and unwrapped using a reliability-based approach based solely on phase differences with respect to neighboring pixels. To recover, the surface profile of the measured object, the height at a given point on the object surface is directly proportional to the change in the unwrapped phase at that point caused by the presence of the object, with respect to a reference plane. The proposed system was used to obtain the surface profile of the inscriptions on a 1-cent Singapore coin, a micro-resistor mounted on a printed circuit board, and the copper pad on a ball grid array electronic component. The measured objects had a maximum height profile (z-coordinate) of 50 μm, and were measured with a reported accuracy of 2.5% (i.e., 2 μm) with respect to measurements provided by a coordinate measuring machine, which relies on scanning the object surface measuring each point with a contact probe. A second generation design of this system was presented by the same authors in [18]. This new SL system was designed to have a compact footprint and measure out-of-plane displacements of micro-components with sub-micron resolution, but otherwise no further innovations were presented regarding the calibration or measurement methods or associated software. The new design mounted the LCD projector and CCD camera with LWD microscope lenses on a rigid fixture perpendicular to a three-axis stage where the measured object was placed, with the goal of addressing alignment and portability issues, and reducing the system footprint with respect to earlier version of the system [57]. The experiments measuring the profiles of a micro-mirror and a micro-electrode pad qualitatively showed that the system was able to measure object features with lengths of 0.1 mm, though the accuracy and repeatability of the measurements was not reported.

In [58], the same authors as in [18] presented a structured-light system for microscale measurements that used a novel two-step phase-shifting technique, as opposed to using three or more phase shifting steps. The rationale for their proposed method was to avoid the need for phase unwrapping so as to improve the potential measurement speed of the system. The structured-light system developed by the authors consisted of a CCD camera and an LCD projector both using LWD lenses. In their experiments, the two-step phase shifting technique was compared with the four-step phase-shifting method used in their previous work [18, 57], and with measurements obtained with a coordinate measurement machine. Results showed that the two-step phase-shifting produced measurements within 0.76% from those obtained with the four-step phase-shifting approach, and that the measurement errors of the two-step approach when measuring the profile

of a coin with a maximum height of 120 μm was approximately 8 μm. Although the proposed technique could potentially provide faster measurements of the surface profile of the object, the effect of using only two phase-shifted patterns on the resulting sensitivity to image noise, ambient illumination and surface albedo, was not documented.

In [59], the development of a real-time SL system for microscopic profilometry based on phase-shifting was presented. The proposed system was based on fitting a DMD projector and a CCD camera to a stereoscopic microscope. Four phase-shifted sinusoidal patterns with a period of 8 pixels were used for measuring a field-of-view (FOV) of 10.67 x 8.01 mm on the object. The main contribution of this system was the overall measurement speed achieved to provide a 3D surface profile, which was the result of their particular hardware and software implementation, which leverages the graphics card GPU to parallelize both image acquisition and post-processing steps such as phase recovery, phase unwrapping, phase to height conversion, noise filtering and rendering. Overall, the system was able to render real-time images at a frame rate of approximately 30 Hz. To determine the measurement accuracy when measuring static and dynamic objects, a flat glass plate and a latex membrane dynamically deformed by pushing it the tip of a pen were measured with the proposed system. Isometric errors of 17 μm were reported, most of which were due to the lateral resolution of the camera pixels (17 μm/pixel at the center of the volume).

In [60], an SL system for 3D microscopy was developed combining a DMD projector, a CMOS camera and LWD microscope lenses with fixed focal lengths. The triangulation of the hardware configuration of the system was set with the fringe projection orthogonal to the reference plane and the camera at an angle that was determined using the Scheimpflug principle to maximize the in-focus measurement volume on both the camera and projector lenses. Namely, the camera CMOS sensor was tilted with respect to the optical axis of the lens, so that the reference plane, the CMOS plane and the principal plane of the camera lens intersect at a single point. This geometrical arrangement maximizes the depth-of-field (DOF) around the reference plane in which both the camera and the projector are in focus. The developed system was tested by measuring a 50-cent Chinese coin and a ceramic flat plate, both placed orthogonal to the projector and moved to four different depth positions, separated 100 μm apart, using a precision stage. The experimental results indicated that the obtainable measurement volume was 4 mm x 5 mm x 0.5 mm, with a standard deviation of 4 μm. Observed measurement errors in the range 1-9 μm were reported to be a result

of the positioning errors of the stage, i.e., to uncertainty about the actual position of the calibration object when generating the calibration data.

2.4 Calibration of SL Systems

System calibration is important to the development of high-accuracy SL systems. The accuracy of the 3D reconstruction depends on the accuracy with which model parameters can be estimated based on calibration data [60]. Calibration approaches that have been proposed in the literature for SL systems can be classified into two categories: 1) model-based approaches that rely on parameterized physical models of the system, with model parameters that are estimated based on calibration data [42, 60-62], and 2) empirical approaches that utilize statistically derived models to map the actual measured information (e.g., image coordinates) to the desired measurement variable (world coordinates of the object surface) [55, 63].

Though model-based and empirical calibration approaches have been proposed for SL systems to measure macro-scale objects [64], calibration for measuring micro-scale objects poses additional challenges. First, micro-scale measurements require special lenses whose optics typically deviate from pinhole models, thus requiring new calibration approaches [42]. Second, lenses used for micro-scale measurements have shallow depth of field, thus limiting the region of the scene inside which the target object is in focus. The shallow DOF poses a challenge for calibration approaches that rely on multiple images of a calibration object at different positions and poses inside the measurement volume. The challenge lies in that, because of the shallow DOF, only a limited set of independent measurements can be made of the calibration object, introducing collinearity and ill-conditioning problems in the model fitting algorithms that use this data to determine the calibration parameters. To deal with these challenges, several calibration approaches have been proposed in the literature for micro-scale measurements. In the remainder of this chapter, these approaches are discussed.

2.4.1 Model-based Calibration

SL-based 3D surface profiling in macro-scale applications has extensively used calibration approaches that estimate the intrinsic parameters of the camera and projector, as well as the extrinsic parameters of the SL system triangulation configuration (e.g., [42, 61]), based on pinhole optical models. However, micro-scale SL systems require special lenses, whose optics deviate

from these pinhole models [42]. Hence, alternative procedures have been presented for the calibration of micro-scale SL systems, as described below.

In [62], a new calibration method was proposed for an SL 3D microscopic system that combines a projector using a LWD microscope lens, modelled with pinhole optics, and a camera with a telecentric lens, modelled as an orthographic projection of the scene with a constant magnification. The proposed calibration procedure required first to obtain the intrinsic parameters of the projector using the standard procedure of considering it as an inverse camera [42]. Namely, a flat calibration object with a grid of circle markers was imaged under different poses. For each pose, multi-fringe patterns with 9 phase-shifts were projected, plus single-fringe patterns to resolve discontinuities at fringe boundaries. After the camera-projector pixel-to-pixel correspondence was established using the captured phase values, the images were mapped to the projector to determine its intrinsic parameters. Using a precision micro-stage to place the calibration object at a known world coordinate frame, the coordinates of the target points of the calibration object were determined and used to estimate the extrinsic parameters of the projector with a Levenberg-Marquardt iterative procedure. Finally, with the calibrated projector, the camera extrinsic transformation was estimated. Defining the world coordinate system to be aligned with the projector coordinate system, the 3D coordinates of the calibration object markers were determined, and this information was used to find least-squares estimates of the world-to-camera transformation matrix, i.e., to estimate the calibration parameters for the camera. Calibration experiments performed with the developed system resulted in ±5 μm errors, with RMS errors of 1.8 μm and 1.2 μm for the camera and the projector, respectively.

An alternative model-based calibration model was proposed in [60], consisting of a general imaging model that mapped each pixel in the camera CCD sensor or the projector DMD panel with a unique light ray. In this general imaging model, pixel-to-pixel correspondences obtained from absolute phase values served to identify homologous pixel pairs. Homologous pixel pairs were pairs of pixels that have the same phase values and thus corresponded to the same light ray, emitted from the projector and reflected by the object onto the camera. During calibration, a flat calibration object with markers was placed on a precision stage, so that the world coordinates of each marking were known. By moving the object while tracking the movement of the markers on both the world coordinate system and in pixel coordinates, the mapping of pixels to light rays was established for each pixel and stored in a look-up table. To calibrate this model, measurements of

the calibration object in at least 3 known poses, two of which cannot be parallel, were required. Based on these three sets of camera-projector correspondences, interpolation was used to measure other objects of arbitrary shape. Calibration errors were not reported, however measurement errors were. A ceramic flat plane placed in different positions inside the measurement volume resulted in mean and standard deviation of measurement errors in the range 1 – 5 μm and 2.3 – 3.7 μm, respectively.

Model-based calibration approaches are based on physical modelling of the system optics. Though they have been widely, successfully used in macro-scale measurement applications, the special optics required for micro-scale measurements is not well represented with pinhole models. More importantly, model-based calibration approaches require multiple images of the calibration object with different positions and poses within the measurement volume to define a calibration data set with a large number of linearly independent samples. This makes model-based approaches unsuitable for SL systems for micro-scale measurements, in which the large optical magnifications that are used result in shallow depth of fields. For these reasons, the literature in micro-scale measurements with SL systems prefers empirical calibration models, described below.

2.4.2 Empirical Calibration Models

In contrast with calibration approaches based on modeling the optics of the projector and the camera, empirical calibration models rely on linear regression to create a mathematical model that maps the surface profile of an object, $S(x, y)$, to the captured phase values at a given location (x, y) on the imaging sensor. These empirically based mathematical models are usually referred to as phase-to-height equations. As an advantage, empirical calibration approaches can be used regardless of the optics of the system, and are thus suitable for systems with pinhole lenses, telecentric lenses, or combinations thereof. Therefore, empirical calibration approaches are suitable for structured light systems for both macro- and micro-scale applications.

To calibrate a structured-light 3D sensing system empirically, the direction of the z-coordinate (also known as depth, or range) is defined, typically aligned with the bisector of the angle between the optical axes of the camera and projector [63] or with the optical axis of the camera [55]. In [63], a flat calibration object is placed on precision micro-stages, and it is imaged in a sequence of positions as it is moved along the z-coordinate. Then, one of the positions of the calibration object (usually the farthest from the camera) is defined as the reference plane and assigned a z-coordinate

value of zero. For each pixel in the imaging sensor, a relationship can be established between the known position of the calibration plane measured with respect to the reference plane, and the change in phase value for that pixel with respect to the phase value the pixel had when the calibration plane was placed in the reference position. For instance, in [63] the phase-to-height relationship for a given pixel is defined as linear regression of the change in phase values between the reference position and the measured position. The regression coefficients are estimated for each pixel based on the calibration data, and stored in a Look-up Table (LUT). To verify the accuracy of the empirical calibration approach, the calibration plane was measured at additional locations (not used as part of the calibration data), resulting in errors of 5 – 7 μm with respect to the known position of the calibration plane as given by laser interferometry with nano-scale accuracy.

More recently, in [55], a different phase-to-height relationship was presented which, although empirically determined, derived its functional form from the optical behavior of symmetric, co-planar structured-light systems with ideal, identical optics for the camera and the projector. In such cases, it has been established that phase and height are inversely proportional to each other due to the perspective projection caused by pinhole optics. An empirical model was proposed as a linear regression of the reciprocal of height as a function of the reciprocal of phase, with a different set of regression coefficients for each pixel, stored in a LUT. Using this empirical calibration model, a measurement was taken of a flat plane in two positions separated by 13 μm (as indicated by the translation stages), resulting in an error of 0.082 μm (0.6%). However, it is difficult to assess the accuracy of the proposed calibration method based on a single data point, and without information about the position error of the stages used for the calibration. As an additional verification of accuracy, the equation of a plane was fitted to the measured points, and the standard deviation of the points with respect to the fitted plane was 0.529 μm.

Though empirical calibration approaches using look-up tables can be used regardless of the optics of the system, their main disadvantage, besides their memory storage requirements, is that each pixel-specific regression model is fitted to a small data set containing only information about the height of the surface that is observed at that camera pixel. For instance, if during the calibration procedure the calibration object is imaged at 10 different locations in the z-coordinate, the LUT approach would require fitting one regression model for each pixel based on (at most) 10 data points. Because of the small number of data samples used to fit the regression model, the resulting

model coefficients are sensitive to noise in the calibration data, and result in a larger predictive variance, i.e., wider confidence intervals for the model predictions.

Chapter 3
Design Methodology for SL System Configurations

In this chapter, a novel generic design methodology is proposed for determining optimal triangulation configurations of SL sensory systems for 3D reconstruction of complex objects. The performance of SL systems is determined by the emitting (i.e., projector) and capturing (i.e., camera) hardware components and the triangulation configuration between them and an object of interest. The optimal configurations of the hardware components are determined with respect to a set of performance metrics: 1) minimizing the 3D reconstruction errors, 2) maximizing the pixel-to-pixel correspondence between the projector and camera, and 3) maximizing the dispersion of the measured 3D points within a measurement volume; while satisfying design constraints based on hardware and user-defined specifications. The proposed methodology utilizes a 3D geometric triangulation model based on ray-tracing geometry and pinhole models for the projector and camera. In Section 3.1 a description of the models for estimating the 3D reconstruction errors of SL systems is provided. Section 3.2 presents the proposed novel methodology for designing an SL system with each step discussed in detail.

3.1 SL system models

SL system models are utilized as key elements in the proposed design methodology in order to estimate 3D reconstruction errors. The models include: 1) pinhole models used for the camera and the projector, 2) an optical geometric model for the triangulation relationships of an SL system configuration, 3) a backward ray-tracing model for establishing the pixel-to-pixel correspondence from the projection panel to the imaging sensor, and 4) a 3D reconstruction model. These SL system models will be used within the design methodology to optimize the triangulation configuration of the hardware components in order to achieve user-defined performance metrics.

3.1.1 Camera and projector models

The camera is modelled using the pinhole model, which defines the geometric mapping between 3D object points and their 2D corresponding projections onto the image plane of the camera [65]. The camera lens is modelled as a single point, referred to as nodal point, through which the light rays enter the camera. The lens behavior is considered to be ideal, i.e., neglecting lens distortion effects [66]. Optical models that include distortion effects can also be used if they are available

prior to implementation of the design methodology. However, since prior experimental tests are needed to determine the appropriate distortion model [67-69] and the SL hardware configuration design precedes the system calibration stage, the methodology incorporates ideal lens behavior. The light rays are assumed to travel in straight lines from the measured object's surface, passing through the nodal point to the image plane of the camera, where an inverted image of the measured object is formed, Figure 1. The image plane where the inverted image is formed is placed one focal length behind the nodal point. A common approach used with the pinhole model is to place a virtual image plane in front of the nodal point [65]. The non-inverted images formed at the virtual image plane are equivalent to the inverted images from the image plane.

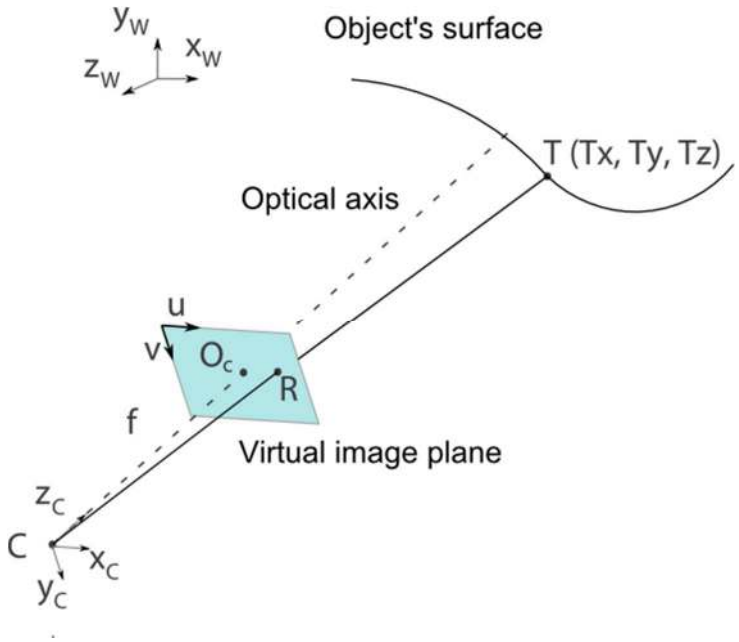

Figure 1. Pinhole model.

Figure 1 illustrates the pinhole model with its virtual image plane for a camera. The camera coordinate system is placed at the nodal point of the camera, C, where its z-axis, z_C, is aligned with the optical axis of the camera lens and intersects the virtual image plane at point, O_C, referred to as the principal point. The x_C and y_C coordinate axes are parallel to the horizontal and vertical directions of the imaging sensor of the camera, respectively. The image coordinate system is defined by convention to be at the top left of the virtual image plane, and has the axes u and v parallel to x_C and y_C.

Using the pinhole model, a 3D point, T, on the object's surface has corresponding image coordinates u and v. The mapping from 3D world coordinates to 2D image coordinates can be

obtained from the pinhole model geometry and rigid body transformations. Therefore, the coordinates of any 3D point T_i, $i = 1, \cdots, n$, of homogeneous coordinates $(X_i, Y_i, Z_i, 1)^T$ are related to its projection on the image plane, point R_i, of homogenous image coordinates $\left(u_i, v_{i,}, 1\right)^T$, by the following relationship [66]:

$$s\begin{pmatrix} u \\ v \\ 1 \end{pmatrix} = K\begin{bmatrix} R_{WC} & t_{WC} \\ 0_{1\times 3} & 1 \end{bmatrix}\begin{pmatrix} X \\ Y \\ Z \\ 1 \end{pmatrix}, \tag{1}$$

which is defined up to the scale factor s. This scale factor provides the unique representation for the mapping of the world to the image homogeneous coordinates. Namely, this scale factor is used since objects of different sizes may result in the same image if they are located at different distances from the image plane [65]. K represents the *intrinsic parameters* of the camera, and R_{WC} is the rotation matrix and t_{WC} is the translation vector from the world coordinate system to the camera coordinate system, respectively. R_{WC} and t_{WC} are referred to as the *extrinsic parameters* of the camera since they characterize the camera's orientation and position with respect to the world coordinate system.

The intrinsic parameters include the optical characteristics and the internal geometry information of the camera [70]. Namely, the focal length of the camera (f_C), the horizontal and vertical pixel sizes (k_u, k_v), and the image coordinates (u_0, v_0) of the principal point O_C. These parameters determine the transformation from the camera coordinates to the image coordinates defined by the matrix K:

$$K = \begin{pmatrix} k_u f_C & 0 & u_0 & 0 \\ 0 & k_v f_C & v_0 & 0 \\ 0 & 0 & 1 & 0 \end{pmatrix}. \tag{2}$$

With respect to the modeling of the projector, the projector itself is considered as an inverse camera where the light rays travel from the image plane of the projection panel to the target object. Therefore, the projector has its own intrinsic and extrinsic parameters based on the camera pinhole model.

3.1.2 SL configuration model

The geometric triangulation model of an SL system requires defining the relative position and orientation of the system hardware components, i.e., projector and camera, with respect to the object of interest. Figure 2(a) shows the triangulation of an SL system, using pinhole models for the camera (C) and the projector (P). The focal lengths of the optics are f_C and f_P for the camera and projector, respectively.

In order to describe an SL configuration, a *design* coordinate frame (x_D,y_D,z_D) is defined with its origin coinciding with the projector's nodal point P. This design coordinate frame provides a fixed reference coordinate system to describe the positions of the hardware components and the reference plane. In the design coordinate system, the orientation of the projector is determined by the intrinsic rotation matrix:

$$R_{\mathrm{DP}} = Y(\alpha_P)X(\beta_P)Z(0), \tag{3}$$

where α_p and β_p are Euler angles measured with respect to the design reference frame. The YXZ notation corresponds to the three elemental rotations of the projector that occur in sequence, i.e., the projector is rotated about its y-axis by α_P, then about its new x-axis by β_P, and finally about its new z-axis by 0 degrees. These two parameters represent two degrees of freedom for the projector's orientation in the triangulation model. Note that the third Euler angle is set at zero, to ensure the horizontal directions remain parallel for the projector and camera.

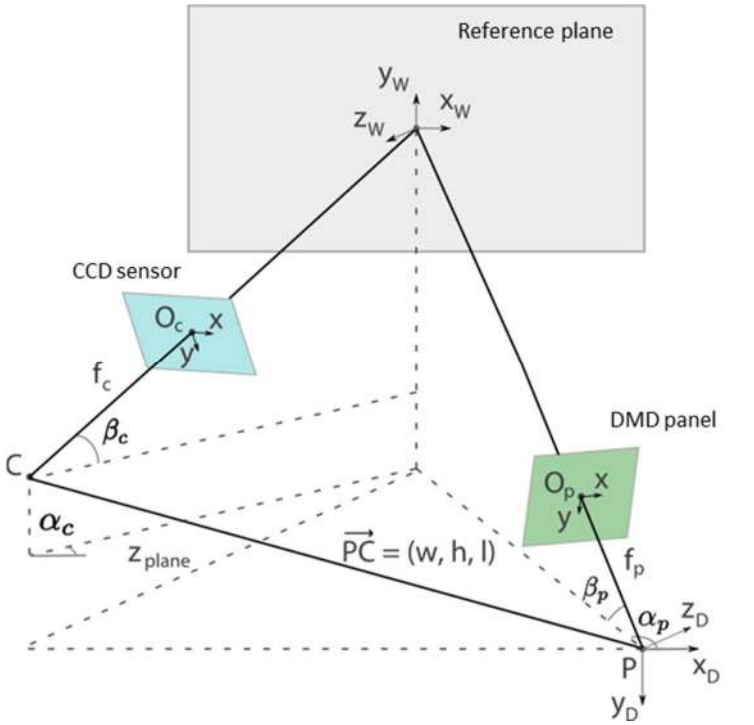

(a)

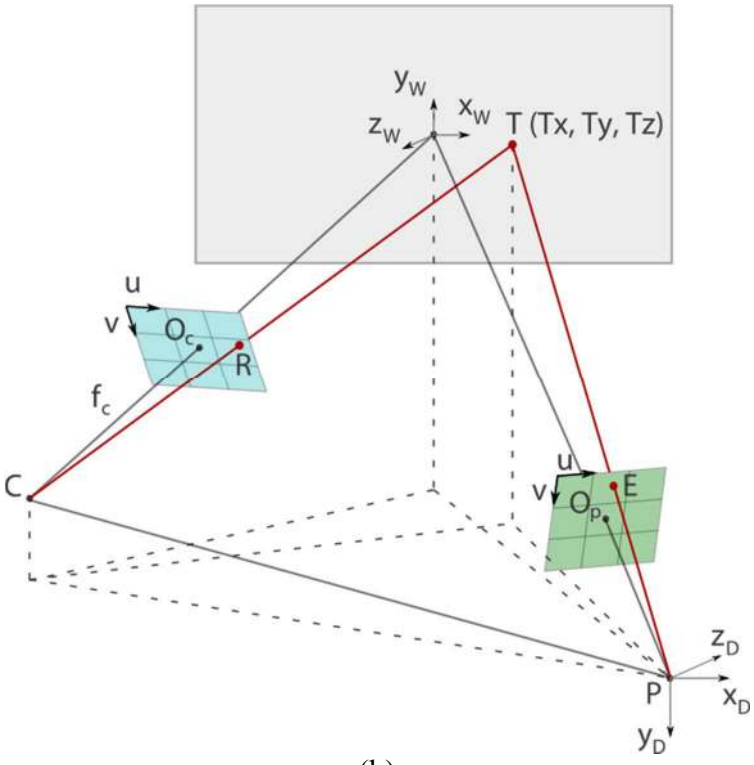

(b)

Figure 2. (a) SL triangulation configuration, and (b) ray-tracing.

The camera position with respect to the projector is set by the separation of the nodal points of the camera and the projector, i.e., w (width), h (height), l (length) in the x, y and z directions of the

design coordinate system, respectively. The 3D vector, $\overrightarrow{PC}$, corresponds to an additional three degrees of freedom for the model. In order to obtain the last degree of freedom for the model, the triangulation configuration needs to be defined in a manner that allows the optical axes of the projector and camera to intersect at a common point located on a reference plane placed at a given distance (z_{ref}). The distance z_{ref} represents this last degree of freedom. This configuration allows the measurement volume, i.e., the intersection of the fields of view and depths of field of the camera and the projector, to be centered on the imaging sensor and the projection panel. Moreover, the intersection of the optical axes determines the location of the origin of the reference world coordinate system, O_W, and defines the camera orientation (α_C, β_C).

In summary, the configuration model has six degrees of freedom: 1) the two orientation degrees of freedom of the projector (α_P, β_P), 2) the 3 degrees of freedom that define the relative position of the camera with respect to the projector (w, h, l), and 3) the one degree of freedom z-position of the reference plane (z_{ref}). In general, any arbitrary hardware configuration can be generated based on the triangulation formed by the intersection of the optical axes of the camera and the projector with a given reference plane. In the design methodology, these degrees of freedom will be used as design variables to optimize an SL system triangulation configuration.

3.1.3 Pixel-to-pixel correspondence

In order to determine the pixel-to-pixel correspondence between the projector and camera, the design methodology utilizes a unique backward ray-tracing model to define which discrete projector pixel emits the light rays captured by a camera pixel of interest; this is in contrast to the traditional approach of only considering a continuous plane for the camera sensor and the projector panel as is done in [42, 71-72]. In our backward ray-tracing model, the emitted light rays from the projector are traced backwards starting from the camera, point C, to a 3D point T on the surface of the object and then to the projector, point P, Figure 2(b). These rays intersect the imaging sensor at point R and the projection panel at point E, respectively. The mapping between the projector's and camera's image coordinates is defined to be:

$$[u_P, v_P]' = q\big(T, z_{ref}, w, h, l, \alpha_P, \beta_P, u_C, v_C, f_C, f_P, \lambda_C, \lambda_P, N_{u,C}, N_{v,C}, N_{u,P}, N_{v,P}\big), \qquad (4)$$

where the projector's image coordinates (u_P, v_P) of point T on the measured object are related to: 1) the set of the aforementioned design variables defining the hardware system configuration

$(z_{ref}, w, h, l, \alpha_P, \beta_P)$; 2) the image coordinates of the corresponding camera pixel (u_C, v_C); and 3) the optical specifications of the camera and projector hardware such as the focal length (f_C, f_P), the sizes of square pixels (λ_C, λ_P), and the vertical $(N_{v,C}, N_{v,P})$ and horizontal $(N_{u,C}, N_{u,P})$ resolutions of the camera's sensor and the projector's panel. q is the mapping function from the imaging sensor to the projection panel using the backward ray-tracing model. Collectively, the variables and parameters on the right hand side of Eq. (4) unequivocally define the geometry of the ray-tracing procedure used to establish the pixel-to-pixel correspondence.

The ray-tracing model is implemented as an iterative algorithm consisting of a step-by-step procedure that includes casting an individual camera ray through point R, determining its intersection with the object's surface (point T), tracing it back to the projection panel (point E), and determining its corresponding projector pixel. Point R on the imaging plane, expressed as $\vec{R}_{x_C y_C z_C}$ in the camera coordinate frame $(x_C y_C z_C)$, is transformed to the design reference frame by the following relationship:

$$\vec{R} = \left(R_{\mathrm{DC}}{}^{\mathrm{T}}\right)^{-1} \vec{R}_{x_C y_C z_C}, \tag{5}$$

where $R_{\mathrm{DC}} = Y(\alpha_c)X(\beta_c)Z(0)$ is the intrinsic rotation matrix of the camera, and α_C and β_C are Euler angles measured with respect to the design reference frame. The 3D point on the object surface, point T with respect to the origin of the design reference frame, is determined to be the intersection of the light ray with the object's surface:

$$\vec{T} = s\left(\vec{n}_S, \vec{C}, \vec{R}\right), \tag{6}$$

where s determines the intersection of an object's surface with normal vector $\vec{n}_S$ and a ray from $\vec{C}$ and passing through $\vec{R}$, and $\vec{C} = (w, h, l)$ corresponds to the position of the camera's nodal point with respect to the origin of the design reference frame. The corresponding point E on the projection panel, with respect to the origin of the design coordinate system, is determined by the intersection of a ray starting from $\vec{T}$ to the nodal point of the projector $\vec{P}$ as:

$$\vec{E} = \left(R_{DP}{}^{T}\right)^{-1} \left\{ \left[\frac{\left(\vec{O}_{P_{x_P y_P z_{\mathrm{P}}}} - \vec{P}_{x_P y_P z_{\mathrm{P}}}\right) \cdot \vec{n}_{P_{x_P y_P z_{\mathrm{P}}}}}{\vec{T}_{x_P y_P z_{\mathrm{P}}} \cdot \vec{n}_{P_{x_P y_P z_{\mathrm{P}}}}} \right] \vec{T}_{x_P y_P z_{\mathrm{P}}} + \vec{P}_{x_P y_P z_{\mathrm{P}}} \right\}, \tag{7}$$

where the subscript $x_P y_P z_P$ denotes the projector coordinate frame; $\vec{O}_{P_{x_P y_P z_P}} = (0,0,f_P)$ corresponds to the principal point of the projector's pinhole model; $\vec{P}_{x_P y_P z_P} = (0,0,0)$ is the position of the projector's nodal point; $\vec{n}_{P_{x_P y_P z_P}} = (0,0,f_P)$ is the normal vector of the projection plane; and $\vec{T}_{x_P y_P z_P} = {R_{DP}}^T \vec{T}$ corresponds to point T in the projector coordinate frame.

Since the projector panel and the imaging sensor are discretized into pixels, each projector pixel illuminates a certain sub-area on the object's surface, which is in turn captured by certain camera pixels. Therefore, the pixel-to-pixel correspondence between the projector and camera requires the estimation of this sub-area on the object's surface in order to determine which camera pixels capture it. In our work, the pixel-to-pixel correspondence is determined by: 1) sampling each camera pixel and by tracing backwards the light rays to determine the projector pixel from which each light ray was emitted, and 2) establishing the unique pixel-to-pixel correspondence for the camera pixel capturing the majority of the light rays from the same projector pixel. First, each camera pixel is divided into a 3x3 uniform grid and each grid cell within the pixel has a corresponding light ray defined as:

$$\left(u_{C,k}, v_{C,k}\right) = (j - 1 + 0.25 \cdot m,\ i - 1 + 0.25 \cdot n)\ \lambda_C, \tag{8}$$

where $1 \leq k \leq 9$ corresponds to the index of the light ray; $1 \leq j \leq N_{u,C}$ and $1 \leq i \leq N_{v,C}$ are the column and row of the camera pixel, respectively; and $m = floor\left(\frac{k}{N_{u,C}}\right)$ and $n = floor\left(\frac{k}{N_{v,C}}\right)$. Then, each ray is traced back to the projector's panel to determine the intersection point *E* and its corresponding projector's image coordinates u_P and v_P in order to determine the projector pixel each ray corresponds to. A camera pixel with at least 5 of its 9 sampled rays corresponding to the same projector pixel is said to have a unique pixel-to-pixel correspondence with that projector pixel.

3.1.4 3D reconstruction model

Once the pixel-to-pixel correspondence is established, the relationship between a 3D point on the object's surface and its projector-camera pixel correspondence can be expressed for the projector and camera using the pinhole model represented in Eq. (1):

$$s_P \begin{pmatrix} u_{P,i} \\ v_{P,i} \\ 1 \end{pmatrix} = M_P \begin{pmatrix} X_{W,i} \\ Y_{W,i} \\ Z_{W,i} \\ 1 \end{pmatrix}, \text{ and} \tag{9}$$

$$s_C \begin{pmatrix} u_{C,i} \\ v_{C,i} \\ 1 \end{pmatrix} = M_C \begin{pmatrix} X_{W,i} \\ Y_{W,i} \\ Z_{W,i} \\ 1 \end{pmatrix}, \tag{10}$$

where s_P and s_C are scale factors for the projector and camera, respectively; i represents the pixel under consideration; and $M_P = K_P \begin{bmatrix} R_{WP} & t_{WP} \\ 0_{1\times3} & 1 \end{bmatrix}$ and $M_C = K_C \begin{bmatrix} R_{WC} & t_{WC} \\ 0_{1\times3} & 1 \end{bmatrix}$ are the transformation matrices for the projector and camera, which are defined based on the geometry of the SL system configuration under consideration.

Utilizing Eq. (9) and (10), we can obtain the set of linear equations needed to estimate the world coordinates of a 3D point on the surface of an object given its projector-camera correspondence:

$$\begin{bmatrix} (u_{P,i}m_{31,P} - m_{11,P}) & (u_{P,i}m_{32,P} - m_{12,P}) & (u_{P,i}m_{33,P} - m_{13,P}) \\ (v_{P,i}m_{31,P} - m_{11,P}) & (v_{P,i}m_{32,P} - m_{12,P}) & (v_{P,i}m_{33,P} - m_{13,P}) \end{bmatrix} \begin{pmatrix} X_{W,i} \\ Y_{W,i} \\ Z_{W,i} \end{pmatrix} = \begin{bmatrix} (m_{14,P} - u_{P,i}m_{34,P}) \\ (m_{14,P} - v_{P,i}m_{34,P}) \end{bmatrix}, \text{ and} \tag{11}$$

$$\begin{bmatrix} (u_{C,i}m_{31,C} - m_{11,C}) & (u_{C,i}m_{32,C} - m_{12,C}) & (u_{C,i}m_{33,C} - m_{13,C}) \\ (v_{C,i}m_{31,C} - m_{11,C}) & (v_{C,i}m_{32,C} - m_{12,C}) & (v_{C,i}m_{33,C} - m_{13,C}) \end{bmatrix} \begin{pmatrix} X_{W,i} \\ Y_{W,i} \\ Z_{W,i} \end{pmatrix} = \begin{bmatrix} (m_{14,C} - u_{C,i}m_{34,C}) \\ (m_{14,C} - v_{C,i}m_{34,C}) \end{bmatrix}, \tag{12}$$

where i denotes the i-th pixel; m_{ij} represents the ij-element of the transformation matrix for the projector (P) or the camera (C). Determining the projector's image coordinates $(u_{P,i}, v_{P,i})$ depends

on the number of axes used for encoding the patterns used in the pattern coding strategy [73]. For patterns encoded in both axes (e.g., 2D M-arrays) of the projection area, both projector's image coordinates ($u_{P,i}$ and $v_{P,i}$) are determined, and the world coordinates of a 3D point ($X_{W,i}$, $Y_{W,i}$, $Z_{W,i}$) are determined by solving the overdetermined system of equations, Eq. (11) and Eq. (12), using the least squares approach. When a single pattern axis (e.g., discrete and continuous time-shifting patterns) is used only $u_{P,i}$ or $v_{P,i}$ is determined, and the world coordinates ($X_{W,i}$, $Y_{W,i}$, $Z_{W,i}$) are determined by solving Eq. (12) and the appropriate equation in Eq. (11).

Figure 3 illustrates the 3D reconstruction process, for which only one pixel of the camera and one pixel of the projector are depicted. The world coordinates of a 3D surface point T' are obtained for patterns encoded in both axes by the least square solution of two non-intersecting rays form the camera and the projector pixels, Figure 3(a), or for patterns encoded in a single axis by intersecting the centered ray form the camera pixel with a vertical plane going through the center of the projector pixel, Figure 3(b). The reconstruction error is determined by obtaining the root mean square (RMS) of the error vector ($T' - T$):

$$e_{RMS} = \sqrt{(T'_x - T_x)^2 + \left(T'_y - T_y\right)^2 + (T'_z - T_z)^2}, \tag{13}$$

where T corresponds to the actual world coordinates of a 3D surface point.

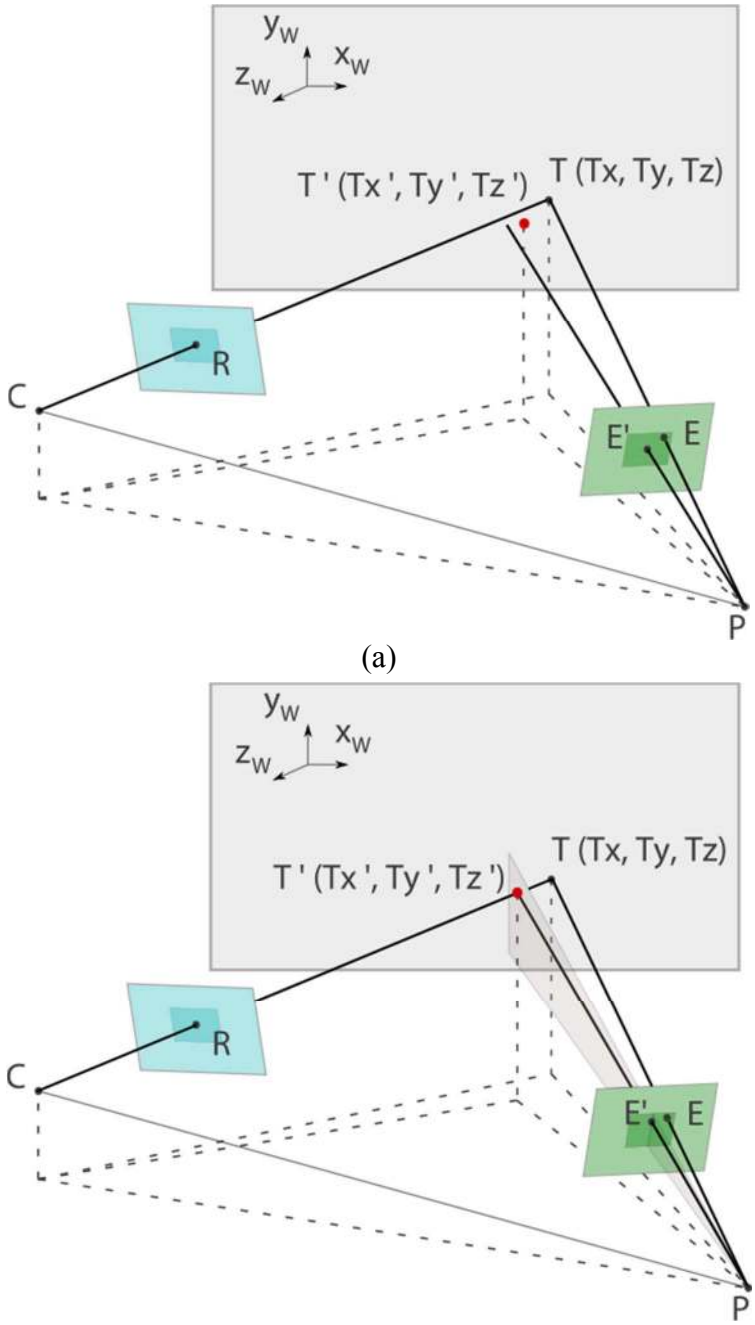

Figure 3. Model of 3D reconstruction errors of point T' (red dot) corresponding to (a) two non-intersecting rays, and (b) one ray intersecting with a plane.

3.2 Design Methodology

In this section, the generic model-based design methodology that optimizes the triangulation configuration of the hardware components of SL systems is presented. The design methodology encompasses the following steps, Figure 4: 1) design problem definition, including identification

of the design variables and performance metrics; 2) identification of design constraints; 3) simulation of system performance; and 4) optimization of the SL system configuration.

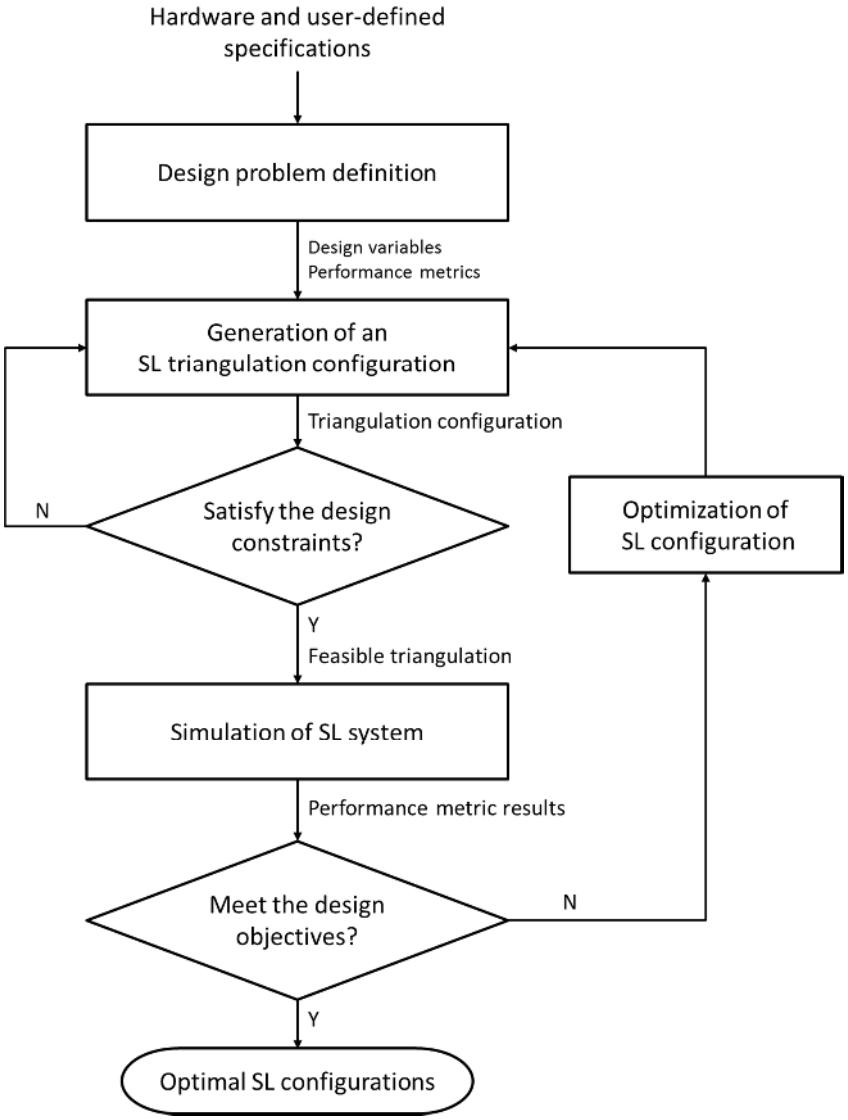

Figure 4. Proposed design methodology for SL systems.

3.2.1 Design problem definition

The first step in the design methodology is to define the design problem which is to determine an optimal SL system triangulation configuration with a given set of hardware components. To formulate this design problem, the design variables and performance metrics need to be first identified. The models presented in Section 3.1 establish a relationship between the expected reconstruction errors, and the geometric and optical characteristics of an SL system. In the proposed methodology, the six degrees of freedom of the SL configuration model are considered to be the design variables of the system.

In order to estimate the overall performance of an SL configuration for a given set of hardware components, the number of axes (N_a) used to encode the patterns in the pattern coding strategy (i.e., 1D or 2D, as discussed in Section 3.1.4) needs to be provided by the user, so that the reconstruction errors can be estimated using the appropriate model. In addition, a user-defined target size of the measurement region, hereafter called measurement volume, is specified by the user to contain the object(s) of interest to be measured. The distribution of the estimated reconstruction errors across the measurement volume is used to assess the performance of the SL system. Based on these reconstruction errors, the following performance metrics are defined: 1) the mean $\hat{\mu}_{e_{RMS}} = \frac{1}{N_s}\sum_{i=1}^{N_s} e_{RMS}^{i}$, and 2) the standard deviation $\hat{\sigma}_{e_{RMS}} = \sqrt{\frac{1}{N_s-1}\sum_{i=1}^{N_s}\left(e_{RMS}^{i} - \hat{\mu}_{RMS}\right)^2}$, of the RMS reconstruction errors for pixels with unique pixel-to-pixel correspondence; 3) the portion (η) of the projected pattern covering the measurement volume; 4) the number of 3D points (N_s) obtained from unique pixel-to-pixel correspondences between the camera and projector; and 5) the average distance from the 3D points to their nearest neighboring 3D points, referred to herein as *dispersion* (d_{N_s}). To reduce the dimensionality of the optimization problem, the five performance metrics discussed above are combined into three design objectives, namely: 1) minimize the mean and standard deviation of the reconstruction errors ($\hat{\mu}_{e_{RMS}} \cdot \hat{\sigma}_{e_{RMS}}$); 2) maximize the portion of the projected pattern covering the measurement volume as well as the number of 3D points with unique projector-camera correspondence ($\eta \cdot N_s$); and 3) maximize the dispersion (d_{N_s}) of the 3D points within the measurement volume so that they are distributed within the measurement volume, in order to better estimate the error distribution inside that volume.

3.2.2 Identification of design constraints

The second step in the proposed methodology is the identification of a set of design constraints (g) which consider practical limitations imposed on the design variables. In particular, we have included six constraints that are used to determine whether a particular triangulation configuration is feasible to implement given a set of hardware components. The design constraints consider the hardware specifications for the projector and camera optics as well as the overall footprint of the SL system. These required constraints correspond to: 1) determining that both the camera and the projector are in front of the reference plane, 2) verifying that the measurement volume is in the in-

focus region for the projection and capturing of the pattern, 3) evaluating whether the positions of the camera and the projector will cause physical interference with each other, or block the projection and capturing of patterns.

The camera and projector are required to be placed in front of the reference plane. The camera and the projector positions with respect to the reference plane are determined by evaluating the relative position of their nodal points (C and P) with respect to this plane, which is defined by its normal vector $\vec{n} = [0,0,-1]'$ and the origin of the world coordinate system O_W. This constraint can be expressed using the dot product as:

$$g(1) = \begin{cases} -1, & if\ [(C - O_W) \cdot \vec{n}] > 0\ \wedge [(P - O_W) \cdot \vec{n}] > 0 \\ 1, & otherwise \end{cases}. \quad (14)$$

In Eq. (15), the result is negative for triangulations where the camera and the projector are placed in front of the reference plane.

The reference plane needs to be placed within the range of the working distance of the optics so that the triangulation configuration can be implemented with the specified optics. Namely, the distances from the origin of the world coordinate system to the nodal points of the projector and the camera should be within the ranges of the working distances of the projector's and camera's optics; $d_{P,min}$, $d_{P,max}$, $d_{C,min}$ and $d_{C,max}$ correspond to the minimum and maximum working distances, respectively. These conditions are defined by the following design constraint:

$$g(2) = \begin{cases} -1, & if \begin{cases} \left(\|P - O_W\| > d_{P,min}\right)\ \wedge\ \left(\|P - O_W\| < d_{P,max}\right) \\ \wedge\ \left(\|C - O_W\| > d_{C,min}\right)\ \wedge\ \left(\|C - O_W\| < d_{C,max}\right), \end{cases} \\ 1, & otherwise \end{cases} \quad (15)$$

Thirdly, the user-defined measurement volume ($\mathcal{V}$) needs to be completely inside the in-focus volumes for both the projector ($\mathcal{V}_{fP}$) and the camera ($\mathcal{V}_{fC}$), which are defined by their fields of view and near and far depths of field, respectively. Both necessary conditions guarantee that the projected pattern will be in-focus for the entire measurement volume, and that the camera will capture a focused image of the pattern. This requirement can be defined in the following constraint:

$$g(3) = \begin{cases} -1, & if\ \mathcal{V} \subseteq \mathcal{V}_{fP}\ \wedge\ \mathcal{V} \subseteq \mathcal{V}_{fC} \\ 1, & otherwise \end{cases}. \quad (16)$$

Constraints evaluating physical interference are introduced to ensure that the projector and camera do not physically interfere with each other by blocking the projection and capturing of patterns and that the hardware components are placed in distinct 3D locations from each other. For determining physical obstruction of the pattern projection, it is determined whether the volume of the camera ($\mathcal{V}_C$) is inside the volume defined by the field of view of the projector, referred to as projector's viewing frustum ($\mathcal{F}_P$):

$$g(4) = \begin{cases} -1, & if\ V_C \sqcap \mathcal{F}_P = \emptyset \\ 1, & otherwise \end{cases}. \tag{17}$$

Similarly, the volume of the projector ($\mathcal{V}_P$) and the camera's viewing frustum ($\mathcal{F}_C$) are used in Eq. (18) for determining physical obstruction for pattern capturing:

$$g(5) = \begin{cases} -1, & if\ V_P \sqcap \mathcal{F}_C = \emptyset \\ 1, & otherwise \end{cases}. \tag{18}$$

Lastly, a constraint evaluates whether there is physical interference between the projector and the camera due to their 3D locations:

$$g(6) = \begin{cases} -1, & if\ V_P \sqcap V_C = \emptyset \\ 1, & otherwise \end{cases}. \tag{19}$$

3.2.3 Simulation of an SL system

The third step in the design methodology is to simulate the SL system in order to estimate the performance metrics of the system for a given triangulation configuration. This estimation process can be repeated to consider a number of feasible hardware configurations, from which an optimal triangulation configuration can be determined for a particular SL system. The measured object is modelled as a flat plane moved along the z-direction to estimate the system performance throughout the measurement volume.

3.2.4 Optimization of system configuration

The last step for the methodology is the optimization of the design. The goal of this step is to determine the *optimal* hardware configurations based on the set of aforementioned performance metrics. The overall SL hardware configuration optimization problem is defined as:

$$\min_{\vec{u}}\left(\hat{\mu}_{e_{RMS}} \cdot \hat{\sigma}_{e_{RMS}}, -\eta \cdot N_s, -d_{N_s}\right), \quad \text{subject to } g(\vec{u}) \leq 0\ , \tag{20}$$

where $\vec{u} = (z_{ref}, w, l, h, \alpha_p, \beta_p)$ is the vector of (geometric) design variables.

The minimization of Eq. (20) is performed subject to satisfying the design constraints defined in Section 3.2.2. This optimization problem can be characterized as a non-linear, highly constrained optimization problem. Due to the multi-objective nature of the optimization problem, there is not only one single optimal triangulation configuration, but a set of configurations, called the Pareto Set [74]. The Pareto set exists due to the trade-off between the multiple design objectives. Several algorithms have been proposed in the literature for multi-objective optimization problems [74]. However, discontinuous, non-linear, constrained optimization problems such as the SL system design problem discussed herein remain a challenge for these methods [75], which typically require the availability of the gradient and Hessian of the objective functions. Therefore, this work uses the derivative-free Direct Multi-Search (DMS) algorithm [75] to solve our multi-objective optimization problem due to its ability to handle such non-linear, discontinuous, constrained, multi-objective optimization problems.

In order to select from the Pareto set a single triangulation configuration to be physically implemented and calibrated with the given hardware components, the goal is to first reduce the Pareto set. A k-means clustering approach [76] is used to group together optimal triangulation configurations in the Pareto Set that have similar values for the design variables. The number of clusters for the configurations is determined by using the normalized dispersion (R^2) and Davis-Bouldin (I_{DB}) quality metrics [77-78]. The final number of clusters is selected when the change in R^2 is less than 1% and the change in I_{DB} score is less than 5%. This clustering of optimal SL system configurations allows only for distinct configurations with respect to the design variables to be considered.

3.3 Summary

In this chapter, a novel design methodology for determining optimal triangulation configurations for SL sensory systems has been presented. The proposed methodology optimizes the triangulation

configurations between the projector, the camera and a measured object, for a given set of performance metrics, while satisfying design constraints based on hardware and user-defined specifications. Due to its generality, the design methodology can be used to design an optimal SL system for any given set of hardware components to measure objects within a target measurement volume. The design methodology allows for the optimization of 3D triangulation configurations regardless of the specific pattern coding strategy that is to be implemented.

Chapter 4
Design Methodology for Optimizing SL Pattern Sequences

In this chapter, the detailed procedure of the design methodology for phase unwrapping of multi-fringe sinusoidal phase-shifted patterns is presented in order to determine the *optimal sequence* of fringe patterns that reduce measurement errors. The pattern sequence methodology considers a multi-variable model to determine the random noise in the absolute phase of a measured 3D object as a function of the number of fringes, the random noise in the relative phase and the random noise in absolute phase used in each unwrapping step. The proposed methodology is novel in that it is able to determine both the overall number of unwrapping steps required and the number of fringes in each pattern at each step in order to minimize the resulting random noise in 3D measurements.

4.1 Sinusoidal Phase-Shifting SL Technique

Our research considers SL sensory systems using a phase-shifting technique with sinusoidal patterns in order to obtain 3D reconstruction of objects. This section presents an overview of the steps used in the sinusoidal phase-shifting technique in order to obtain 3D reconstruction prior to a detailed discussion on the pattern sequence methodology.

4.1.1 Sinusoidal Phase-Shifting Techniques

Sinusoidal phase-shifting techniques utilize a sequence of phase-shifted patterns with a sinusoidal intensity profile in order to determine the projector-camera pixel correspondence. The intensity profile of the sinusoidal pattern is designed based on one frequency, which is phase-shifted by a factor of $2\pi/N_S$ for generating every projection of the sequence, where N_S corresponds to the total number of projections. The intensity profile I_i^P of a projected pattern is given by [51]:

$$I_i^P(x^P, y^P) = I'(x^P, y^P) + I''(x^P, y^P)\cos\left(\phi^P(x^P, y^P) - \frac{2\pi p_i}{N_S}\right), \qquad (21)$$

where P is the projection pattern; $p_i = 0,1, \dots, N_S - 1$ represents the ith shifted pattern; I' is the average intensity; I'' is the intensity modulation; $\phi^P(x^P, y^P)$ is the relative phase value between 0 and 2π at the (x^P, y^P) projection coordinates; and $2\pi p_i/N_S$ represents equally distributed phase-shifts to cover the entire period. Figure 5(a) shows a pattern with 5 fringes projected onto a propeller where each fringe corresponds to a sinusoidal intensity profile in gray scale.

The captured intensity profile I_i^C for a shifted pattern can be expressed for each pixel as [51]:

$$I_i^C(x^c, y^c) = \alpha(x^c, y^c)\left[I'(x^c, y^c) + I''(x^c, y^c)\cos\left(\phi^c(x^c, y^c) - \frac{2\pi p_i}{N_S}\right)\right], \qquad (22)$$

where $\alpha(x^c, y^c)$ is the effect of the surface reflectivity of the object and $\phi^c(x^c, y^c)$ is the relative phase value at the (x^c, y^c) camera coordinate. For simplicity, the relative phase $\phi^c(x^c, y^c)$ will be denoted as $\phi^c(x, y)$ hereafter. Hence, all further references to pixel coordinates (x, y) represent coordinates in the camera coordinate frame.

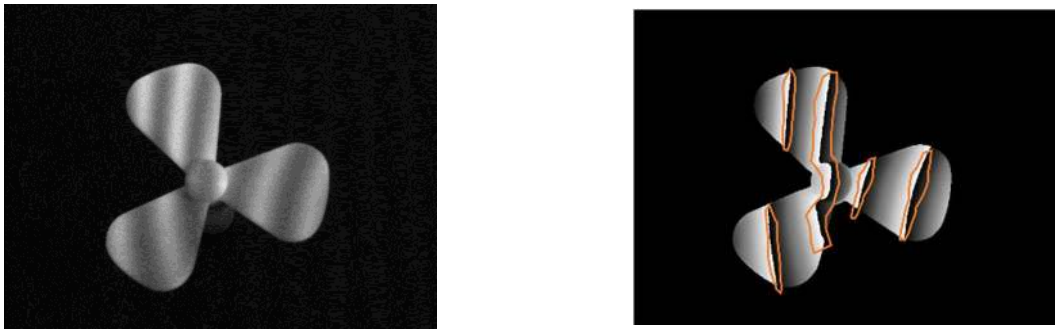

(a) (b)

Figure 5. (a) Pattern with 5 fringes projected onto the blades of a propeller, and (b) relative phase map with discontinuities at fringe boundaries highlighted in orange.

Based on the captured patterns, a relationship exists to determine the relative phase value of each pixel. For sinusoidal intensity profiles using three phase-shifted patterns ($N_S = 3$), as is used in our thesis, the relative phase of each camera pixel is given by:

$$\phi^c(x, y) = arctan\left\{\frac{\sqrt{3}\cdot[I_1^C(x,y) - I_3^C(x,y)]}{2\cdot I_2^C(x,y) - I_1^C(x,y) - I_3^C(x,y)}\right\}, \qquad (23)$$

where I_1^C, I_2^C, I_3^C correspond to the intensity of the three phase-shifted patterns, respectively. Figure 5(b) presents the relative phase map, consisting of varying shades of gray for different phase values, obtained by Eq. (23) for the pattern of 5 fringes shown in Figure 5(a). Given that the relative phase is based on intensity profiles, the random noise in intensity can introduce random noise in the relative phase obtained from captured patterns [49]. This random noise is a result of the random perturbations of ambient light and/or of the projected light pattern, camera quantization noise, among other noise sources [51].

4.1.2 Active Phase Unwrapping

The relative phase map obtained from the three phase-shifted patterns is periodic, with phase jumps (discontinuities in relative phase) at the boundaries between fringes as highlighted in Figure 5(b). This results in potentially multiple pixels in different regions of the phase map image having the same phase value. In order to identify the unique correspondence for each projector-camera pixel pair, active phase unwrapping algorithms are used to remove the phase discontinuities between fringes by adding integral multiples of 2π to the relative phase [31, 43, 47]. The resulting unwrapped phase values are known as absolute phase values.

To remove the discontinuities in relative phases, a commonly used active phase unwrapping approach can be implemented which utilizes the absolute phase from a single fringe pattern to determine the fringe number of each pixel in the phase map image [43, 49]. Since a single fringe pattern covers the entire field of view of an object of interest with only one fringe, it does not introduce phase discontinuities and can provide non-periodic information to unwrap the multi-fringe pattern (e.g., the five fringes in Figure 5). Given a set of phase-shifted captured patterns with n_f fringes, and a set of phase-shifted patterns with one fringe, the absolute unwrapped phase of a pixel is obtained by [49]:

$$\Phi_{n_f}^{C}(x,y) = 2\pi\, Round\left[\frac{n_f \cdot \Phi_1^{C}(x,y) - \phi_{n_f}^{C}(x,y)}{2\pi}\right] + \phi_{n_f}^{C}(x,y), \tag{24}$$

where $\phi_{n_f}^{C}$ corresponds to the relative phase of the multi-fringe pattern with n_f fringes, and Φ_1^{C} is the absolute phase of the single fringe pattern. Note that the absolute phase $\Phi_{n_f}^{C}(x,y)$ obtained from Eq. (24) at any given pixel (x,y) depends only on the phase values of the aforementioned fringe patterns at that pixel, without requiring information from neighboring pixels, i.e., the 3D reconstruction at a given pixel is independent of its neighbors. This is an important feature of active phase unwrapping that significantly reduces the processing time required for 3D reconstruction.

The absolute phase from the multi-fringe pattern determines the pixel position for each camera pixel with respect to the projector, which in turn defines the projector-camera correspondence required to obtain the 3D reconstruction of an object of interest. However, due to the triangulation configuration used between the projector, camera and the object of interest, the projector and

camera pixels may not have a perfect one-to-one correspondence. This means that the phase value for each camera pixel could be a function of the phase values of multiple projector pixels, since one projector pixel could be captured by more than one camera pixel (resulting in repeated measurements of the same phase value) and/or one camera pixel may (partially) capture multiple projector pixels. This source of intensity noise also contributes to the phase unwrapping errors.

Due to the importance of accurately unwrapping relative phase values in order to obtain high-precision 3D reconstruction, sequential approaches for active phase unwrapping have been proposed [47, 50]. In this context, the phase unwrapping achieved through Eq. (24) is referred to as an *active phase unwrapping step*. Sequential active phase unwrapping can use multiple phase unwrapping steps, i.e., in succession using the resulting absolute phase from a previous unwrapping step to unwrap the relative phase values from a pattern with a larger number of fringes, where the number of unwrapping steps are more than one [47]. The absolute phase obtained from such sequential phase unwrapping is known to reduce the random noise in 3D reconstruction [50].

4.1.3 3D Reconstruction

The 3D reconstruction model of the SL sensory system defines the relationship between a 3D point on the surface of an object and its projector-camera pixel correspondence. In this work, as discussed in Chapter 3, the 3D reconstruction model is determined based on Eqs. (9) and (10), which relates the parameters for the triangulation configuration of the hardware and the pinhole models used for the projector and the camera.

4.2 Pattern Sequence Methodology

A novel, generic methodology is developed to determine the set of multi-fringe patterns required for an SL system in order to accurately measure the 3D surface profiles of objects when sequential active phase unwrapping is used. The set of patterns encompasses a temporal sequence of patterns of multiple fringes with sinusoidal intensity profiles. The number of fringes used in each pattern in the set is selected within the methodology such that the random noise in the absolute phase is subsequently reduced during each phase unwrapping step. This in turn reduces the 3D measurement errors that are a direct result of this noise. The proposed three-step methodology is presented in Figure 6. The first step is to determine the set of fringes that can be projected with a given sensor hardware resolution. Then, the second step estimates the random noise in relative

phase for the sensor hardware set-up. Lastly, the third step identifies the set of multi-fringe patterns which reduce the random noise in the absolute phase of a measured 3D object. The following subsections describe in detail each step of the methodology.

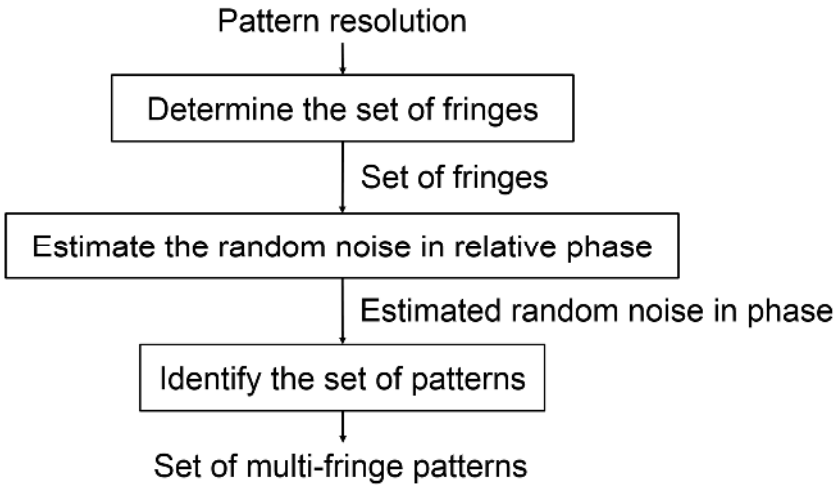

Figure 6. Proposed design methodology for SL pattern sequence.

4.2.1 Step 1: Determine the Set of Fringes

The first step of the methodology consists of determining the set of fringes to be investigated for defining the optimal sequence of the multi-fringe patterns. This set is defined by the required pattern coding resolution of the SL system. For a given projection area of R pixels consisting of M by N pixels, the coding pattern resolution is the number of pixels along the coding axes (vertical and/or horizontal) in which the pattern is varying. For time-multiplexed phase-shifted patterns, the sinusoidal intensity profile is encoded along only one coding axis, typically the horizontal axis, in which both the camera and the projector have the highest resolution. Without loss of generality, let us assume that the camera sensor has a resolution that is equal to or greater than that of the projector, let N be the number of pixels of the projector in the axis of the highest resolution (i.e., the horizontal direction). Hence, the number of fringes, n_f, within the multi-fringe pattern set to be projected is defined based on the projection resolution, i.e., number of pixels (N). The largest number of fringes to be considered corresponds to a discretized sinusoidal pattern with at least 5 pixels per fringe along the horizontal axis to avoid spatial aliasing of the peaks and troughs of the sinusoidal intensity profile. Furthermore, in order to apply sequential phase unwrapping, the multi-fringe patterns in the set are required to encode the entire N pixels along the coding axis, i.e., the number of fringes of the multi-fringe patterns must be an exact divisor of the N pixels. Hence, the

set of fringes to be evaluated is defined as $\mathbb{S}_n = \{n_f\}$ where n_f corresponds to the number of fringes that satisfy the following conditions: 1) $n_f \in \{1,2, \dots, N/5\}$, and 2) $N \bmod n_f = 0$.

4.2.2 Step 2: Estimate the Random Noise in Relative Phase

The second step of the methodology focuses on estimating the random noise that is present in the relative phase values. Since relative phase is determined based on intensity values, the random perturbations in intensity will result in random noise in relative phase [49, 51]. Hence, the effect of the intensity noise on the relative phase needs to be investigated for the set $\mathbb{S}_n$.

The relative phase values of the fringe patterns are obtained for the corresponding patterns via Eq. (23). The statistical properties of the random noise in relative phase can be estimated from the distribution of phase values from repeated measurements. This random noise is considered to be a zero-mean Gaussian random variable [51]. Its standard deviation $\hat{\sigma}_{\phi_{n_f}^C}$, which is used as a quantitative measure of the noise level, can be estimated as the average of the standard deviations of the phase values across all pixels [51].

In [51], it was shown that $\hat{\sigma}_{\phi_{n_f}^C}$ is proportional to the random noise in intensity and inversely proportional to the intensity modulation and the number of shifted patterns, while being independent of the number of fringes. Hence, the relative phase from a single fringe pattern is used to estimate $\hat{\sigma}_{\phi_{n_f}^C}$ by taking repeated measurements of a flat plane placed at the center of the measurement volume of the SL system. The estimated random noise of the relative phase is obtained by:

$$\hat{\sigma}_{\phi_{n_f}^C} = \sqrt{\frac{1}{N_T - 1} \sum_{i=1}^{N_T} \left(\Phi_1^{C,i} - \hat{\mu}_{\Phi_1^C} \right)^2}, \tag{25}$$

where $\hat{\mu}_{\Phi_1^C} = \frac{1}{N_T} \sum_{i=1}^{N_T} \Phi_1^{C,i}$, and $\Phi_1^{C,i}$ corresponds to the measured phase values obtained from Eq. (23) for a single fringe pattern ($n_f = 1$). $N_T = R \cdot N_m$ is the total number of phase values measured, which is obtained by measuring R number of pixels of the projected pattern in N_m measurement repetitions.

4.2.3 Step 3: Identify the Set of Patterns

The third step of the methodology consists of identifying the set of patterns needed to minimize the effect of the random noise in relative phase on the resulting absolute phase in order to reduce the random noise in the 3D measurements. The goal is to achieve an unwrapping approach that is both robust to random noise in phase and efficient with respect to unnecessarily increasing the number of required pattern images of the target object. Hence, the active phase unwrapping procedure is simulated, in order to analyze the effect of $\hat{\sigma}_{\phi_{n_f}^C}$ on the resulting absolute phase. Namely, the simulation is used to determine: 1) the influence of the numbers of fringes of the multi-fringe patterns on the random noise in the resulting absolute phase during sequential phase unwrapping, and 2) the pattern sequence that decreases the noise effect on the resulting absolute phase. In order to model sequential active phase unwrapping, the absolute phase from the previous unwrapping step $(k-1)$ is used as the reference phase $\Phi_{ref}^{C,k-1}(x,y)$ for the current step k:

$$\Phi_{n_f}^{C,k}(x,y) \;= 2\pi\, Round\left[\frac{n_f \cdot \Phi_{ref}^{C,k-1}(x,y) - \phi_{n_f}^{C}(x,y)}{2\pi}\right] + \phi_{n_f}^{C}(x,y), \tag{26}$$

where $\Phi_{n_f}^{C,k}$ is the absolute phase at the current phase unwrapping step resulting from the relative phase $\phi_{n_f}^{C}$ of a pattern with n_f fringes. The effect of the random noise introduced during phase unwrapping is simulated for the set of fringes by: 1) adding random noise to the ideal phase values, i.e., phase values used for generating the patterns with single and multiple fringes; 2) determining the absolute phase using active phase unwrapping for the set of multi-fringe patterns; and 3) determining the standard deviation of the resulting absolute phase when varying the random noise level.

In order to simulate the phase values from the captured patterns, first the ideal (noise-free) relative phase values are simulated assuming a one-to-one projector-camera pixel correspondence. Hence, the ideal relative phase values for a multi-fringe pattern are determined by:

$$\phi_{n_f}^{P} = \frac{(j \bmod p_f) - 1}{p_f - 1} 2\pi, \tag{27}$$

where $j = 1, \dots, N$ is the pixel number, and $p_f = N/n_f$ corresponds to the number of pixels per fringe. The ideal reference absolute phase for any k step Φ_{ref}^P is simulated using the absolute phase of a single fringe pattern:

$$\Phi_{ref}^P = \frac{j-1}{N-1} 2\pi. \tag{28}$$

Then, the relative and reference phase values captured by the camera, i.e., $\tilde{\phi}_{n_f}^C$ and $\tilde{\Phi}_{ref}^C$, are generated by adding white random noise to the ideal phase values in Eqs. (27) and (28). This corresponds to adding a Gaussian variable for the noise (w_n) with zero mean and standard deviation ($\hat{\sigma}_{\phi_{n_f}^C}$), i.e., $w_n \sim N\left(0, \hat{\sigma}_{\phi_{n_f}^C}{}^2\right)$:

$$\tilde{\phi}_{n_f}^C = \phi_{n_f}^P + w_n, \tag{29}$$

$$\tilde{\Phi}_{ref}^C = \Phi_{ref}^P + w_n. \tag{30}$$

As a result of noise in the reference and relative phase values, the absolute phase $\tilde{\Phi}_{n_f}^C$ is also a random variable, which can be considered Gaussian [51]. Its standard deviation is estimated by Monte Carlo simulation, namely, randomly generating a predefined number (N_s) of realizations of the random variable of the absolute phase $\tilde{\Phi}_{n_f}^C$ and comparing them with the ideal absolute phase values $\Phi_{n_f}^P$ to estimate the standard deviation of the differences. To consider the effect of uncertainty in the noise level that can be caused by for example, varying ambient illumination, object albedo and object geometry, the simulation process is repeated for varying noise levels of $\sigma_{\phi_{n_f}^C}$, within a range defined as $0 < \sigma_{\phi_{n_f}^C} < \eta\, \hat{\sigma}_{\phi_1^C}$, for $\eta > 1$. This proposed approach ensures that the selected patterns are simultaneously optimal for a range of noise levels.

The simulated distribution of the absolute phase values characterizes how the random noise in the relative phases results in random noise in the absolute phase during active phase unwrapping, i.e., the effect of $\sigma_{\phi_{n_f}^C}$ and $\sigma_{\Phi_{ref}^C}$ on $\sigma_{\Phi_{n_f}^C}$. A simulation study of the trend behavior of Eq. (26) with varying levels of input noise suggests that there is a monotonic increase in the resulting noise in absolute phase as the noise level increases in the relative and reference phase values. For low noise

levels of $\sigma_{\phi^C_{n_f}}$ and $\sigma_{\Phi^C_{ref}}$ the rate at which the noise level increases in the relative and reference phases propagates to the absolute phase is an inverse function of the number of fringes as defined in Eq. (26). However, this trend is no longer valid after a certain noise level after which the random noise in relative phase is amplified by the number of fringes. This noise level depends on the noise level of the reference phase, the noise level of the relative phase, the number of fringe of the multi-fringe patterns, and the number of pixels used for the pattern discretization. This characterization suggests that the number of fringes should be increased to reduce the noise in the unwrapped phase values, but also suggests that it cannot be increased indiscriminately without causing an increase in the noise levels. These conflicting trends indicate the existence of an optimum, i.e., a specific number of fringes for which the noise level is minimized within the input noise range considered. Based on this characterization, it is proposed a criterion for selecting the number of fringes that minimizes the noise level as that which minimizes the norm of the gradient of the random noise of the absolute phase:

$$\arg\min_{nf} \iint \left\| \nabla \sigma_{\Phi^C_{n_f}} \right\|^2 d\sigma_{\Phi^C_{ref}}\, d\sigma_{\phi^C_{n_f}}, \tag{31}$$

where $\left\| \nabla \sigma_{\Phi^C_{n_f}} \right\|^2$ corresponds to the L_2-norm of the gradient of $\sigma_{\Phi^C_{n_f}}$. The L_2-norm of the gradient is integrated over the range of noise levels.

As previously described, in sequential active unwrapping the unwrapped absolute phase values are used as the reference phase for the next unwrapping step, i.e., $\Phi^C_{ref,step2} = \Phi^C_{ref,step1}$. To determine the number of fringes required for this next step of unwrapping, the same approach as described above is utilized by using the obtained absolute phase from the previous step as the reference phase. Namely, Eq. (31) is used for simulating the unwrapping process but with a reduced variance of the noise in reference phase, i.e., with $\sigma_{\Phi^C_{n_f,step2}} = \sigma_{\Phi^C_{n_f,step1}}$. In other words, although the noise in the relative phase remains unchanged because it is the result of image intensity noise, the noise in the reference phase used for the simulations is lower as it has been reduced by the previous active unwrapping step. Sequential phase unwrapping is repeated until the improvements in reducing the random noise in the absolute phase is less than 1%, i.e.,

$$\left\| \frac{\sigma_{\Phi^C_{n_f,step_k}} - \sigma_{\Phi^C_{n_f,step_{k-1}}}}{\sigma_{\Phi^C_{n_f,step_{k-1}}}} \right\| \leq 0.01. \quad (32)$$

4.3 Summary

In this chapter, a novel pattern sequence methodology for SL sensory systems is presented in order to effectively determine the optimal set of multi-fringe patterns needed to obtain accurate 3D reconstruction of objects. This methodology simultaneously determines the number of patterns needed as well as the number of fringes within these patterns in order to minimize measurement errors. The novelty of the proposed design methodology is that: (1) determines the optimal pattern sequence and the optimal number of fringes for each pattern in the sequence, and (2) obtains the highest measurement accuracy by minimizing 3D reconstructions errors.

Chapter 5
Design Methodologies for Micro-Scale Measurements

In Chapters 3 and 4, design methodologies for the hardware configuration and pattern sequences for SL systems were presented. These methodologies, formulated for SL systems for macro-scale measurements, cannot directly be applied to micro-scale measurement systems. In this chapter, the design methodologies for SL systems for micro-scale measurements consider the shallow depth of field of the microscope lenses used when optimizing the system configuration and the pattern sequence. A sinusoidal phase-shifting technique is used with an image focus fusion approach to generate in-focus images within a larger measurement volume than would otherwise be possible using microscope lenses. Furthermore, a novel calibration approach is proposed for this system, which leverages robust regression methods and model selection metrics to obtain a calibration model with minimum prediction errors for a given calibration data set, which can be utilized to determine 3D points over the entire measurement volume.

5.1 Structured-Light with Image Focus Fusion

In order to measure small objects in the micro-scale (0.5 – 10 mm), SL sensory systems with microscope lenses are used to reduce the size of the fringe patterns projected onto the micro-scale part, and also to magnify the pattern deformation captured by the camera sensor [18, 56, 59]. The limited depth-of-field (DOF) of the microscope lenses used by the camera and projector limits the measurement volume to a very shallow region, Figure 7(a), where the captured deformed patterns are in-focus [79], thus severely restricting the type and overall size of the objects that can be measured. To overcome the limited DOF of the microscope lenses, this thesis builds upon the novel approach for SL measurement of micro-scale objects developed in [80-81] by other members of our research group which uses focus fusion methods to combine images taken at different focus settings, in order to obtain all-in-focus images of the deformed fringe patterns over a larger measurement volume, Figure 7(b). In addition, a novel calibration procedure for these systems based on a calibration model valid for the entire measurement volume was developed.

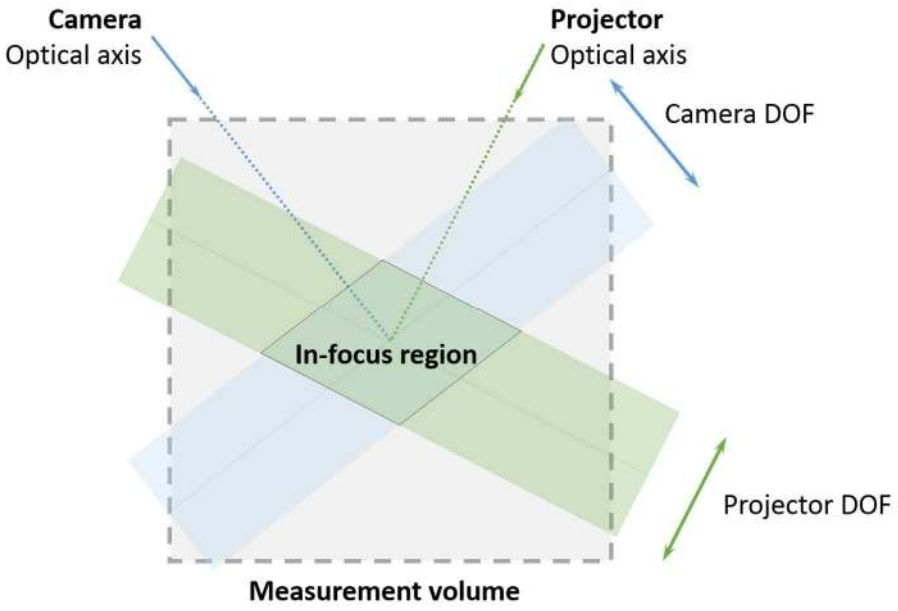

(a)

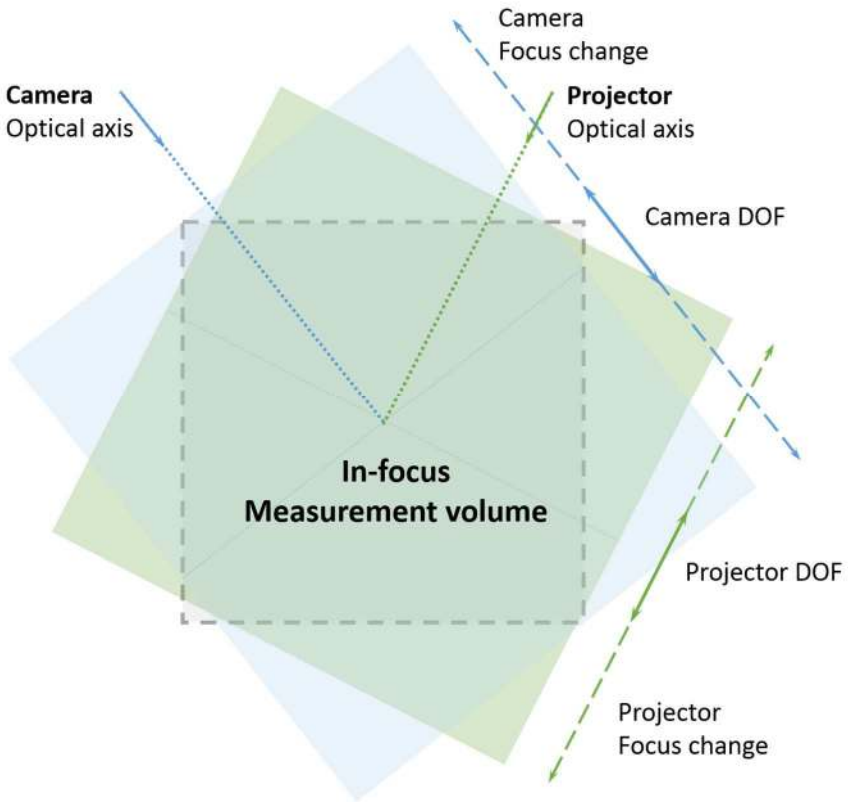

(b)

Figure 7. Top view schematic representation of the measurement volume and the in-focus region of the camera and projector (a) without and (b) with image focus fusion, respectively.

5.1.1 Focus Fusion

Image focus fusion is a digital post-processing technique that combines multiple images, taken at different focus levels, in order to generate a single resulting all-in-focus (AIF) image with a greater DOF than any of the individual source images [82]. The focus fusion technique is generally used in the fields of macro-photography and microscopy where the DOF is limited by the optics. In this thesis, the use of image focus fusion is proposed to overcome the small in-focus region caused by the shallow DOF of the microscope lenses, shown in Figure 7. Namely, a novel measurement approach is proposed by incorporating image focus fusion techniques into the SL system measurement [80-81], with the goal of obtaining an image where all the features of the measured objects are focused.

The starting point for focus fusion algorithms is a set of images of the same scene captured with different focus settings, i.e., with different focal lengths. Based on this image set, focus fusion algorithms typically consist of three stages: calculating a focus measure, selecting the focused regions of each image in the set, and image fusion [83]. First, the square of the gradient of image intensities is calculated for all pixels and used as a focus measure. Second, the regions in each image with the highest focus measures are selected to form part of the final AIF image. Finally, the focused regions of each image are aligned and combined to generate the AIF image, typically using a weighted average approach.

In SL systems that use image focus fusion for micro-scale measurements, the target object is placed at the reference position. Then, to measure the 3D surface profile of this micro-scale object, the projector and camera scan through the part with sequential focus steps along their optical axes, projecting the designed light patterns onto the object and capturing their deformation caused by the object surface profile. Once all images are obtained, the images corresponding to the same projected pattern but with different focus levels are fused to obtain a set of AIF images, one for each pattern. In order to minimize noise in the fused image that could be caused by camera noise and system vibration, an image alignment algorithm was combined with a selective image fusion algorithm that is robust to noise [77]. In particular, the Selective All-in-Focus (SAF) algorithm [83] is used to create the AIF images.

5.2 Design Methodology for SL System Configurations for Micro-Scale Measurements

As discussed in Chapter 3, the triangulation configuration between the camera, projector and the measured part has a significant influence on the resulting measurement accuracy. In this context, it was also discussed how implementation-related issues such as physical interference, working distances of the lenses, FOV and DOF, impose a set of geometrical constraints that significantly limit design choices. Hence, the first step in the system setup and calibration of an SL system for micro-scale measurements is the design of the hardware triangulation configuration.

The design methodology presented in Chapter 3 is adapted and described in this section. Figure 8 shows the methodology for designing the triangulation configuration of SL systems for micro-scale measurements. The full design methodology described in Section 3.2 is not directly applicable, for two reasons. First, the implementation of focus fusion methods to increase the size of the measurement volume for micro-scale measurements requires that the focal length (f) of the optics varies during projection and capturing. In consequence, the ray tracing model presented in Section 3.2.3 as part of the design methodology, which is formulated for a constant focal length, is no longer valid. Second, the shallow depth of field and short working distance of the microscope lenses must be considered when modelling the triangulation configuration between the measured object, camera and projector. The triangulation model with these new optical specifications makes the geometric constraints (FOV/DOF overlap, physical interference) the critical consideration for the triangulation design.

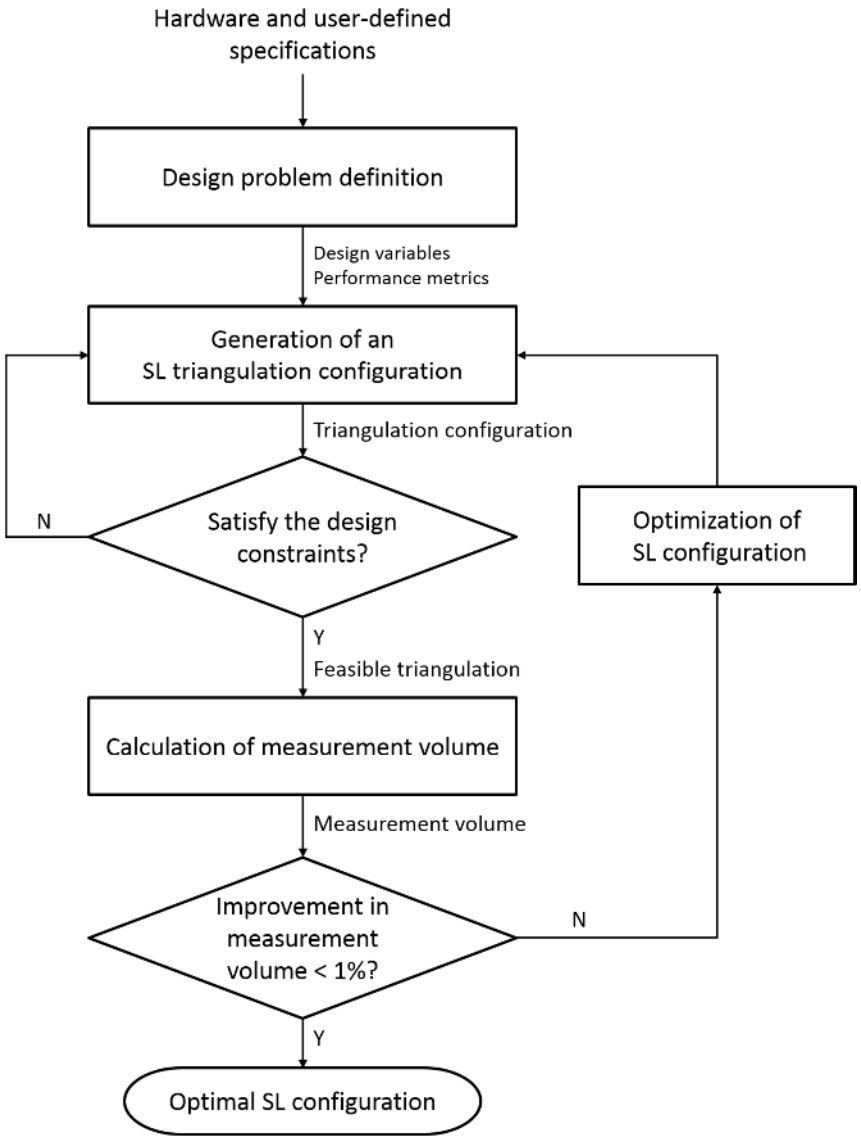

Figure 8. Proposed design methodology for SL system configuration for micro-scale measurements.

As shown in the flowchart in Figure 8, the optimization objective for the SL system for micro-scale measurements is redefined to be maximizing the size of the measurement volume. The hardware triangulation configuration for the SL system for micro-scale measurements was designed using only the geometric constraint models described in Section 3.2.2. In other words, the system triangulation was designed to maximize the overlap between the FOV and DOF of the camera and projector optics, while considering the design constraints defined by practical limitations of the hardware components.

5.3 Design Methodology for Optimizing SL Pattern Sequences for Micro-Scale Measurements

The reduction in random noise in phase values obtained by the sequential unwrapping of the optimal pattern sequence is of particular importance during the calibration procedure for micro-scale measurements. As Section 5.4.4 will show that pixel-to-pixel correspondences, which are estimated from phase values, can introduce significant errors in the calibration data. Hence, the novel design methodology described in Chapter 4 is used for optimizing pattern sequences for SL measurement micro-scale measurements. However, a slight modification on the way of estimating the random noise in phase of SL systems using microscope lenses since the random noise in phase for such systems also vary with the number of fringes.

The adapted design methodology for SL systems for micro-scale measurements is presented in Figure 9. Similar to the methodology described in Chapter 4, this methodology is used to determine the optimal pattern sequence. To this end, the first step is to determine the set of fringes $\mathbb{S}_n$ that will be considered for designing the pattern sequence. The second step of the methodology is modified in order to estimate the noise in phase values caused by random noise in image intensity, based on noise in phase for fringe patterns with all the number of fringes in the set $\mathbb{S}_n$. In addition, to take into account the effect of shallow DOF of microscope optics, e.g., the noise introduced by unfocused images, the noise in phase values is determined at different z-positions within the target measurement volume. The end result of this process is a full characterization of the noise in phase values, as a function of z-position and the number of fringes of the pattern projected. This comprehensive characterization of the noise in phase values provides the information required to proceed with simulations of the sequential unwrapping process. After the noise in phase values is fully characterized, the rest of the steps of the pattern sequence design methodology are conducted without any further modifications.

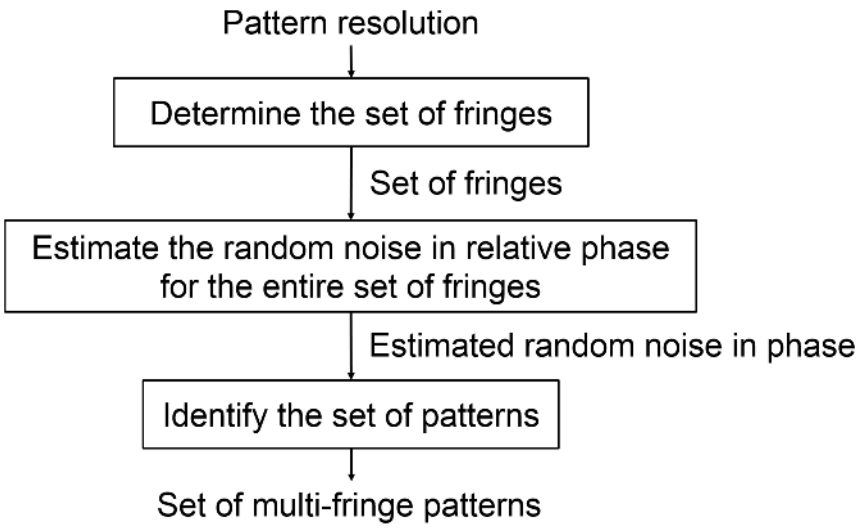

Figure 9. Proposed design methodology for SL pattern sequence for micro-scale measurements.

5.4 Calibration Procedure

The goal of the calibration procedure is to determine the coefficients of the calibration model that are valid for measuring objects within a target measurement volume [62]. The calibration data used for obtaining the model parameters is obtained by imaging a planar calibration object placed at different positions within the target measurement volume [42]. The calibration object features a grid of markers with known, certified dimensions and spacing, and it is mounted on a 3-axis translational precision stage.

In order to calibrate an SL sensory system, the calibration procedure presented in Figure 10 is used. Namely, in order to obtain the calibration data, a planar calibration object is moved within the measurement volume and imaged using the optimal pattern sequence determined following the design methodology described in Section 5.3. The calibration procedure consists of: 1) taking several images with multiple focus levels for each pattern and a fully-illuminated image, 2) generating all-in-focus captured patterns, 3) detecting the object features (calibration markers) in the fully-illuminated image in the camera image coordinate frame, 4) re-mapping the obtained features to the projector image coordinate frame using the phase obtained from the patterns, and 5) fitting and selection of the model with the lowest prediction errors for the calibration data.

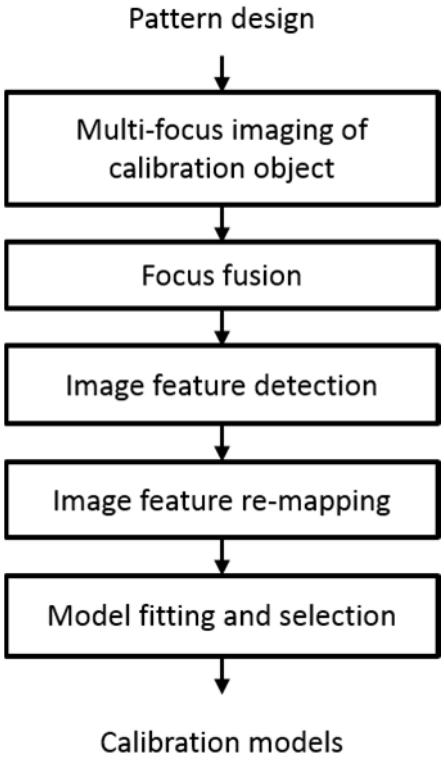

Figure 10. Procedure for calibration of the SL system for micro-scale measurements.

A world coordinate frame needs to be defined as a fixed reference coordinate system to describe the position of the measured objects within the measurement volume of the SL system. The calibration plane is placed vertically on a 3-axis stage, i.e., with the normal of the plane aligned with the depth movement which coincided with the z-axis. The x, y and z directions of the world coordinate frame are aligned with the movement of the stage in the vertical, horizontal and depth (perpendicular to the xy plane) directions, respectively, following the right-hand rule. The origin of the world coordinate frame is defined to be the top left marking of the calibration object when placed at the farthest position from the camera.

5.4.1 Multi-focus Imaging of the Calibration Object

During the calibration procedure, the calibration object is gradually moved with a fixed step along the z-axis, starting from the farthest position ($Z_W = 0$) to the closest z-position to the sensory system. Then, the plane is returned to the $Z_W = 0$ position, moved with a fixed step in the y-direction, and then followed by another set of incremental, fixed-step movements in the z-direction.This procedure is repeated multiple times so that the calibration object markers form a

dense grid within the measurement volume. The rationale for moving the object back to the $Z_W = 0$ position before performing lateral translations is to avoid positioning errors due to backlash in the precision stages.

At each position of the calibration object, the fringe patterns are projected and captured using different focus settings of the optics. This ensures that each region of the measured object has been captured, in focus, illuminated for each pattern. In addition, fully illuminated images (with no fringes) are captured at the same set of focus settings; these images are used during the focus fusion step, described next. The end result of this process is a set of $n_{focus} \times (n_{patterns} + 1)$ images, where n_{focus} is the number of focus settings and $n_{patterns}$ is the number of fringe patterns, incremented by 1 to account for the fully illuminated images.

5.4.2 Focus Fusion

After the images have been captured, a post-processing step is performed to fuse images from multiple focus settings into a single, AIF image for each fringe pattern. First, fully illuminated images of the calibration object captured under different focus settings are fused with the Selective All-in-Focus (SAF) algorithm [83], a step that identifies and maps each region of the final AIF image to one or more of the input images in which this region is in focus. In this thesis, the images captured for each pattern are fused using the same focused region mapping that resulted from the fusion of the fully illuminated images. By reusing the focused region mapping from the fully illuminated images to fuse the images of the fringe patterns, the computational cost of the focus fusion procedure is reduced. Furthermore, the use of fully illuminated images as a base for focus fusion reduces potential errors that may be introduced in the focused region mapping by the varying illumination of the fringe patterns.

5.4.3 Image Feature Detection

The calibration data set consists of the coordinates of calibration object markers defined in the image camera and projector coordinate systems (u_C, v_C, u_P, v_P) as well as their 3D coordinates (X_W, Y_W, Z_W) in the world coordinate system. For each calibration object position, the set of fringe patterns and a fully-illuminated image are projected onto the planar calibration object, and images are captured using a range of focus levels. The images are then combined to obtain AIF images using the focus fusion algorithm explained in Section 5.4.2.

The AIF, fully-illuminated image is used to determine the image camera coordinates (u_C, v_C) of each marker at each z-position using automated feature detection algorithms. A Hough Transform [83] is used in this work to identify the image coordinates of the calibration object markers, due to its robustness to the presence of noise in the images.

The final result of the image feature detection step is a data set of n_{calib} points, containing the world coordinates of the calibration object markers ($X_{W,k}$, $Y_{W,k}$, $Z_{W,k}$), known from the position of the motion stages, and the image coordinates of these points in the camera sensor ($u_{C,k}$, $v_{C,k}$), $k = 1, \dots, n_{calib}$, determined from the captured images through the automated detection procedure.

5.4.4 Image Feature Re-mapping

Previous steps of the calibration procedure have resulted in a data set ($X_{W,k}$, $Y_{W,k}$, $Z_{W,k}$, $u_{C,k}$, $v_{C,k}$), $k = 1, \dots, n_{calib}$, containing the world and image coordinates of the calibration object markers. To complete this calibration data set, however, the image coordinates of the calibration object markers in the projector panel ($u_{P,k}, v_{P,k}$) must be determined. In [80], the viewpoint re-mapping technique was used to generate the projector viewpoint of the image, using the pixel-to-pixel correspondences obtained from the absolute phase values of each pixel to generate a full synthetic image of the scene from the viewpoint of the projector. After synthetic images of the projector view of the calibration object are obtained through viewpoint re-mapping, the image feature detection procedure was conducted on these images to determine the location of the calibration object markers in the projector panel [80-81].

However, the projector viewpoint images obtained through re-mapping usually are of lower quality than the camera images, due to the effects of triangulation geometry, image noise, and errors in the pixel-to-pixel correspondences. These viewpoint re-mapping errors can reduce the accuracy of the image feature detection procedure, thus introducing errors in the calibration data. To address this issue, a novel approach for re-mapping is introduced, which focuses only on re-mapping the coordinates of the calibration object markers that were detected in the (more accurate) original images. In other words, the feature detection algorithms are used only on the original AIF images, which are taken from the viewpoint of the camera. Then only the coordinates of the calibration object markers are remapped to the projector viewpoint, without the need for further feature detection.

For the k-th calibration object marking, its coordinates in the projector panel, $(u_{P,k}, v_{P,k})$, are determined by first identifying the absolute phase values $(\Phi_{H,k}, \Phi_{V,k})$ that correspond to the image coordinates of the markers $(u_{C,k}, v_{C,k})$ in the camera. Feature detection algorithms determine the image coordinates of the markers with subpixel accuracy (i.e., pixel coordinates are real numbers, not integers), while the absolute phase values are only available at integer pixel coordinates in the camera. Hence, a bilinear interpolation approach is used to determine $(\Phi_{H,k}, \Phi_{V,k})$ from the phase values captured by the camera at the pixels that surround the pixel $(u_{P,k}, v_{P,k})$ where the k-th calibration marking was detected. The bilinear interpolation can be expressed as:

$$\Phi_{H,k}(u_{C,k}, v_{C,k}) = a_0 + a_1 u_{C,k} + a_2 v_{C,k} + a_3 u_{C,k} v_{C,k}, \tag{33}$$

$$\Phi_{V,k}(u_{C,k}, v_{C,k}) = b_0 + b_1 u_{C,k} + b_2 v_{C,k} + b_3 u_{C,k} v_{C,k}, \tag{34}$$

where a_i and b_i, $i = 0, \ldots 3$, are the interpolation coefficients, found from the solution to the following systems of equations:

$$\begin{bmatrix} 1 & u_{C,i} & v_{C,j} & u_{C,i}v_{C,j} \\ 1 & u_{C,i} & v_{C,j+1} & u_{C,i}v_{C,j+1} \\ 1 & u_{C,i+1} & v_{C,j} & u_{C,i+1}v_{C,j} \\ 1 & u_{C,i+1} & v_{C,j+1} & u_{C,i+1}v_{C,j+1} \end{bmatrix} \begin{bmatrix} a_0 \\ a_1 \\ a_2 \\ a_3 \end{bmatrix} = \begin{bmatrix} \Phi_{H,(i,j)} \\ \Phi_{H,(i,j+1)} \\ \Phi_{H,(i+1,j)} \\ \Phi_{H,(i+1,j+1)} \end{bmatrix}, \tag{35}$$

$$\begin{bmatrix} 1 & u_{C,i} & v_{C,j} & u_{C,i}v_{C,j} \\ 1 & u_{C,i} & v_{C,j+1} & u_{C,i}v_{C,j+1} \\ 1 & u_{C,i+1} & v_{C,j} & u_{C,i+1}v_{C,j} \\ 1 & u_{C,i+1} & v_{C,j+1} & u_{C,i+1}v_{C,j+1} \end{bmatrix} \begin{bmatrix} b_0 \\ b_1 \\ b_2 \\ b_3 \end{bmatrix} = \begin{bmatrix} \Phi_{V,(i,j)} \\ \Phi_{V,(i,j+1)} \\ \Phi_{V,(i+1,j)} \\ \Phi_{V,(i+1,j+1)} \end{bmatrix}, \tag{36}$$

In Eqs. (35) and (36), $u_{C,i} = \lfloor u_{C,k} \rfloor$, $u_{C,i+1} = \lceil u_{C,k} \rceil$, $v_{C,j} = \lfloor v_{C,k} \rfloor$, $v_{C,j+1} = \lceil v_{C,k} \rceil$ are the image coordinates of the pixels that surround the detected calibration marking $(u_{C,k}, v_{C,k})$. Once the absolute phase values $(\Phi_{H,k}, \Phi_{V,k})$ of the markers are known, the corresponding image coordinates in the projector panel $(u_{P,k}, v_{P,k})$ can be determined uniquely by linear interpolation. Given the horizontal and vertical resolution of the projector panel, DMD_H and DMD_V, respectively, the projector coordinates of the calibration markers are

$$u_{P,k} = DMD_H\left(\frac{\Phi_{H,k}-\Phi_{H,min}}{\Phi_{H,max}-\Phi_{H,min}}\right) + 1, \quad (37)$$

$$v_{P,k} = DMD_V\left(\frac{\Phi_{V,k}-\Phi_{V,min}}{\Phi_{V,max}-\Phi_{V,min}}\right) + 1, \quad (38)$$

where $\Phi_{H,max}, \Phi_{H,min}, \Phi_{V,max}, \Phi_{V,min}$ are the maximum and minimum of the encoded absolute phase values in the projector, in the horizontal and vertical directions, respectively.

This final result of this step of the calibration procedure is the complete calibration data set, which consists of the world coordinates ($X_{W,k}$, $Y_{W,k}$, $Z_{W,k}$) of each calibration marking k, and its corresponding image coordinates in the camera $(u_{C,k}, v_{C,k})$ and projector, $(u_{P,k}, v_{P,k})$.

5.4.5 Model Fitting and Selection

The mathematical model for the computation of the 3D surface profile from the camera and projector pixel coordinates of a point on the object surface is referred to here as the calibration model. In this thesis, in contrast to LUT approaches that fit regression models to each pixel data (Section 2.4.2), a single calibration model is used for all camera pixels to predict each 3D world coordinate of each point in the object surface as a function of its camera and projector pixel coordinates, namely:

$$X_W = f_X(u_c, v_c, u_p, v_p), \quad (39)$$

$$Y_W = f_Y(u_c, v_c, u_p, v_p), \quad (40)$$

$$Z_W = f_Z(u_c, v_c, u_p, v_p), \quad (41)$$

where u_c, v_c and u_p, v_p are, the camera and projector image coordinates of the point on the object surface, respectively. X_W, Y_W, and Z_W are its coordinates in the world reference frame, and f_k, $k = X, Y, Z,$ are regression functions with coefficients determined based on the calibration data set generated in the previous steps. By using a single model for each world coordinate that is fitted to

data from all pixels, the proposed calibration approach is able to capture the global trends and non-linear interactions between input variables, which may arise due to image distortions and optical aberrations. More importantly, using all pixel data to fit a single model for each world coordinate allows for a larger data set, which leads to more robust estimates for the calibration parameters and narrower confidence intervals for the model predictions, in contrast with LUT approaches.

Based on previous work [55] that has used polynomial functions to establish phase-to-height relationships, in this work polynomial regression functions are considered as candidates for f_k, Table 1. The choice of considering only polynomial regression functions of up to the third degree is based on the statistical principle of parsimony [84], and is further verified in this work through analysis of regression residuals and model selection metrics, discussed later in this section.

Table 1. Polynomial regression models considered.

Model	**Number of Model Parameters**	**Mathematical Equation**
Linear	4	$f_k(u_c, v_c, u_p) = \beta_0 + \beta_1 u_c + \beta_2 v_c + \beta_3 u_p$
Linear with Interactions	7	$f_k(u_c, v_c, u_p) = \beta_0 + \beta_1 u_c + \beta_2 v_c + \beta_3 u_p + \beta_4 u_c v_c + \beta_5 v_c u_p + \beta_6 u_c u_p$
Quadratic	10	$f_k(u_c, v_c, u_p) = \beta_0 + \beta_1 u_c + \beta_2 v_c + \beta_3 u_p + \beta_4 u_c v_c + \beta_5 v_c u_p + \beta_6 u_c u_p + \beta_7 {u_c}^2 + \beta_8 {v_c}^2 + \beta_9 {u_p}^2$
Cubic	20	$f_k(u_c, v_c, u_p) = \beta_0 + \beta_1 u_c + \beta_2 v_c + \beta_3 u_p + \beta_4 u_c v_c + \beta_5 v_c u_p + \beta_6 u_c u_p + \beta_7 {u_c}^2 + \beta_8 {v_c}^2 + \beta_9 {u_p}^2 + +\beta_{10} u_c^2 v_c + \beta_{11} u_c v_c^2 + \beta_{12} v_c^2 u_p + \beta_{13} v_c u_p^2 + \beta_{14} u_c^2 u_p + \beta_{15} u_c \mathrm{u_p^2} + \beta_{16} u_c \mathrm{v_c u_p} + \beta_{17} {u_c}^3 + \beta_{18} {v_c}^3 + \beta_{19} {u_p}^3$

Once the functional form of a parametric regression model has been specified (e.g., as in Table 1), model fitting refers to the process of estimating the optimal set of coefficients β_j based on a set of calibration data. Since the models listed in Table 1 are linear on the regression coefficients, the theory of linear regression can be easily applied to fit the models to the calibration data. It is known, however, that linear regression coefficients are highly sensitive to noisy and/or outlier-ridden data. Given that the proposed SL system for micro-scale measurements can be affected by multiple sources of noise (vibrations, ambient illumination, object albedo), robust regression methods are recommended to obtain estimates of the regression coefficients that are less sensitive to outliers.

Namely, the Iteratively Re-weighted Least Squares (IRLS) method [85], a robust regression method, is used to determine robust coefficients for the calibration models. In the following lines, the standard notation found in the regression literature [85] is used to briefly describe IRLS regression.

In the IRLS algorithm, at iteration q, a weighted linear least squares problem is solved,

$$\beta^{(q+1)} = \arg\min_{\beta} \sum_i w_i^{(q)} \left| \boldsymbol{y}_i - \boldsymbol{X}_i \beta^{(q)} \right|^2 = \left(\boldsymbol{X}^T \boldsymbol{W}^{(q)} \boldsymbol{X} \right)^{-1} \boldsymbol{X}^T \boldsymbol{W}^{(q)} \boldsymbol{Y}, \tag{42}$$

where $\boldsymbol{W}^{(q)}$ is a diagonal matrix of weights that controls the influence of each observation, $\boldsymbol{Y}$ is the vector of observed responses, and $\boldsymbol{X}$ is the design matrix of the regression, with each column representing a regression variable and each row an observation. In the context of fitting calibration models for the SL system, the observed responses $\boldsymbol{Y}$ are the world coordinates (X_W, Y_W, Z_W) of the calibration markers while the design matrix of the regression $\boldsymbol{X}$ would contain as columns the individual terms of the polynomial regression models listed in Table 1, e.g., $(1, u_c, v_c, u_p, u_c^2, v_c^2, u_p^2, \dots)$. Initially, the weights are set all equal to 1, $w_i^{(0)} = 1$, $i = 1, \dots n$, and are updated at each iteration q as a function of the magnitude of the residual between each observation and the corresponding regression model prediction. A commonly used choice of weighting function is the Cauchy weighting function, also used in this work without loss of generality,

$$w_i^{(q+1)} = \frac{1}{1 + \left(\boldsymbol{y}_i - \boldsymbol{X}_i \beta^{(t)} \right)^2}. \tag{43}$$

Other weighting functions can be used [86]. However, initial tests performed in this work (not shown here) did not find significant differences between results obtained with different weighted functions. Overall, the effect of the IRLS method is, as iterations proceed, to give progressively smaller weights to the observations that deviate the most from the regression model, thus making the process robust to outliers.

To evaluate the performance of each calibration model with the calibration data set, the root mean squared (RMS) error and the median absolute deviation (MAD) were used, calculated as:

$$RMS = \sqrt{\frac{1}{n}\sum_{i=1}^{n}(\hat{\boldsymbol{y}}_i - \boldsymbol{y}_i)^2}, \tag{44}$$

$$MAD = median\{|\hat{\boldsymbol{y}}_i - \boldsymbol{y}_i|, i = 1, \dots, n\}, \tag{45}$$

where $n < n_{calib}$ is the number of observations used to calculate the error metric, $\hat{\boldsymbol{y}}_i$ is the prediction of the calibration model, and $\boldsymbol{y}_i$ is the observed data. RMS is used herein as the error metric of choice in standard regression analysis, while MAD is used as the preferred error metric in robust regression as it is less influenced than RMS by the large residuals that occur at any observation that is considered an outlier.

Once all the calibration models are fitted to the calibration data, the model selection metrics below are used to select the best model for that particular data set [84]. In this context, the best model is defined as that which fits the data well without overfitting, thus exhibiting better generalization capabilities [84]. In particular, in this work the residual mean squared error is used, calculated as:

$$MS_{res}(p) = \frac{SSE_{res}(p)}{n-p}, \tag{46}$$

and the leave-one-out cross-validation error is also used, calculated as:

$$CV = \sqrt{\frac{1}{n}PRESS}, \tag{47}$$

where n is the number of observations, p is the number of model coefficients (a measure of "complexity" of the model), $SSE_{res}(p) = \sum_{i=1}^{n}(\hat{\boldsymbol{y}}_i - \boldsymbol{y}_i)^2$ is the sum of squared errors for a regression model with p parameters, $PRESS = \sum_{i=1}^{n}(\hat{\boldsymbol{y}}_{-i} - \boldsymbol{y}_i)^2$, is the prediction sum of squares for leave-one-out cross-validation, and $\hat{\boldsymbol{y}}_{-i}$ is the value of the i-th observation predicted by a model fitted to a data set from which this observation has been removed.

To prepare for fitting the calibration models and selecting the model with the lowest predictive error for the calibration data, the calibration data set is split into two subsets following best practices for data analysis [87]. One data set, named the training data set and containing 80% of the observations, is used for fitting the calibration models, i.e., to determine the model coefficients. The second set, named the validation data set and containing the remaining 20% of the data, is used after the model is fitted to assess its predictive abilities.

The IRLS method described above is used on the training data to fit the regression models listed in Table 1. Then, the error metrics and model selection criteria, Eqs. (46) and (47), are calculated for these models based on the training data sets. In addition, RMS and MAD error metrics are calculated based on the validation data sets. This information is then used to select the best model for the data, and to quantify its predictive accuracy.

The final result of the calibration procedure is a mathematical model that maps the image coordinates of each pixel in the camera frame (u_c, v_c), and its corresponding pixel coordinates in the projector panel (u_p, v_p), to the world coordinates of the corresponding point on the surface of the measured object (X_W, Y_W, Z_W).

5.5 Summary

In this chapter, a novel calibration approach for SL systems for micro-scale measurements has been presented. In the proposed Structured-Light with Image Focus Fusion technique, a focus fusion approach is used to combine images of the measured object illuminated with the fringe patterns at a set of different focus levels, thus increasing the effective depth of field of the microscope lenses used in the camera and projector. In addition, a novel viewpoint re-mapping technique is introduced to determine the image coordinates of the detected calibration markers in the projector panel, necessary to complete the calibration data set. Furthermore, a single, global calibration model, valid for all pixels in the image, is fitted to the calibration data to predict the world coordinates of the object surface, as opposed to typical look-up table approaches that fit one regression model for each image pixel. Finally, a formal approach for fitting, selection and assessment of calibration models is presented, resulting in calibration models that have the lowest predictive errors for a given calibration data set.

Chapter 6
Implementation Experiments on SL System Configuration Design for Macro-Scale Measurements

The design methodology presented in Chapter 3 was applied to a real-time SL system for surface profiling of complex objects. Experiments were conducted with an optimal sensor configuration and the performance of the optimal sensor configuration was compared with a non-optimal hardware configuration.

6.1 Testing the Design Methodology

In this section, the proposed design methodology was utilized to simulate the optimal configurations of an SL system consisting of a CCD camera (Prosilica GE680C) with a 640x480 pixel resolution and a DLP projector (Texas Instrument Inc. DLP Light Commander®) with a 1024x748 native pixel resolution. The projection area used in the simulations was 640x480 pixels. The pixel size of the camera was 7.4 μm, whereas the pixel size for the projector was 10.8 μm. Table 2 presents the hardware specifications for the projector, the camera and their corresponding optics. The user-defined measurement volume is also identified to be 60x70x30 mm^3 in order to contain small complex objects of interest. Based on these specifications, the design constraints are defined to determine the physical feasibility of implementing SL triangulation configurations with the corresponding hardware components for the desired measurement volume.

Table 2. Hardware and user-defined specifications.

	Parameters	**Values**
Focal lengths	f_C, f_P	16 mm, 28 mm
Working distance range for camera's lens	$d_{C,min}, d_{C,max}$	300 mm, 700 mm
Working distance range for projector's lens	$d_{P,min}, d_{P,max}$	575 mm, 1000 mm
Pixel sizes	λ_C, λ_P	7.4 μm, 10.8 μm
Resolution	$N_{h,C}, N_{v,C}, N_{h,P}, N_{v,P}$	$640, 480, 640, 480$
Camera volume	$\mathcal{V}_C$	[50, 40, 70] mm
Projector volume	$\mathcal{V}_P$	[200, 55, 115] mm
Measurement volume	$\mathcal{V}$	[60, 70, 30] mm
Number of axes for pattern encoding	N_a	1

The ranges for the design variables were arbitrarily defined in order to explore a wide variety of triangulation configurations while being consistent with the space limitations of our physical test environment, Table 3. The 3D SL system models described in Section 3.1 were used to estimate

the performance metrics. A flat plane was moved along the z-axis of the world coordinate system at 7.5 mm increments across the measurement volume.

Table 3. Ranges for the design variables used during optimization.

Design Variable		Ranges
Distance to the reference plane	z_{ref}	[250, 1000] mm
Camera-projector distance in x	w	[-500, 0] mm
Camera-projector distance in y	h	[-500, 0] mm
Camera-projector distance in z	l	[0, 500] mm
First projector's Euler angle	α_P	[-90, 0] °
Second projector's Euler angle	β_P	[70] °

Eighteen optimal triangulation configurations were obtained from the design methodology for the specified hardware as shown in Table 4. Each configuration is different from the others by at least one design variable.

Table 4. Optimal configurations obtained by the proposed methodology.

Configuration No.	z_{ref} (mm)	w (mm)	h (mm)	l (mm)	α_p (°)	β_p(°)
1	756.3	-475.0	-100.0	212.5	-18.00	10.88
2	756.3	-412.5	-100.0	275.0	-6.75	14.63
3	756.3	-475.0	-100.0	87.5	-18.00	14.00
4	756.3	-475.0	-100.0	87.5	-18.00	11.50
5	756.3	-412.5	-100.0	337.5	-18.00	10.88
6	756.3	-412.5	-100.0	275.0	-18.00	12.75
7	756.3	-475.0	-287.5	275.0	-18.00	10.88
8	756.3	-475.0	-475.0	87.5	-6.75	13.38
9	756.3	-475.0	-412.5	87.5	-6.75	10.88
10	756.3	-412.5	-412.5	337.5	-18.00	13.38
11	756.3	-350.0	-475.0	337.5	-6.75	10.88
12	756.3	-225.0	-162.5	337.5	-6.75	10.88
13	756.3	-225.0	-100.0	212.5	-6.75	12.13
14	550.0	-175.0	-362.5	450.0	-54.00	12.63
15	756.3	-225.0	-162.5	25.0	-18.00	10.88
16	756.3	-162.5	-162.5	337.5	-6.75	14.00
17	756.3	-100.0	-162.5	337.5	-6.75	11.50
18	756.3	-100.0	-412.5	25.0	-18.00	11.50

The performance metric results for each of these configurations are presented in Table 5. All eighteen optimal configurations can be implemented using the aforementioned SL system hardware. In the next section, experiments conducted are presented for Configuration No. 5, chosen among these optimal triangulation configurations because it presents a reasonable trade-off between the optimization objectives shown in Table 5.

Table 5. Performance metrics for the optimal configurations obtained by the proposed methodology.

Configuration No.	μ_{RMS} (mm)	σ_{RMS} (mm)	η	N_s	d_{N_s} (mm)
1	0.3295	0.0647	0.158	443	5.52
2	0.3366	0.0669	0.162	388	5.57
3	0.3430	0.0660	0.155	295	6.68
4	0.3432	0.0677	0.158	314	6.63
5	0.3519	0.0781	0.158	826	4.23
6	0.3612	0.0774	0.156	646	4.82
7	0.3640	0.0673	0.158	509	5.25
8	0.3860	0.0718	0.163	129	8.43
9	0.3870	0.0707	0.166	139	8.18
10	0.4319	0.0829	0.156	584	5.07
11	0.4422	0.0795	0.166	314	6.60
12	0.5107	0.1072	0.166	908	4.08
13	0.5515	0.1205	0.164	527	5.25
14	0.5634	0.1605	0.098	30	9.71
15	0.6553	0.1647	0.158	321	6.77
16	0.7253	0.1673	0.162	995	3.96
17	1.4571	0.3878	0.165	1037	3.87
18	1.5306	0.4023	0.158	238	7.46

6.2 Experimental verification

In this section, experiments conducted with an optimal configuration (Configuration No. 5 from Table 4) of the real-time SL system presented in Section 6.1 are evaluated to verify its performance with respect to a feasible configuration (z_{ref} = 810.99 mm, w = -413.97 mm, h = -162.56 mm, l=159.65 mm, α_p= -25.58°, β_p = 10.89°), generated randomly in the design space but satisfying the design constraints provided by the proposed design methodology. Furthermore, the performance of the optimally configured SL system is also investigated with respect to obtaining the 3D surface profile of objects with different surface complexities.

6.2.1 System hardware

The SL system utilized in the experiments was implemented using the hardware components specified in Section 6.1. Figure 11 shows the SL hardware system. The DLP projector and the CCD camera were synchronized by a micro-controller for pattern projection and capturing at a frame rate of 200 fps. The hardware components of the SL system were placed according to a triangulation configuration and the overall SL system was calibrated using the procedure presented in [42]. A high-precision linear stage, Aerotech Model ATS212, with a repeatability of $\pm 1\mu$m, was utilized for the calibration of the overall sensory system.

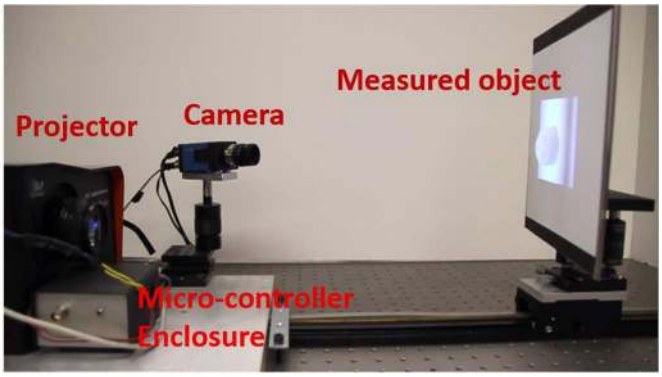

Figure 11. SL hardware system.

6.2.2 Pattern coding strategy

In order to establish the projector-camera correspondence, a continuous time-multiplexing technique with a sinusoidal intensity profile, previously developed by our group [43], was utilized as the pattern coding strategy due to its ability to provide accurate measurements and real-time processing speeds [3]. The technique uses two sets of three $2\pi/3$ phase-shifted patterns. The first set of patterns consists of five vertical fringes, while the second set consists of only one vertical fringe. After correspondence has been established, the 3D reconstruction model presented in Section 3.1.4 is used to obtain the 3D world coordinates of the measured surface points of an object of interest.

6.2.3 Comparison between optimal and feasible triangulation configurations

The experimental comparison was performed by measuring a flat plane and a metric step block, both of which were mounted on a high-precision stage and placed within the measurement volume. For the experimental comparison of the triangulation configurations, only the performance metrics related to the reconstruction errors were used by comparing the measured 3D profile of an object with respect to its known dimensions. The number of 3D points obtained from unique pixel-to-pixel correspondence nor their dispersion within the measurement volume can be physically determined in the SL system set-up. This is due to the fact that these two metrics are primarily based on the 3D points with unique pixel-to-pixel correspondence established during the backward ray-tracing method in the design methodology. In contrast, during the experiments, the unique pixel-to-pixel correspondence cannot be identified since individual light rays cannot be isolated in order to determine whether the majority of the rays corresponding to a particular camera pixel are originating from the same projector pixel.

The plane was placed on the aforementioned high-precision stage and moved along the z-axis of the world coordinate system at 0.1 mm increments, covering a depth of 6 mm at the center of the measurement volume. Figure 12 shows the RMS errors in depth. The optimal SL triangulation configuration provides more accurate measurements (min. RMS error = 0.1869 mm, max. RMS error = 0.1992mm, mean RMS error = 0.1924 mm) than the feasible configuration (min. RMS error = 0.2410 mm, max. RMS error = 0.2985 mm, mean RMS error = 0.2701 mm).

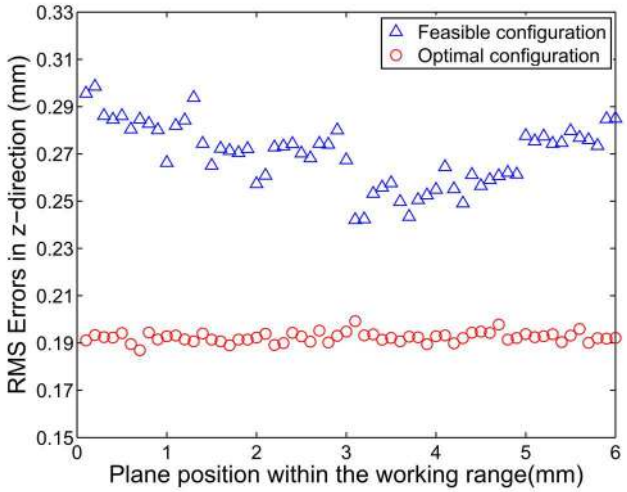

Figure 12. 3D surface reconstruction of the SL system within 6 mm range.

The metric step block with certified dimensions (American Society for Testing and Materials International E797 metric step block) was also measured in order to compare the system performance when measuring an object with known depth variation, Table 6. The step block was placed on the stage and its height dimension was aligned with the z axis of the coordinate frame of the SL system. Namely, the measured height corresponds to the z-coordinate ($Z_{W,i}$) in Eqs. (11) and (12). The mean value of the measured height for each step was estimated by comparing the measurement results with the corresponding certified height. Figure 13 shows the surface profile of the step block obtained from measurements with the optimal triangulation configuration for the SL system. Overall, the comparison results show that the optimal SL system configuration obtained with the proposed methodology outperforms the feasible configuration, thus validating the effectiveness of the methodology as a general design tool for SL systems.

Table 6. Measurement results of a certified metric step block.

Certified height	Optimal configuration	Feasible configuration
1.0 mm	1.024 mm	1.255 mm
2.5 mm	2.513 mm	2.672 mm
5.0 mm	4.918 mm	5.216 mm

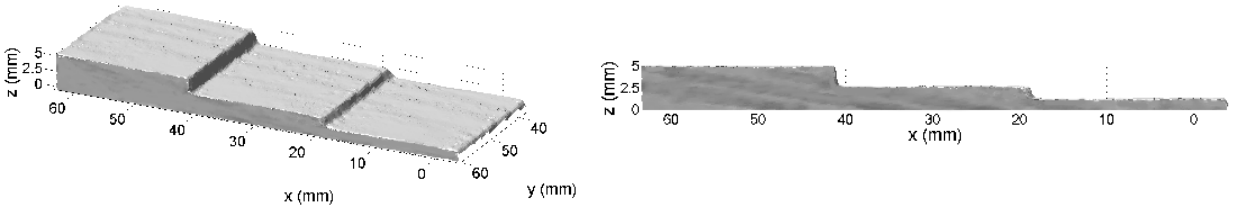

Figure 13. 3D surface reconstruction of metric step block measured with the optimal configuration.

6.2.4 3D reconstruction of complex objects using the optimal SL triangulation configuration

As a further evaluation of the optimally configured SL sensory system, a set of complex objects were measured. The objects chosen were: (a) a LEGO™ part with an array of protruding pins on its surface; (b) a propeller with four slender blades with evenly distributed small holes; and (c) a curved gear with both convex and concave regions and small teeth. The measurement results in Figure 14 show the ability of the designed SL system to obtain the 3D surface profiles of objects with different surface complexities.

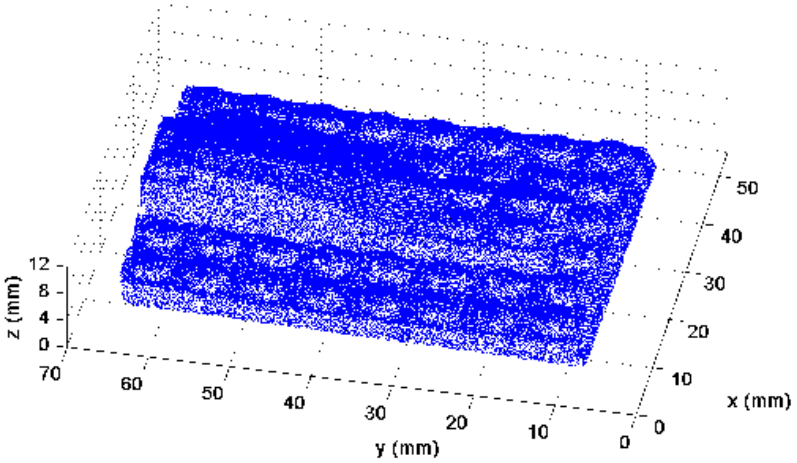

(a)

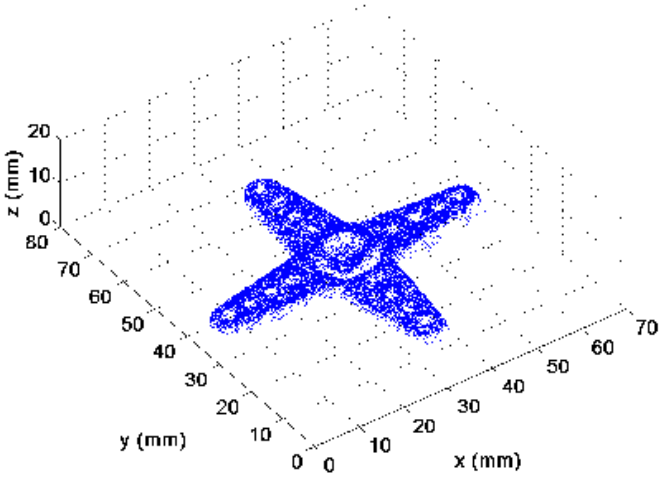

(b)

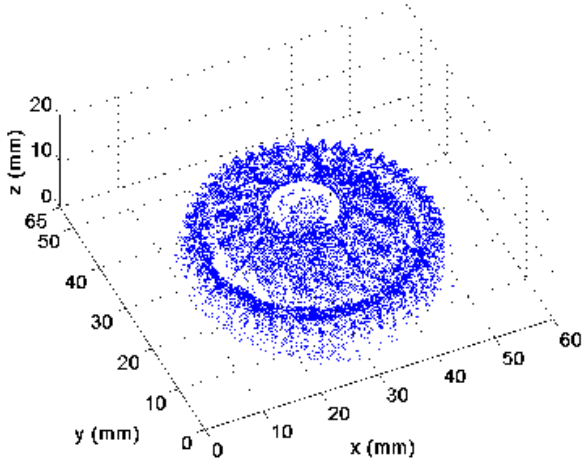

(c)

Figure 14. 3D surface reconstruction of complex objects: (a) LEGO™ piece, (b) propeller, and (c) gear.

6.3 Summary

An SL system configuration was designed utilizing the proposed design methodology for SL system configurations. Experiments were conducted to compare the implementation of an optimal configuration determined by the design methodology with respect to a feasible configuration also provided by the methodology. Experimental results showed that the optimal configuration provided more accurate 3D surface profiles than the feasible configuration. The optimally configured SL system was also used to show the capability of the designed SL system in obtaining the 3D surface profiles of objects with different surface complexities. Due to its generality, the proposed methodology can be used to design optimal SL system for any given set of hardware components to measure objects with varying surface complexities.

Chapter 7
Implementation Experiments on Pattern Sequence Design for SL Systems for Macro-Scale Measurements

The proposed pattern sequence design methodology presented in Chapter 4 is implemented on an SL system and its performance is compared extensively in experiments to a commonly used approach for obtaining fringe pattern sets using a variety of test objects.

7.1 Pattern Sequence Methodology applied to an SL Sensory System

The proposed methodology was implemented in order to determine the optimal sequence of multi-fringe patterns for an SL sensory system developed following the methodology presented in Chapter 4. The SL sensory system consists of a DLP projector (Optoma ML300) with a native resolution of 1024x748 pixels, a CCD camera (Prosilica GE680C) with a native resolution of 640x480 pixels and a triggering unit consisting of an Arduino micro-controller responsible for synchronizing the projector and camera during pattern projection and image capturing, Figure 15. The hardware triangulation configuration between the projector, camera and an object of interest was determined using the hardware set-up design methodology previously developed in Chapter 3. The system was calibrated using the procedure presented in [42]. The pattern projection area for the overall system is defined to be 400x300 pixels. It is important to note that the methodology is not dependent on any specific hardware components and can be used with other SL hardware systems to meet user needs.

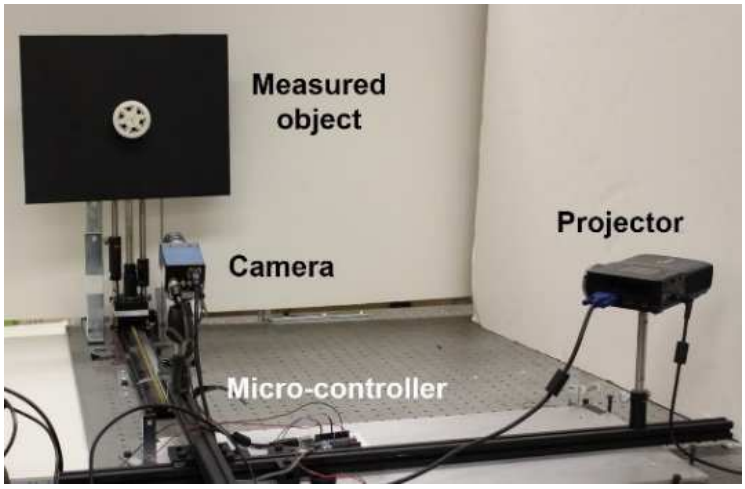

Figure 15. Objects with different surface complexities.

7.1.1 Set of Fringes

Step 1 of the proposed methodology was implemented to determine the set of fringes to be investigated based on the pattern coding resolution of the SL system. The sinusoidal patterns were designed to vary along the higher resolution horizontal axis, with $N = 400$ pixels. Therefore, the set of fringes evaluated were defined as $\mathbb{S}_n = \{n_f\} = \{1, 2, 4, 5, 8, 10, 16, 20, 25, 40, 50, 80\}$ where n_f corresponds to the number of fringes that satisfy the following conditions: 1) $n_f \in \{1, \dots, 400/5\}$, and 2) $400 \; mod \; n_f = 0$.

7.1.2 Random Noise in Relative Phase

Step 2 of the methodology was implemented by projecting a single fringe pattern onto a flat plane placed at the center position within the measurement volume of the SL system. The random noise in relative phase, $\hat{\sigma}_{\phi_{n_f}^c} = 0.036$ rad, was estimated by (7) as the average of the standard deviations of 20 measurements of the phase values for the single fringe $\hat{\sigma}_{\phi_1^c}$.

7.1.3 Set of Patterns

Step 3 of the methodology was used to determine the optimum set of multi-fringe patterns among the set of existing fringes determined in Step 1. To define the range for the noise level of the phase values for the simulations, a value of $\eta = 2$ was considered, i.e., the noise level was set to be within $0 < \sigma_{\phi_{n_f}^c} < 0.072$ rad. In order to characterize the random variable $\sigma_{\Phi_{n_f}^c}$, the absolute phase $\widetilde{\Phi}_{n_f}^c$ was simulated $N_{reps} = 20$ times for each random noise value defined by incrementing through the aforementioned range by 0.001.

In order to identify the set of patterns required to achieve the minimum noise in the absolute phase for the SL system, Eq. (31) was used. The number of unwrapping steps was determined to be two using the random noise reduction criterion in Step 3. The results are presented in Figure 16, where the random noise in the resulting absolute phase $\sigma_{\Phi_{n_f}^c}$ is presented as a function of the number of fringes n_f, the random noise level of the relative phase $\sigma_{\phi_{n_f}^c}$ and the reference phase $\sigma_{\Phi_{ref}^c}$. Namely, Figure 16(a) and Figure 16(b) present the results for the first and the second phase unwrapping steps where the random noise in the resulting absolute phase $\sigma_{\Phi_{n_f}^c}$ is presented in logarithmic scale as a function of the number of fringes n_f, the random noise level of the relative

phase $\sigma_{\phi_{n_f}^c}$ and the reference phase $\sigma_{\Phi_{ref}^c}$. It can be seen that when larger numbers of fringes are present in the pattern, lower random noise levels are obtained in the absolute phase. Namely, with larger number of fringes (lighter shades in Figure 16) there is an order-of-magnitude noise reduction in the logarithmic-scale axis of $\sigma_{\Phi_{n_f}^c}$ in both Figure 16(a) and Figure 16(b). The optimization process resulted in $n_{f,step1} = 10$ and $n_{f,step2} = 50$, from Figure 16(a) and Figure 16(b) respectively. Hence, for our SL sensory system, the robust set of patterns corresponds to patterns with {1, 10, 50} fringes. The notation {1, $n_{f,step1}$, $n_{f,step2}$,….} from hereon is used to represent a set of fringe patterns for sequential phase unwrapping.

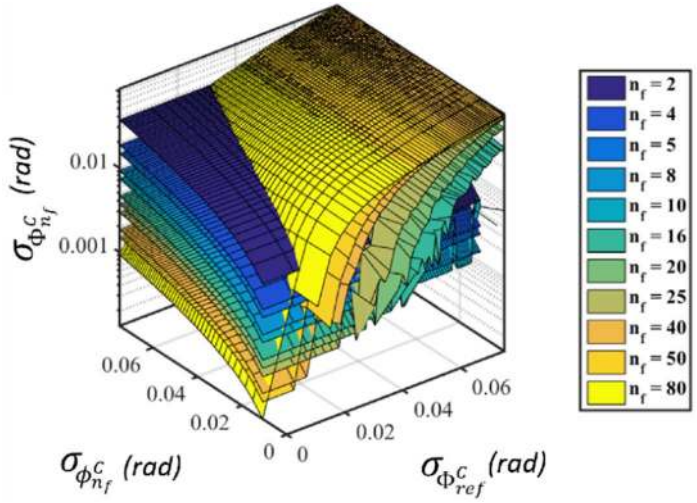

(a)

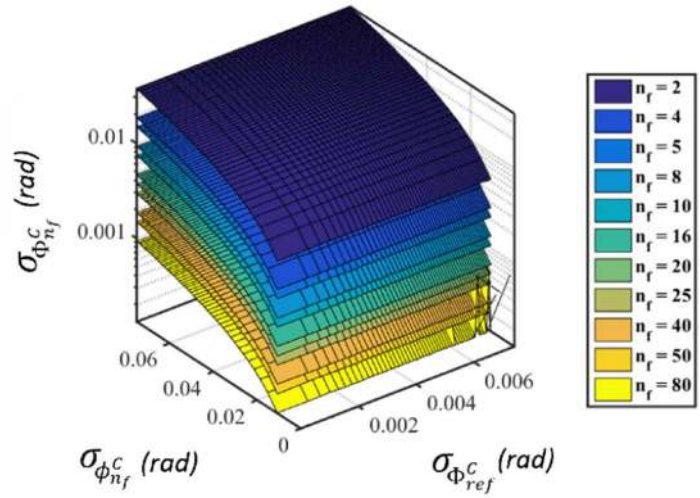

(b)

Figure 16. Effect of random noise in relative and reference absolute phases on the absolute phase for varying random noise levels during (a) the first and (b) the second unwrapping steps.

7.2 Experiments

Experiments were conducted utilizing the proposed pattern sequence methodology for various objects. The pattern set obtained using our methodology was compared with two multi-fringe pattern sets obtained using a commonly used approach presented in [49] which gradually increases the number of fringes of a multi-fringe pattern in order to reduce the noise in phase. As noted above, this is the only other existing approach that provides a procedure for increasing the number of fringes in a multi-fringe pattern sequence. Namely, the approach requires that the number of fringes in each unwrapping step be doubled for the next consecutive unwrapping step. Using this approach, the following pattern sets were chosen: 1) {1, 2, 4}, as it consists of the same number of unwrapping steps as our methodology defines; and 2) {1, 2, 4, 8, 16}, as it provides a sequence of patterns that reaches the largest number of fringes that can be obtained within the set $\mathbb{S}_n$.

The experimental comparison of these pattern sets was performed for a variety of objects with varying surface complexities. The objects include a metric step block and three 3D printed objects with more complex surfaces including a three-blade propeller, a double-helical gear, and a scaled model of a V6 engine block, as shown in Figure 17. These objects contain a combination of smooth and discontinuous features allowing us to investigate the robustness of the fringe patterns to varying object surface profiles. The performance metrics used for the comparison study were: 1) measurement accuracy, and 2) standard deviation in measurements.

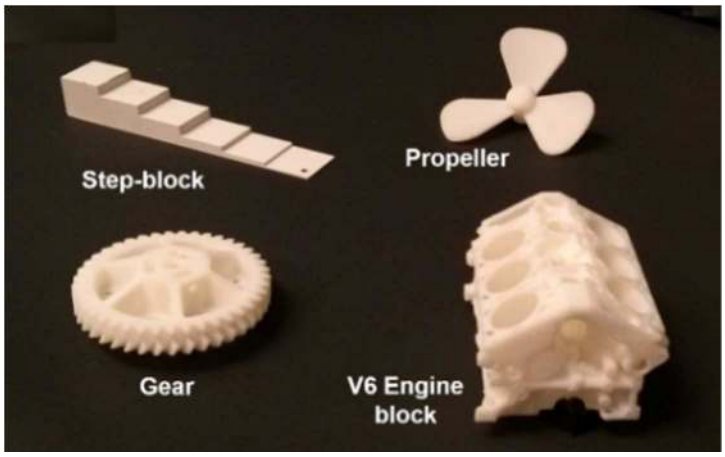

Figure 17. Objects with different surface complexities.

7.2.1 Measurement Accuracy

In order to compare the measurement accuracy for the three pattern sets, a metric step block with ASTM E797 certified dimensions was measured. The random noise in 3D measurement for the

step block was experimentally determined by obtaining the mean value of each measured step height with respect to the corresponding certified height. The step block was measured fifteen times with each pattern set. The mean height measurements for each step of the certified step block were then compared, Table 7. From the table, it can be seen that when using the same number of unwrapping steps, set {1, 10, 50} obtained from our methodology resulted in smaller measurement errors for the height measurements when compared with set {1, 2, 4}. Namely, with the same number of unwrapping steps, the set {1, 10, 50} was able to reduce the random noise in the absolute phase which resulted in more accurate measurements for the heights of each step. With respect to the set {1, 2, 4, 8, 16}, the methodology set {1, 10, 50} provided similar mean values for the height measurement, however, with the proposed methodology, the SL system was able to provide these measurements with half as many unwrapping steps.

Table 7. Measured Heights of a Certified Metric Step Block.

Certified step height (mm)	Methodology set {1, 10, 50}	Set {1, 2, 4}	Set {1, 2, 4, 8, 16}
2.50	2.460	2.560	2.409
5.00	4.889	4.627	4.885
10.00	9.922	9.658	9.908
15.00	14.892	14.724	14.887
20.00	19.850	19.347	19.850

7.2.2 Standard Deviation in Measurements

In order to determine the effect of the random noise in absolute phase $\sigma_{\Phi_{n_f}^c}$ on the random noise in measured height for the metric step block, the standard deviation of the measured heights for each pattern set was determined. As can be seen in Figure 18, a significantly lower standard deviation of the measured height is obtained with methodology set {1, 10, 50} as indicated in Table 8 by non-overlapping 95% confidence intervals around the median standard deviation of the measured heights.

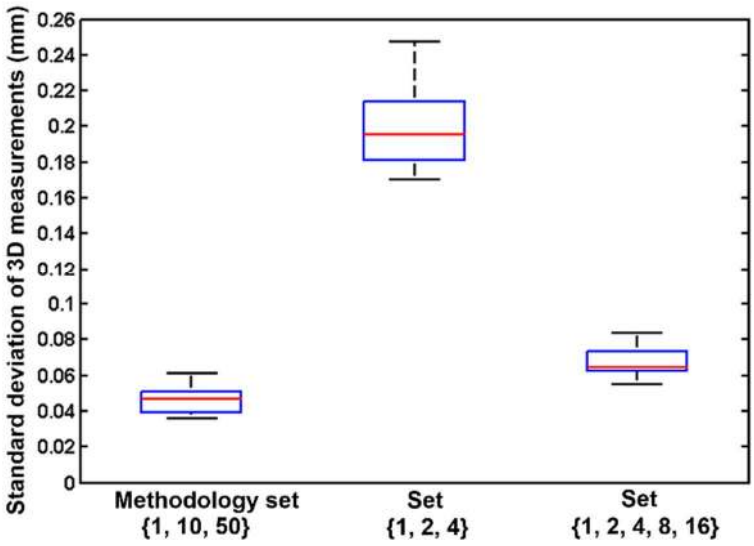

Figure 18. Distribution of the standard deviation of the measured height for the step block.

Table 8. Median and 95% Confidence Interval [in brackets] for the Standard Deviation of the measured Heights.

Measured object (mm)	Methodology set {1, 10, 50}	Set {1, 2, 4}	Set {1, 2, 4, 8, 16}
Step block	46.86 μm [44.70, 49.02]	195.54 μm [189.63, 201.44]	64.42 μm [62.41, 66.42]

7.2.2.1. Complex Surface Profiles

To compare the random noise in 3D measurements of the complex objects, the standard deviation of the world coordinates of each 3D point was determined for the propeller, gear and V6 engine block. The measurements were again repeated fifteen times. Figure 19, Figure 20 and Figure 21 show a comparison of the distributions of the standard deviations for the propeller, gear and engine block, respectively. As can be seen in the figures, the proposed methodology set exhibits smaller standard deviations for the 3D measurements. Table 9 shows the median standard deviation and 95% confidence intervals for each object and pattern set, showing that the standard deviation of the 3D measurements for the methodology set is statistically smaller. Figure 22 shows the 3D point clouds obtained using each pattern set for all three objects, respectively, with the color of each measured 3D point corresponding to its standard deviation. Comparing the point clouds, it can be observed that the feature points throughout each object have smaller standard deviations when using the methodology set. For example, there are, in general, more dark blue points for the

methodology set than the other two sets, noticeably at: 1) the curved blade surfaces in Figure 22(a), 2) the gear teeth in Figure 22(b), and 3) the edges of the six engine cylinders in Figure 22(c). In summary, Figure 19 - Figure 22 show that the proposed methodology approach can reduce random noise in 3D measurements of objects with both smooth and complex surface profiles.

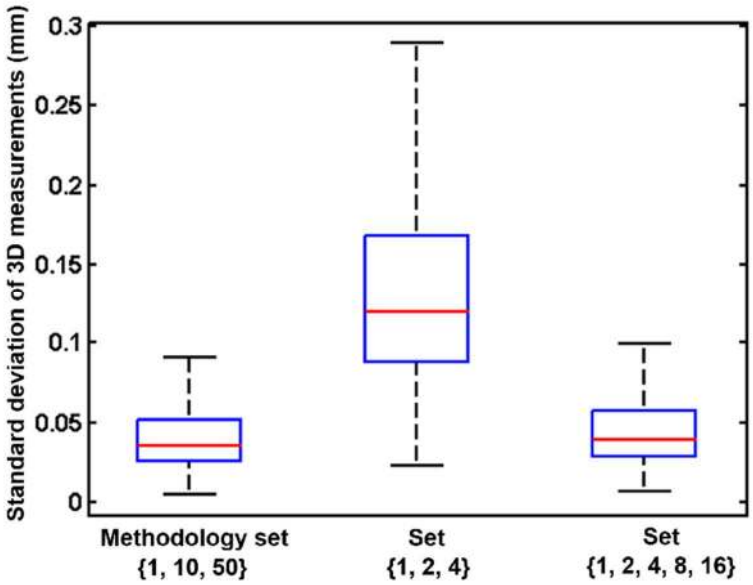

Figure 19. Distribution of the standard deviation of the 3D measurements for the propeller.

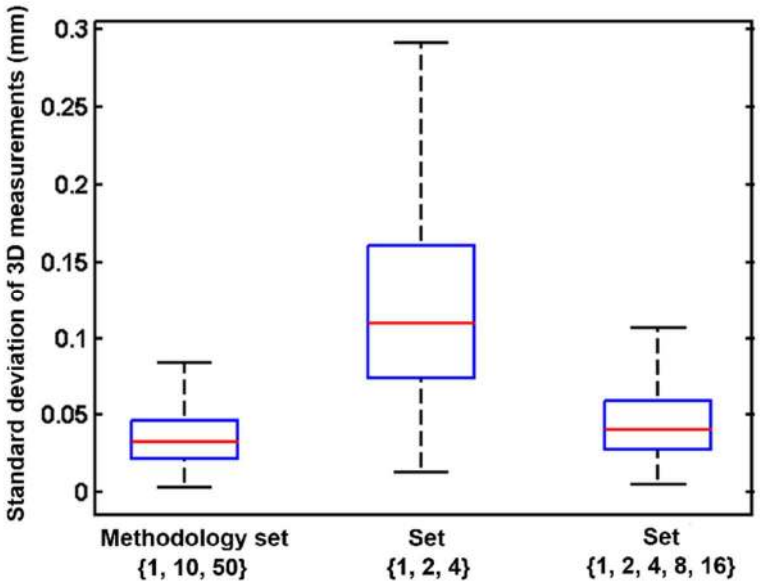

Figure 20. Distribution of the standard deviation of the 3D measurements for the gear.

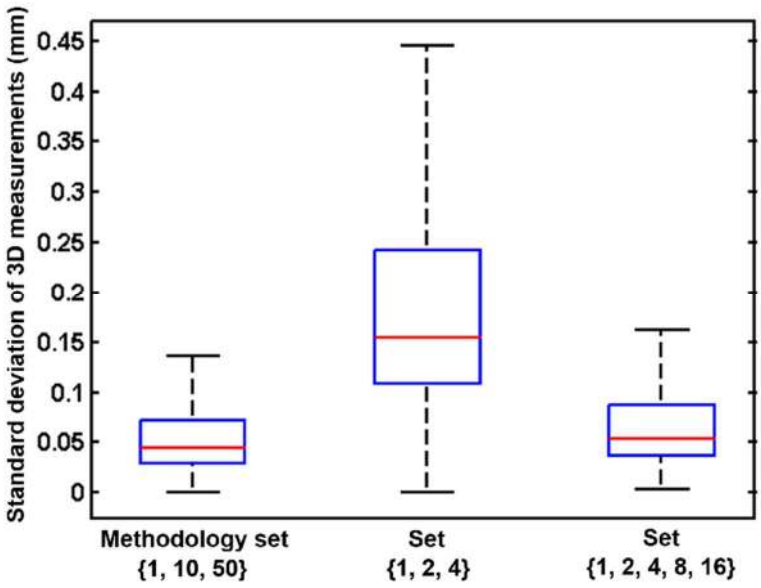

Figure 21. Distribution of the standard deviation of the 3D measurements for the scaled model V6 engine block.

Table 9. Median and 95% Confidence Interval [in brackets] for the Standard Deviation of the 3D Heights.

Measured object (mm)	**Methodology set {1, 10, 50}**	**Set {1, 2, 4}**	**Set {1, 2, 4, 8, 16}**
Propeller	32.25 μm [35.05, 35.45]	119.45 μm [108.87, 120.07]	38.98 μm [38.76, 39.20]
Gear	32.52 μm [32.34, 32.71]	119.45 μm [108.87, 110.12]	40.88 μm [40.65, 41.12]
Scaled Model of V6 Engine block	44.26 μm [43.96, 44.57]	154.86 μm [153.94, 155.58]	54.26 μm [53.91, 54.61]

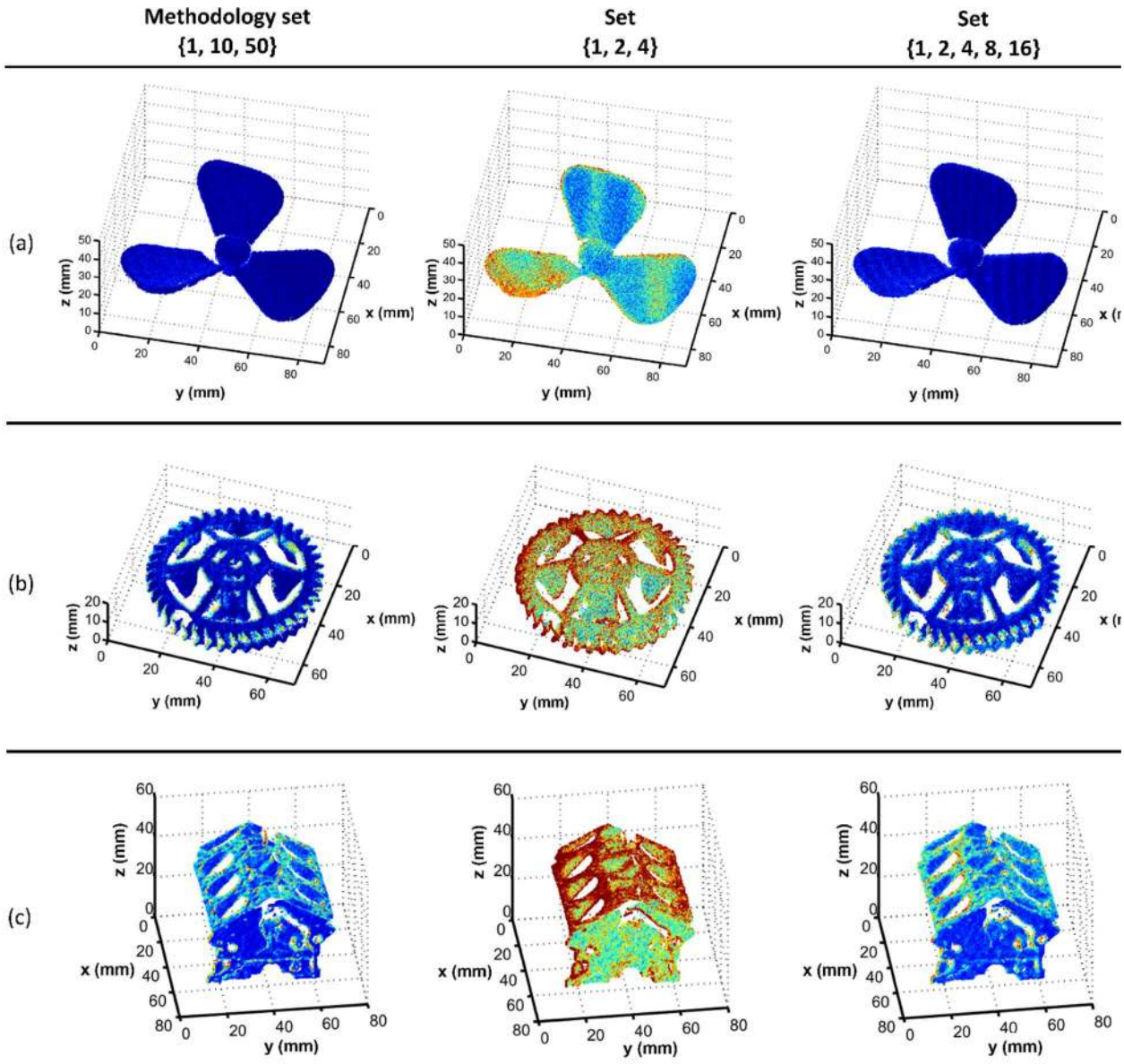

Figure 22. 3D point clouds obtained using different multi-fringe pattern sets for: (a) a propeller, (b) a gear and, (c) a scaled model V6 engine block. The color scale on the right corresponds to the standard deviation in mm of the coordinates of each 3D point.

Since active phase unwrapping allows for 3D reconstruction of each pixel independently of its neighbors (as explained in Section 4.1.2), the computation time required to obtain the 3D reconstruction, t_{3D}, based on the absolute phase of a multi-fringe pattern is directly proportional to the computation time of processing the phase of a given pixel ($t_{\phi_{pixel}}$) and its corresponding 3D coordinates ($t_{3D_{pixel}}$), the number of captured pixels (M x N pixels) and, the unwrapping steps (n_{steps}) in sequential unwrapping, i.e., $t_{3D} = t_{\phi_{pixel}} t_{3D_{pixel}} M N n_{steps}$. In this context, the proposed methodology is efficient in that it minimizes the noise in 3D measurements by using only

the optimal number of unwrapping steps and fringes. The set {1, 2, 4, 8, 16} when compared to the methodology set {1, 10, 50} requires two additional unwrapping steps and also doubles the computation time needed to produce a 3D measurement. In general, the methodology set can be used for a wide range of objects which exhibit smooth varying surface regions, as well as with large numbers of discontinuous and complex features, examples of which are shown herein in the experiments. Furthermore, because the methodology set requires the least number of captured images to obtain accurate 3D reconstruction of an object, it is suitable for real-time and fast-measurement applications as well as measuring dynamic objects when implemented using high throughput hardware components such as those in [13, 88].

7.3 Summary

The proposed pattern sequence design methodology was utilized to determine the optimal pattern sequence for an SL system. Comparison experiments presented verified that the multi-fringe pattern set determined by our proposed methodology is able to minimize random noise in measurements when compared with multi-fringe pattern sets obtained from a frequently used approach.

Chapter 8
Implementation Experiments on Design Methodologies for Micro-Scale Measurements

In this chapter, the proposed design methodologies presented in Chapters 3, 4 and 6 are applied to the design of a 3D SL system for micro-scale measurements. This chapter discusses how the design methodologies were applied to determine the optimal configuration of the hardware components and the optimal pattern sequence to reduce the 3D reconstruction errors. The measurement volume for the SL system developed was defined to be 0.5x0.5x0.5 mm^3. The SL system was calibrated with a measurement accuracy of 1 μm, following the calibration procedure presented in Section 5.4 using the optimal system configuration and the optimal pattern sequence. Experiments were conducted to evaluate the achievement of the desired measurement accuracy and the ability of the designed SL system of measuring a variety of micro-scale objects. Experimental results demonstrate the effectiveness of the proposed methodologies for designing SL systems for micro-scale measurements.

8.1 Design of the SL System Configuration

8.1.1 Description of the Hardware Components

The SL system for micro-scale measurements was developed and implemented in [80] by a member of our research group following the design methodology presented in this thesis and discussed in Section 5.2. The details of the hardware selection and system implementation can be found in [80]. In this section a brief description of the hardware components is provided.

The 3D SL system for micro-scale measurements consists of a DLP projector for projecting the fringe patterns onto the measured object, a CMOS camera for capturing the deformed patterns, and their corresponding microscope lenses, as shown in Figure 23. A micro-controller is used to synchronize the projection and capturing of the fringe patterns of the measured object mounted on a precision stage. The complete SL system, shown in Figure 23, was mounted on a passively damped optical table to minimize the effect of vibration on the experimental results. In the following paragraphs, a description of the hardware components is presented.

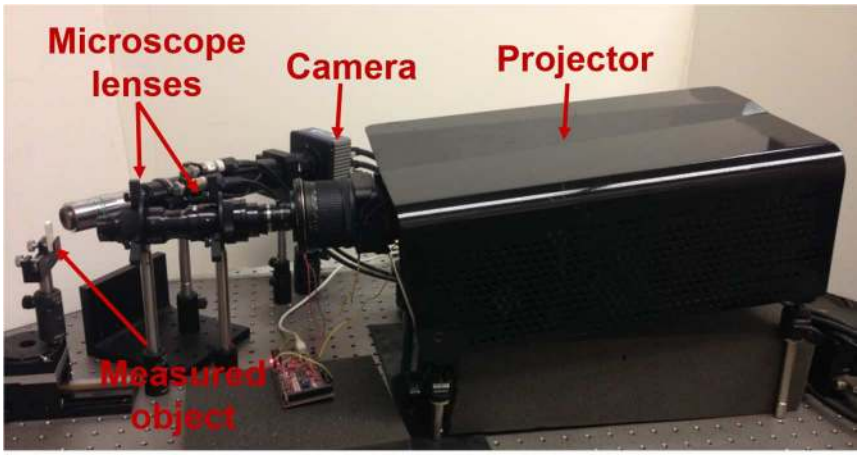

Figure 23. 3D SL sensory system for micro-scale measurements.

The projector is the TI (Texas Instruments Inc.) Light Commander® with a native resolution of 1024 x 768 pixels and a square pixel size of 10.8 μm, which generates 8-bit gray scale (0-255 gray level) light patterns. In order to scale down the light fringe pattern generated by the 0.55" XGA DMD projector panel onto the object size, an assembly of microscope lenses from Navitar Inc. were mounted onto the projector to achieve a magnification level of 16.6X. In order to compensate for an offset vertical angle of 7° on the projection of the Light Commander®, a tilt-shift lens (Nikon 45 mm f/2.8D tilt-shift lens) was incorporated to successfully cancel out the vertical tiling angle of the projection path. In addition, the tilt-shift lens was coupled to a reversed larger aperture Fujinon CCTV lens (Fujinon 25 mm f/1.4) to eliminate the diffraction and neutralize the magnification before further coupling it to the microscope lens (Navitar Zoom 6000). In order to compensate for the Scheimpflug effect, the back support of the projector was lifted up by 8 cm until the effect was minimized in the images through empirical experiments [80]. The list of the microscope lens assembly for the projection side is presented in Table 10.

The camera was the Adimec Quartz Q-4A180/CL with a native resolution of 2048x2048 pixels and a square pixel size of 5.5 μm. The camera can capture images at a maximum frame rate of 180 fps. The assembly of microscope lenses attached to the camera and consists of: a 20X Mitutoyo infinity-corrected long working distance microscope objective lens, a 6.5 X motorized UltraZoom microscope lens (1-62316), a 1.0 X tube lens (1-6015), and a lens motor controller. The microscope lens assembly has a magnification range of 2.8X-18X at a long microscope working distance of 20 mm when coupled to the camera. Table 10 presents the list of the optical components in the microscope lens assemblies for the camera.

Table 10. Assemblies of the microscope lens setup for the projector and the camera [80].

Optics components	
Projector	**Camera**
Nikon 45 mm f/2.8D tilt-shift lens Fujinon CCTV lens (Fujinon 8 mm f/1.4) (reverse lens) 20X Mitutoyo objective lens 6.5 X Zoom microscope lens 2.0 X adapter	20X Mitutoyo objective lens 6.5 X motorized UltraZoom microscope lens 1.0 X tube lens

8.1.2 SL System Configuration

As discussed in Chapter 3, the triangulation configuration between the camera, projector and the measured part has a significant influence on the resulting measurement accuracy, though in practice considerations such as physical interference, working distances of the lenses, FOV and DOF, impose a set of geometrical constraints that significantly limit design choices. For instance, Figure 24 shows the projector and camera lenses in close proximity to the measured object, with the world coordinate system shown for reference purposes. The small working distances of the camera and projector lenses, combined with their size, make it difficult to jointly focus on the target object without obstructing each other's line of sight.

The methodology of Section 5.2 was applied, which relies on the geometric constraint models described in Section 3.2.2. The optimization objective of maximizing the size of the measurement volume was achieved by minimizing the angle between the optical axes of the camera and projector while avoiding physical interference.

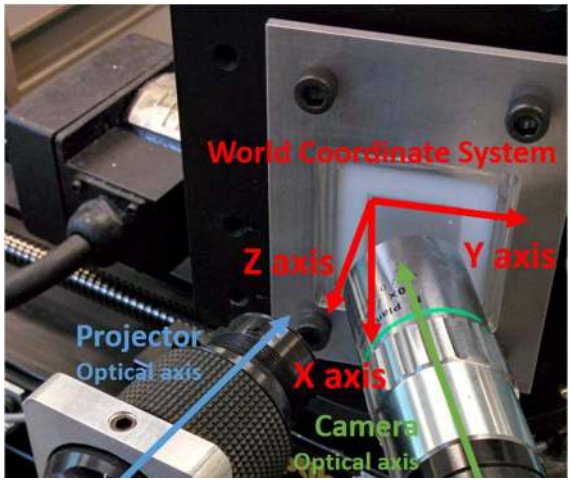

Figure 24. World coordinate frame indicated on the SL system set-up.

8.2 Design of the SL Pattern Sequence

The design methodology presented in Section 5.3 was used to determine the optimal pattern sequence for the SL system for micro-scale measurements, i.e., the sequence of fringe patterns that minimizes the 3D reconstruction errors for a given set of hardware components and their triangulation configuration.

8.2.1 Set of Fringes

Step 1 of the proposed methodology was applied to determine the set of fringes $\mathbb{S}_n$ to analyze based on the pattern coding resolution of the SL system. Since the resolution of the projector is 1024 pixels (in the horizontal direction used for pattern encoding), and ensuring that each fringe is represented by at least 5 pixels, the set of fringes is given by $\mathbb{S}_n = \{n_f\} = \{1, 2, 4, 8, 16, 32, 64, 128\}$, where n_f corresponds to the number of fringes that satisfy these two conditions: 1) $n_f \, \epsilon \, \{1, \dots, 1024/5\}$, and 2) $1024 \; mod \; n_f = 0$.

8.2.2 Random Noise in Relative Phase

Step 2 of the methodology was used to determine the noise in phase values as described in Section 5.3. In particular, the noise in phase values was determined by projecting fringe patterns with all the number of fringes included in the set $\mathbb{S}_n$ onto a vertical flat plane placed within the measurement volume of the SL system. The plane was moved to different z-positions within the target measurement volume, to fully characterize the behavior of the phase noise across the measurement volume.

The random noise in phase was estimated by: 1) taking repeated measurements of the flat calibration object for each z-position, 2) calculating the noise as the standard deviation of the phase values at each pixel with respect to the stage known z-position, and 3) taking the noise average of all the pixels for each plane position. Figure 25 shows the average of the phase noise for the number of fringes considered, for different positions of the plane inside the measurement volume in 50 μm increments. The noise in relative phase increased when the flat plane was imaged at the positions $Z_W = \{0, 100, 450, 500\}$ μm, which correspond to the positions that are closest and farthest from the camera and projector. This is evidence that these positions do not fall inside the region where

both the camera and projector are in focus. Hence, the measurement volume in which both the camera and the projector are in focus is limited within $Z_W = 100$ and $Z_W = 400$ μm.

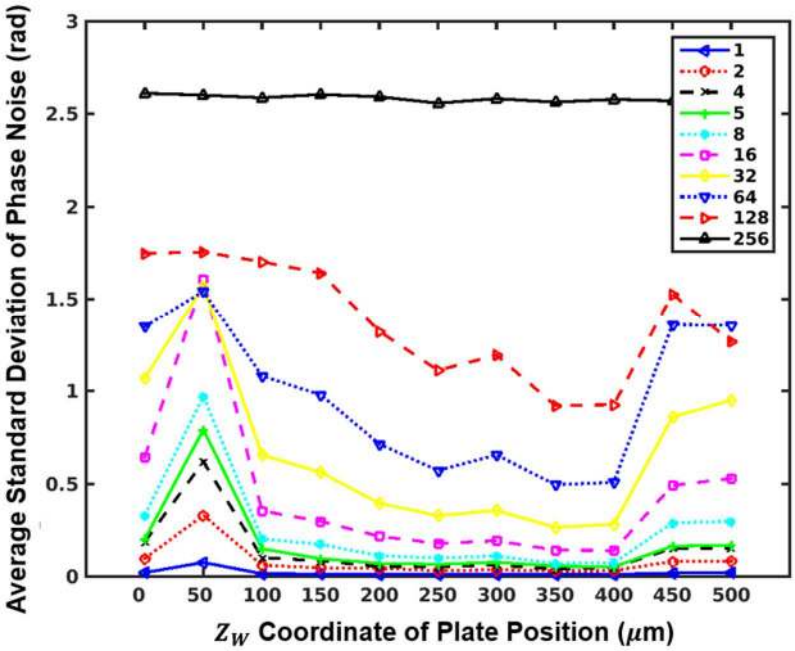

Figure 25. Relative phase noise of fringe patterns projected onto a flat plane moved along the z-axis of the measurement volume for micro-scale measurements.

8.2.3 Pattern Sequence

After the noise in phase values was fully characterized, Step 3 of the methodology was implemented to determine the optimum set of multi-fringe patterns among the set of existing fringes determined in Step 1, using the procedure described in Section 4.2.3. Based on the information provided by Figure 25, a value of 0.25 rad for the noise in relative phase was used, and $\eta = 1.5$ was considered, hence the noise level was set to be within $0 < \sigma_{\phi_{n_f}^c} < 0.375$ rad. The selected noise level of 0.25 rad and safety factor of $\eta = 1.5$ provided an approximate upper bound for the phase noise for patterns with up to 16 fringes. The absolute phase $\widetilde{\Phi}_{n_f}^c$ was simulated $N_{reps} = 20$ times for each random noise value defined by incrementing through the aforementioned range by 0.009 rad.

Eq. (31) was used to identify the optimal set of patterns required to minimize the random noise in the absolute phase for the SL system. Using the random noise reduction criterion in Step 3, described in Section 4.2.3, the number of unwrapping steps was determined to be four, resulting in patterns with {1, 2, 4, 8, 16} fringes. Figure 26(a) and Figure 26(b) present the results for the

first and the last phase unwrapping steps where the random noise in the resulting absolute phase $\sigma_{\Phi_{n_f}^c}$ is presented in logarithmic scale as a function of the number of fringes n_f, and the random noise level of the relative phase $\sigma_{\phi_{n_f}^c}$ and the reference phase $\sigma_{\Phi_{ref}^c}$. Larger number of fringes are represented with lighter shades in Figure 26. For the first unwrapping step, Figure 26(a), it can be seen that $n_{f,step1} = 2$ fringes minimizes the random noise in the absolute phase for the entire domain of $\sigma_{\phi_{n_f}^c}$ and $\sigma_{\Phi_{ref}^c}$. Similarly, after 4 steps of sequential unwrapping, in Figure 26(b), it can be seen that $n_{f,step4} = 16$ fringes provides the minimum random noise in the resulting absolute phase.

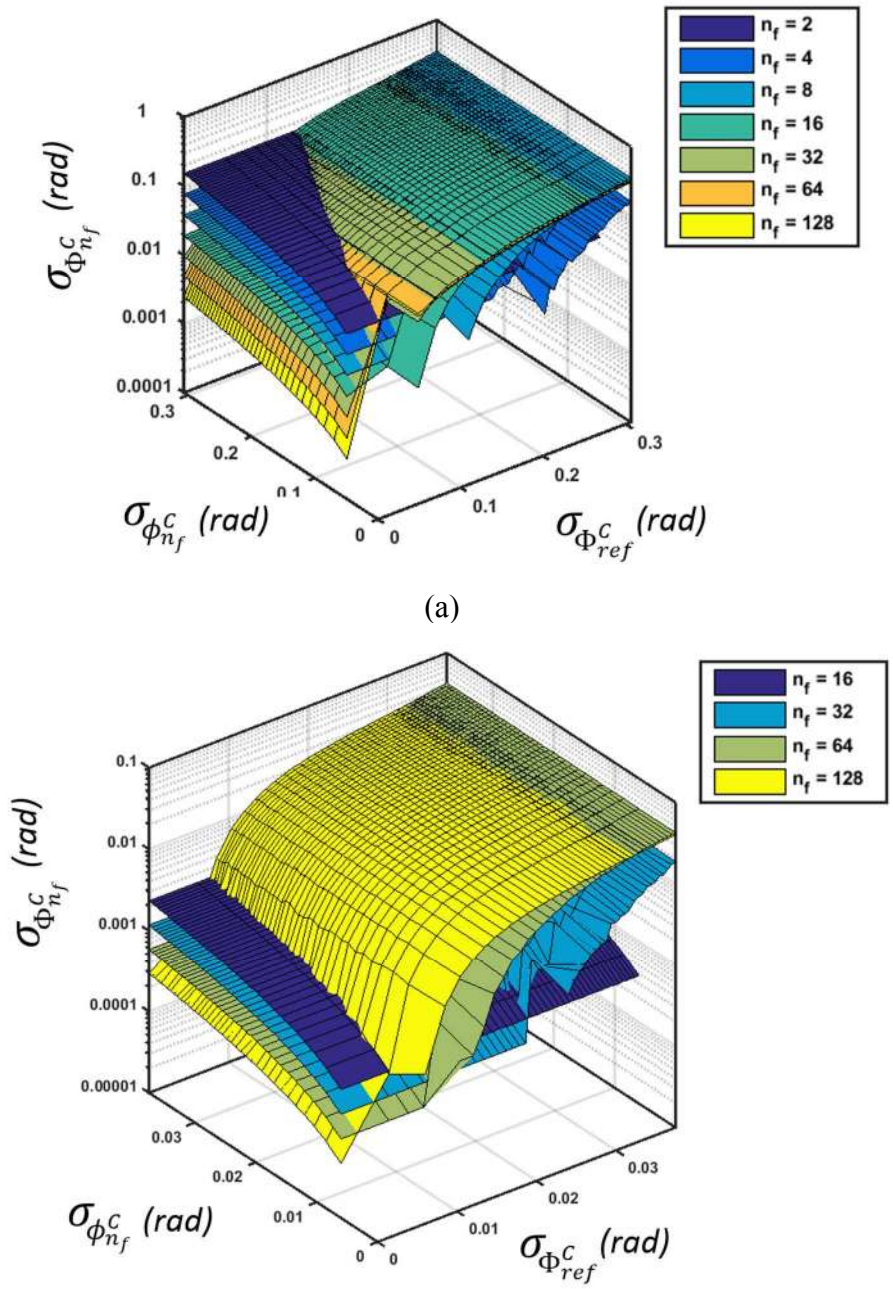

Figure 26. Effect of random noise in relative and reference absolute phases on the absolute phase for varying random noise levels during (a) the first and (b) the fourth (last) unwrapping steps.

8.3 Calibration Procedure

For system calibration, the methodology described in Section 5.4 was used. A planar calibration object featuring a grid of circles with a radius of 62.5 μm and a spacing of 125 μm was used.

Figure 27 and Table 11 provide object specifications. The accuracy of the circle spacing is rated to 1 μm. The calibration object was mounted on top of a 3-axis translational stage (Thor Labs PT3M) in order to move the calibration object through the measurement volume, Figure 28. The position repeatability of the stage is 1.5 μm, with a backlash error up to 8 μm.

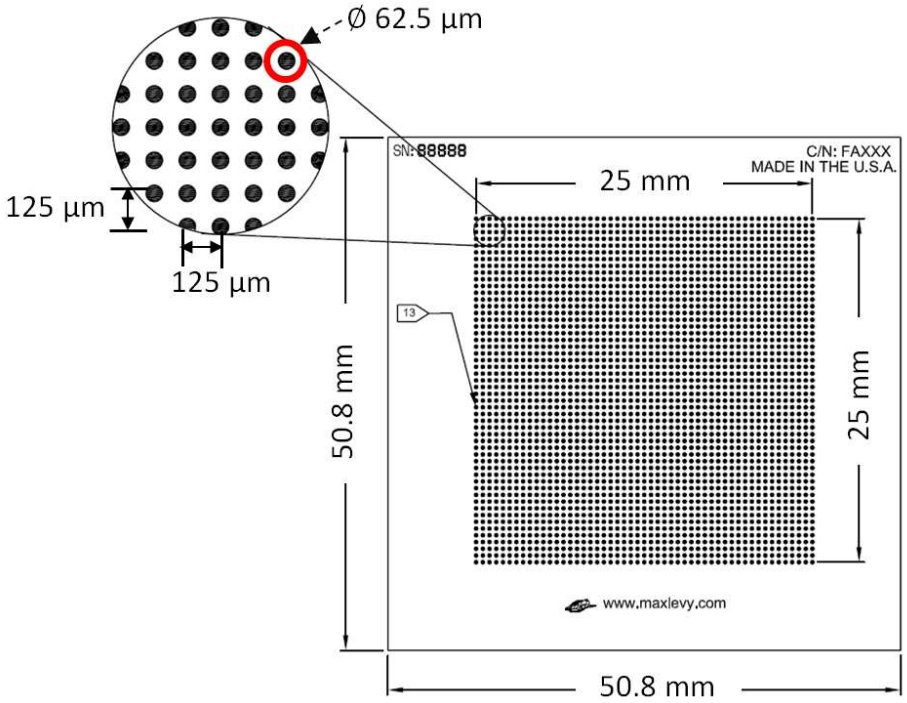

Figure 27. Calibration object featuring a grid of circles from Edmund Optics, Inc. [89].

Table 11. Specification of the calibration object: Fixed frequency grid distortion target from Edmund Optics, Inc. [89].

Specification:	
Type	Chrome on Opal
Dimensions (mm)	50.8 x 50.8
Pattern Size (mm)	25 x 25
Thickness (mm)	1.5
Dot Diameter	62.5 μm
Dot Diameter Tolerance	± 2 μm
Dot spacing	125 μm
Dot Spacing Tolerance (mm)	± 1 μm Center to Center, ± 0.004 Grid Corner to Corner
Overall Accuracy (mm)	± 1 μm
Surface Accuracy (λ)	4 - 6 λ per 25.4 Area
Surface Quality	40-20
Coating	Reflective First Surface Chromium Rabs = 50% ± 5% @ 550 nm

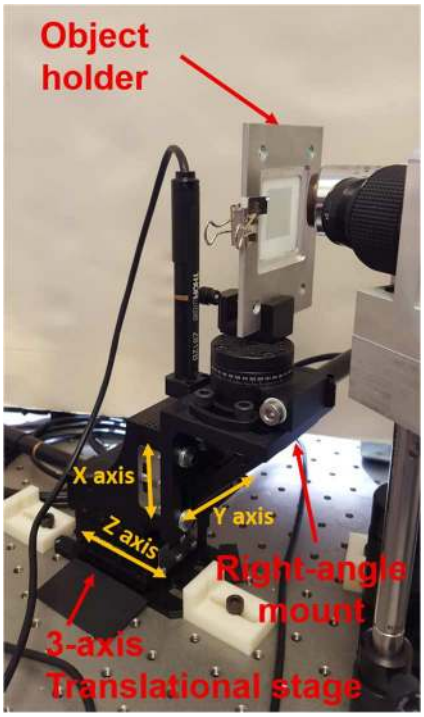

Figure 28. Assembly of a 3-axis translational stage using a right angle bracket to mount the object holder.

The calibration plane was placed vertically on the stage, i.e., with the normal of the plane aligned with the z-axis. The plane was gradually moved with a fixed step along the z-axis, in 50 μm steps, starting from the farthest ($Z_W = 0$ μm) to the closest z-position ($Z_W = 500$ μm) to the sensory system, as indicated in Figure 29. Then, the plane was returned to the position $Z_W = 0$ μm, moved 20 μm in the y-direction, followed by another set of 50 μm movements in the z-direction. This procedure was repeated 6 times, resulting in a total of 66 plane positions.

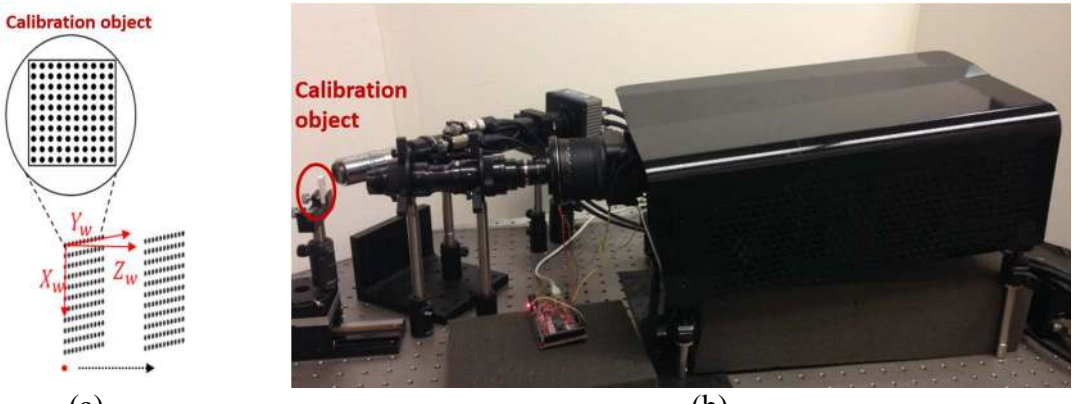

(a) (b)

Figure 29. (a) Schematic of the calibration movement in the world coordinate frame during calibration, (b) SL system set-up with the calibration object indicated.

8.3.1 Multi-focus Imaging of the Calibration Object

For each position of the calibration object, the optimal pattern sequence determined in Section 8.2.3, namely patterns with {1, 2, 4, 8, 16} fringes, were projected. In addition, a fully illuminated pattern was also projected for the focus fusion procedure. For each pattern, images were captured using a procedure for capturing images at multiple focus settings presented in [81]. This procedure consisted of: 1) searching the peak focus of an image to determine the in-focus region, 2) varying the focus level to position the in-focus region at the left of the camera view, and 3) imaging the camera view with images at successive focus levels until the in-focus region was at the right of the camera view. This resulted in a collection of images with a small in-focus region that moved across the camera view.

8.3.2 Focus Fusion

The images captured in the previous step were post-processed to combine information from multiple images captured with different focus levels into a single all-in-focus image for each fringe pattern, for each calibration object location. To this end, the fully illuminated images corresponding to multiple focus levels are processed first, to determine how each region of each image maps out to the final all-in-focus image. Once the mapping between the focused regions of each image and the final all-in-focus image has been determined, this mapping is used for the focus fusion of the remainder pattern images.

8.3.3 Image Feature Detection

The Circular Hough Transform [90], a circle detection algorithm based on the Hough transform, was used to determine the location of the centers of the circular markings in the calibration object [80].

The world coordinates of the circle centers are defined based on the known position of the stage and the known distances between circle centers. This information is then combined with the image coordinates (u_c, v_c) of the circle centers in the camera. Based on the number of plane positions considered (66), and the number of circular calibration markings that are captured in each image, a total of approximately 1,000 data points are used for calibration.

8.3.4 Image Feature Re-Mapping

The last step in acquiring the data needed for system calibration is determining the image coordinates in the projector panel (u_P, v_P) for each of the circle centers that were detected in the camera. This requires determining the pixel-to-pixel correspondences between the camera and the projector. To this end, the all-in-focus images of the optimal pattern set {1, 2, 4, 8, 16} are processed to calculate the relative phase of each pixel, and are then sequentially unwrapped to obtain the absolute phases of each pixel. Finally, the absolute phase values of each pixel are used to calculate the image coordinates of each detected circle center in the projector. This completes the calibration data set, i.e., $(X_{W,k}, Y_{W,k}, Z_{W,k}, u_{C,k}, v_{C,k}, u_{P,k}, v_{P,k})$, for $k = 1, \dots, n_{calib}$.

8.3.5 Model Fitting and Selection

The calibration data set obtained in Section 8.3.4 is used to fit regression models to map the camera and projector image coordinates of points in the object surface to the corresponding world coordinates. For this purpose, the calibration data set is split into two subsets: A training data set, containing 80% of the data and used to determine the coefficients of the model that best fit the data, and a validation data set, containing the remaining 20% of the data and used to assess the predictive performance of the model with a data set that was not used to fit the model.

As discussed in Section 5.4.5, polynomial models of first, second and third degree, shown in Table 1, were considered as candidate models and fitted to the training data set using iteratively re-weighted least squares (IRLS). Then, model selection metrics were computed using the training data to select the single best predictive model for each world coordinate. Figure 30, Figure 31 and Figure 32 show the behavior of error metrics (training RMS, validation RMS) and model selection metrics (residual MSE, cross-validation error) for each model for predicting the X_W, Y_W and Z_W coordinates, respectively. As expected, the RMS error of the model for the training data set decreases as models with more explanatory variables (and more tunable coefficients) are considered. Note, however, that the cross-validation (CV) error increases for the M_4 (i.e., cubic) models, exhibiting its lowest value for the M_3 (i.e., quadratic) models in all three cases. This is evidence that the cubic models are overfitting the data, and are thus unable to predict new observations accurately even though they reproduce the training data closely. Based on this evidence, the quadratic models are selected for the calibration data set. Table 12 shows the

coefficients β_j of the regression models, which are used for determining X_W, Y_W and Z_W based on the image coordinates (u_P, v_P, u_P).

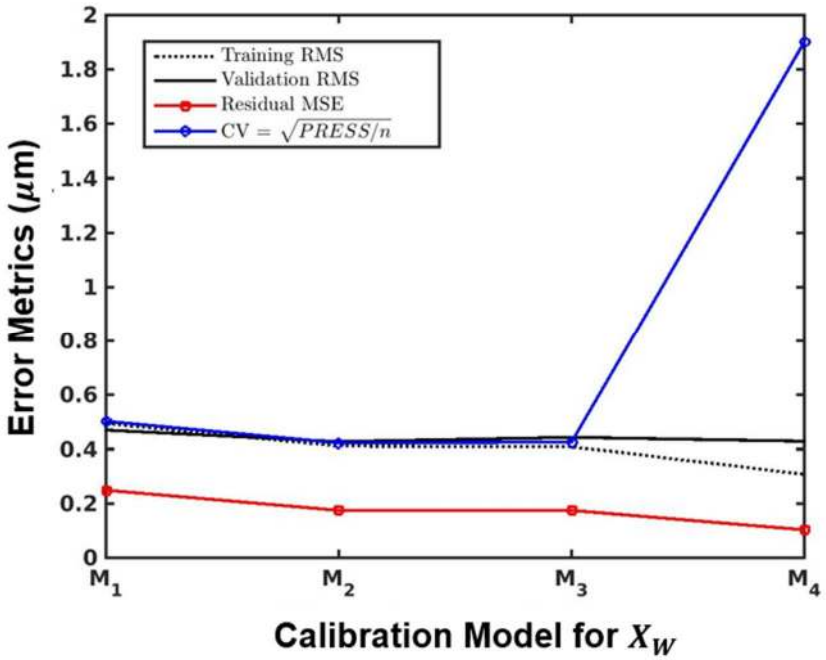

Figure 30. Error metrics and model selection metrics for estimating the x-coordinates using the calibration models: M1: Linear, M2: Linear with interactions, M3: Quadratic, M4: Cubic.

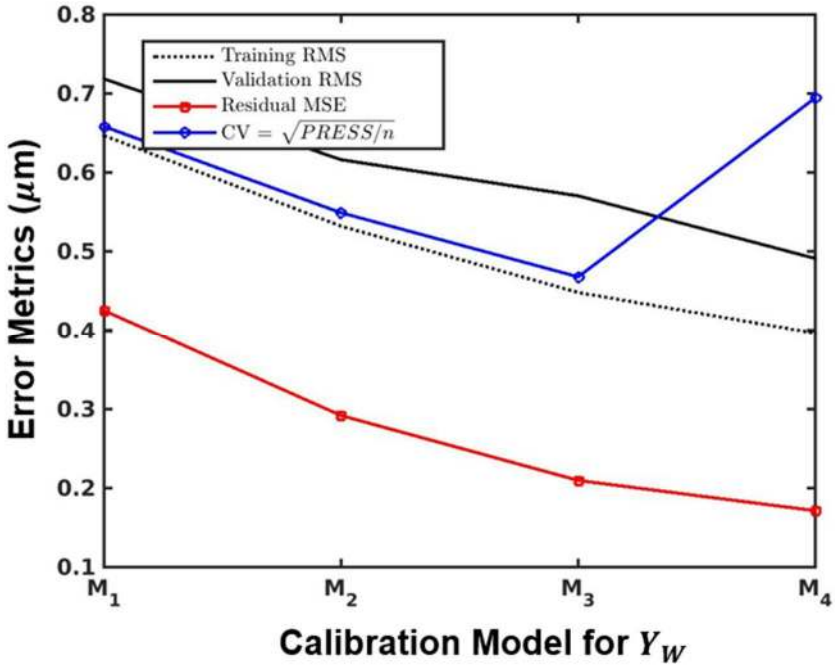

Figure 31. Error metrics and model selection metrics for estimating the *y*-coordinates using the calibration models: M1: Linear, M2: Linear with interactions, M3: Quadratic, M4: Cubic.

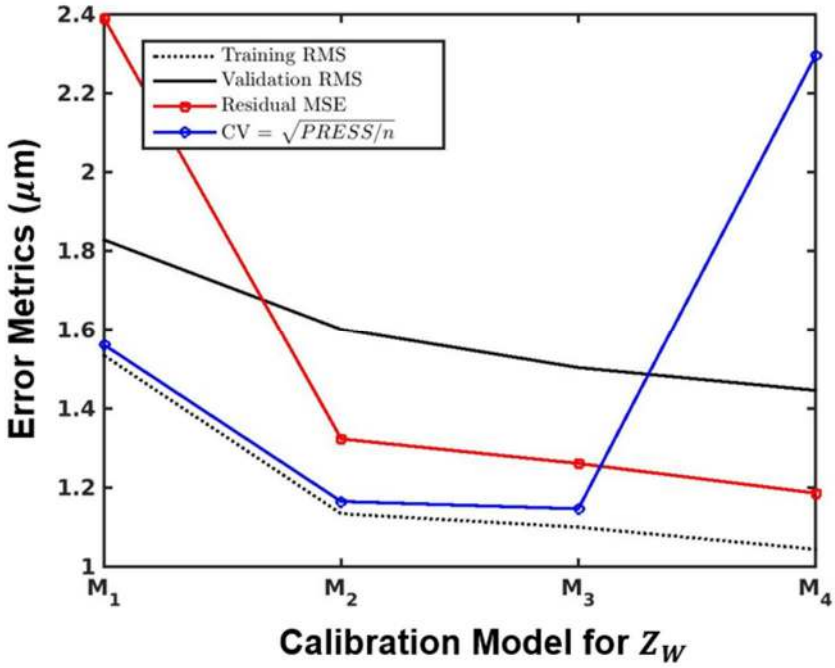

Figure 32. Error metrics and model selection metrics estimating the *z*-coordinates using the calibration models: M1: Linear, M2: Linear with interactions, M3: Quadratic, M4: Cubic.

Table 12. Quadratic regression models fitted to the calibration data set.

Coordinate	Regression Model $\beta_0 + \beta_1 u_c + \beta_2 {u_c}^2 + \beta_3 v_c + \beta_4 u_c v_c + \beta_5 {v_c}^2 + \beta_6 u_p + \beta_7 u_c u_p + \beta_8 v_c u_p + \beta_9 {u_p}^2$
X_W	$\overrightarrow{\beta_X}$ = [-1.1832 , 0.0141 , -0.0267 , 2.4420 , -0.0073 , 0.0002 , -0.1285 , 0.0662 , -0.0054 , -0.0159]
Y_W	$\overrightarrow{\beta_Y}$ = [-1.8035 , 1.9230 , -0.0655 , 0.0133 , 0.0008 , 0.0002 , 1.3125 , 0.1914 , 0.0132 , -0.1170]
Z_W	$\overrightarrow{\beta_Z}$ = [-1.1020 , -8.4957 , 0.2071 , -0.0223 , -0.0105 , -0.0052 , 9.3165 , -0.2730 , 0.0847 , 0.1714]

The models shown in Table 13 only require one of the projector coordinates. In this work, the horizontal image coordinate u_P is used as it is the axis in which the projector has the highest resolution. In Section 3.1.4, it was discussed that the 3D reconstruction only requires one image coordinate of the projector to establish a unique triangulation for a given point on the surface of the measured object, although both projector image coordinates could be used if available to enforce a least squares solution of the triangulation equations. In the context of fitting calibration models for the SL system for micro-scale measurements, tests conducted using both u_P and v_P projector image coordinates to fit the calibration models did not result in lower prediction errors.

Once the model with the lowest cross-validation error was selected for predicting each world coordinate, the models were used to predict the data in the validation set to quantify the predictive accuracy of the models. In particular, the validation data and the model predictions are used to calculate the RMS and MAD error metrics, Eqs. (44) and (45), respectively, which quantify the measurement error that can be expected from the SL system for micro-scale measurements. Table 13 shows the validation error metrics for the calibration models for each world coordinate. It also includes the 3D errors (also known as "isometric" errors), calculated as the L_2 norm of a vector which components are the error metrics for each coordinate. The MAD validation error is 1.36 μm, which is comparable with the position accuracy of the precision stage used for the calibration experiments.

Table 13. Validation error metrics for the quadratic regression models fitted to the calibration data.

Measurement direction	Validation Error (RMS in μm)	Validation Error (MAD in μm)
X_W	0.44	0.34
Y_W	0.57	0.46
Z_W	1.50	1.24
$\sqrt{(X_W)^2 + (Y_W)^2 + (Z_W)^2}$	1.67	1.36

8.4 Experimental Measurements

Once the calibration of the SL system for micro-scale measurements was completed, a series of tests were performed to assess its performance. Both a planar object and complex objects were used for these tests, as discussed below. The performance metrics used were: 1) the measurement accuracy of the system, and 2) surface profile measurements with depth variations and surface discontinuities.

8.4.1 Planar object

A planar object was placed vertically on the stage, i.e., with the normal of the object plane aligned with the z-axis of the SL system. The plane was moved along the z-axis, following the same approach used for the calibration experiments. The plane was moved 10 times in 50 μm steps from $Z_W = 0$ μm to $Z_W = 500$ μm, and moved 3 times in 20 μm steps along the y-direction, for a total of 44 plane positions.

At each position, the planar object was measured using the fringe pattern sequence determined in Section 8.2.3 to generate the absolute phase maps. Then, using the calibration models, the world coordinates of each pixel were calculated, thus generating the point clouds. A mathematical model representing a flat plane was fitted to each point cloud using linear regression methods, and the mean value of the Z_W coordinates of the point clouds was used to indicate the z-position of the plane. This estimated plane position was compared with the actual position of the stage. Figure 33 shows the position errors, i.e., the difference between the z-position of the fitted plane and the (known) position of the stage. The errors are larger when the planar object is placed in the world coordinates $Z_W = \{0, 50, 450, 500\}$ μm, which coincide with the positions where the phase noise errors were larger. However, median position errors for the central region of the measurement volume, i.e., when the planar object was placed in the world coordinates $Z_W = \{150, \dots, 400\}$ μm, are under 2 μm, comparable to the position error of the stage (1.5 μm).

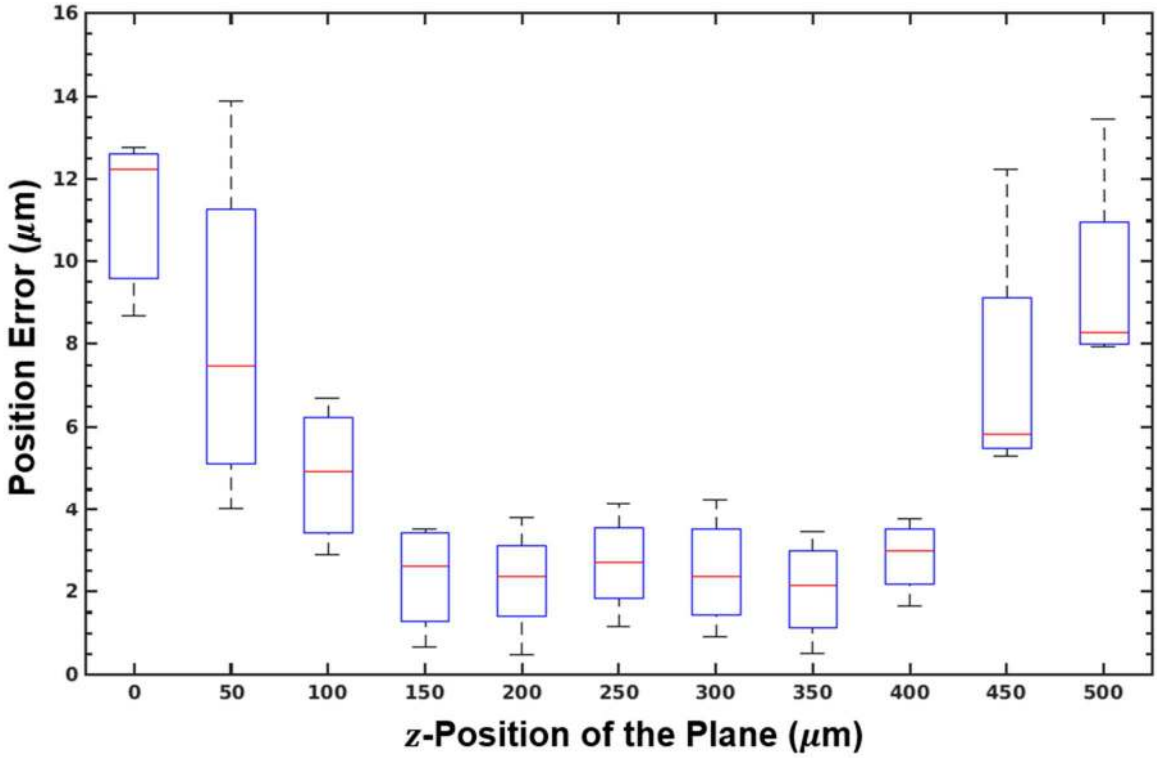

Figure 33. Plane position error with respect to the stage position within the measurement volume.

8.4.2 Complex Objects

Finally, the SL system for micro-scale measurements was tested measuring objects with different surface complexities. The feature of a digit of the year on a Canadian dime (10 cent Canadian coin) was measured, Figure 34. Figure 35 shows the surface profiles of the small regions in which the number "3" and the letter "N" can be seen. Figure 35(a) and Figure 35(b) were rendered from a point cloud with more than 2 million points obtained by registration of 5 and 12, respectively, separate, overlapping measurements conducted while moving the coin in the x-coordinate direction for measuring the number "3" and in both x - and y -coordinates for the letter "N". The surface profiles of the micro-scale features "3" and "N" depicts the ability of the SL system to measure the height variations that characterize the profile of the "3" and the "N", and the surface roughness of the flat area of the coin.

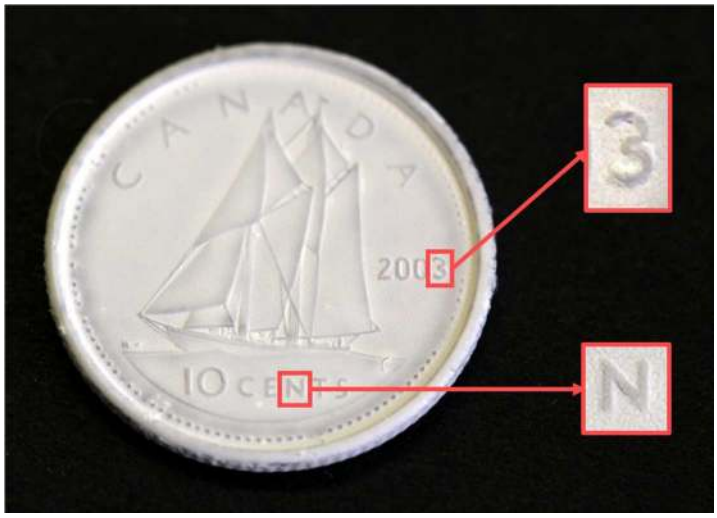

Figure 34. Canadian dime with micro-scale features “3” and “N”.

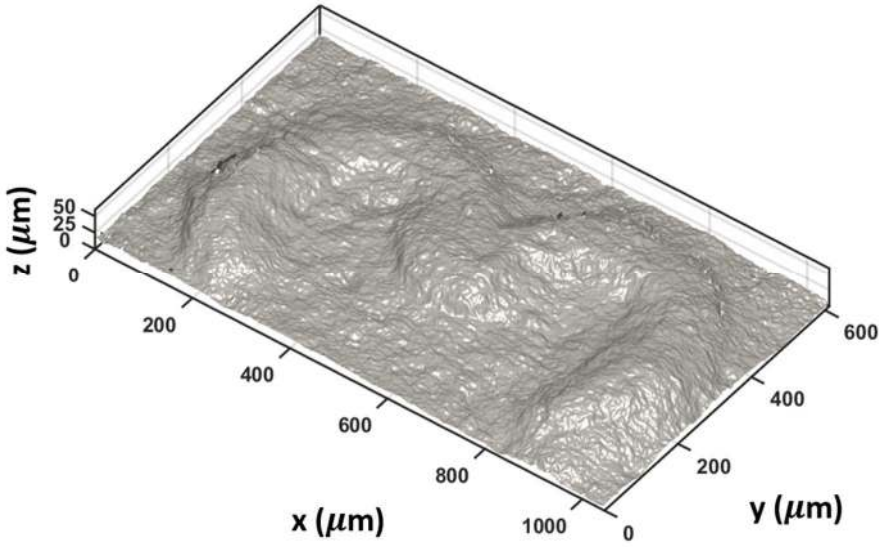

(a)

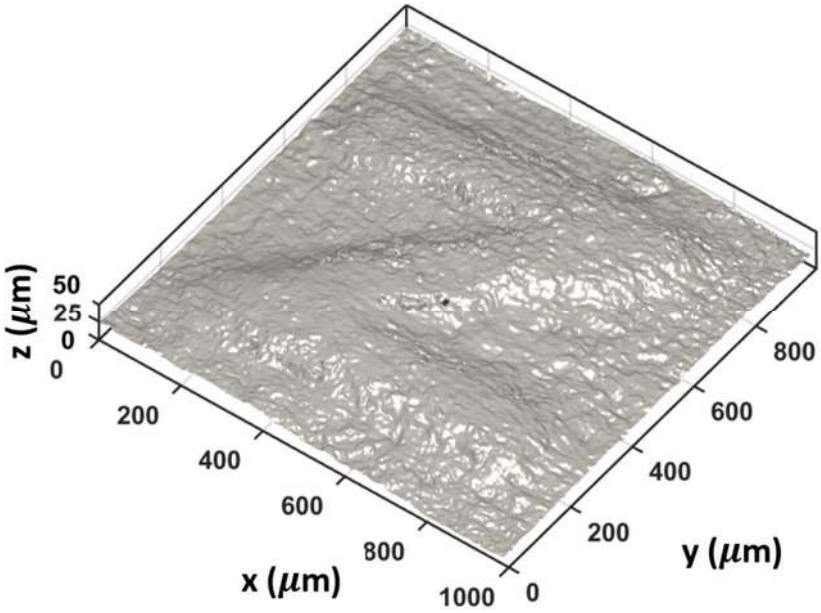

(b)

Figure 35. Surface profile of the micro-scale features "3" and "N" on a Canadian dime measured with the designed SL system.

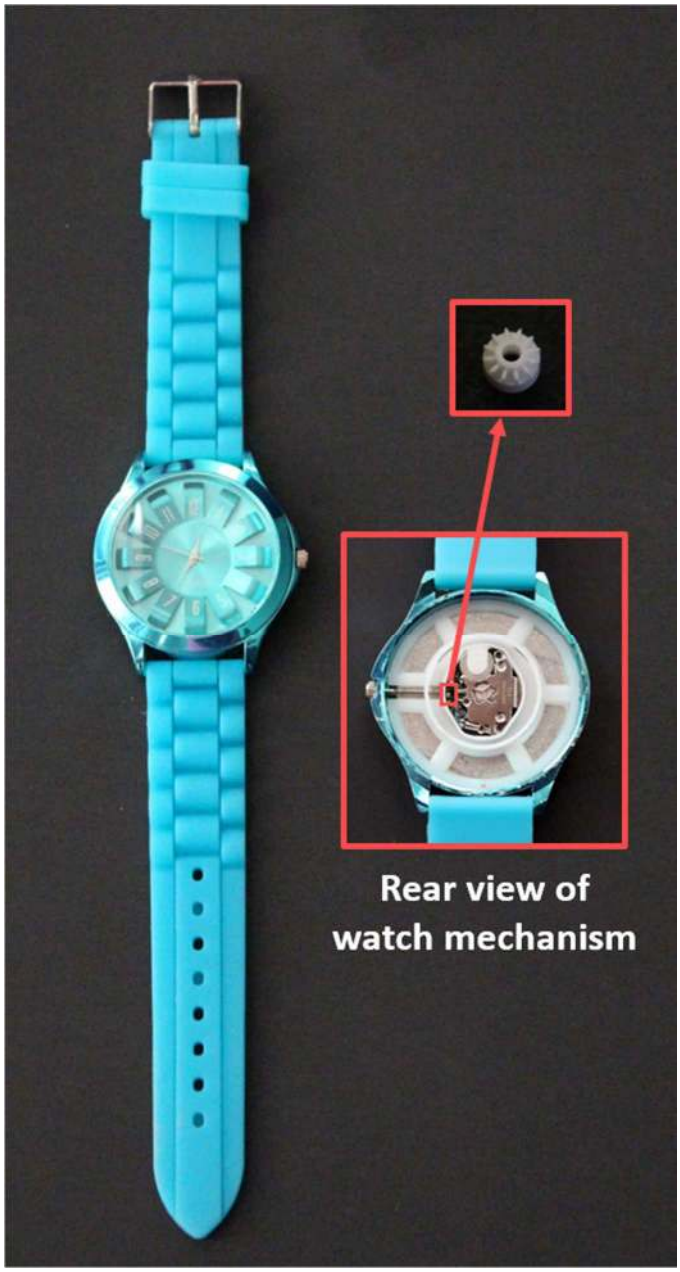

Figure 36. Wrist watch measured with micro-scale gear.

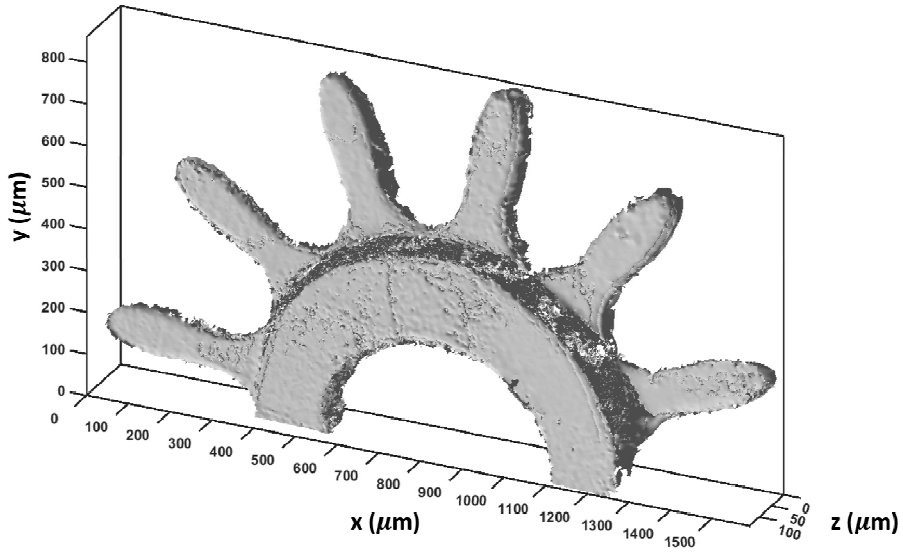

Figure 37. Surface profile of the micro-scale gear of wrist watch measured with the designed SL system.

A micro-scale gear from the mechanism of a wrist watch, Figure 36, was also measured. Figure 37 shows the results of measuring a micro-scale gear from a wrist watch, a small and complex object. This surface profile was rendered from a point cloud with 4.5 million points, obtained by registration of 7 separate, overlapping measurements conducted while moving the gear in both the x-coordinate and y-coordinate directions. The surface profile of the micro-scale gear illustrates that the SL system is able to provide 3D measurements of the discontinuous small teeth, the defined edge profile of the teeth, the curvature of the interior diameter of the hub, and the surface roughness of the gear.

8.5 Summary

In this chapter, the novel design methodologies presented in Chapter 5 were implemented for a 3D SL system for micro-scale measurements of objects. The SL system was implemented using the optimal configuration of the hardware components to maximize the measurement volume, the optimal pattern sequence to reduce the 3D reconstruction errors, and the system calibration for SL systems for micro-scale. Experiments conducted with a variety of micro-scale objects demonstrated the effectiveness of the proposed methodologies for designing SL systems for micro-scale measurements.

Chapter 9
Conclusions

This chapter presents a summary of the research challenges addressed in this thesis, the design methodologies proposed for SL system to measure small complex objects, and validation experiments conducted to verify the effectiveness of the designed systems. Finally, possible directions for future research are discussed.

9.1 Contributions

This thesis presented the design, development and implementation of design methodologies for SL sensory systems in order for them to measure the 3D surface profile of small complex objects. To this end, both hardware and software aspects were considered in the design methodologies for SL systems, resulting in the following contributions to the state of the art:

9.1.1 Design Methodology for SL System Configurations

To design the system configuration of the hardware components of the SL system for measuring small complex objects, a general methodology was developed for determining the optimal triangulation configuration of SL systems. Based on the optical specifications of the camera and projector, their physical sizes, and the target measurement volume, the proposed design methodology determines the optimal configuration of the hardware components based on the following performance metrics: 1) minimizing the 3D reconstruction errors, 2) maximizing the pixel-to-pixel correspondence between the projector and camera, and 3) maximizing the dispersion of the measured 3D points within a required measurement volume. In addition, a set of design constraints were defined in order to ensure the feasibility of the resulting configuration, avoiding physical interference and occlusions, and keeping the overall system footprint within desired ranges.

9.1.2 Pattern Sequence Design Methodology for SL Systems

A novel design methodology was developed for determining the optimal pattern sequence that minimizes measurement errors in SL systems that use sinusoidal phase-shifting techniques. Based on the sequential unwrapping strategy of using a set of patterns with increasing number of fringes, the proposed methodology uniquely considers both the number of patterns that are needed in the

pattern sequence as well as the number of fringes for each pattern in order to reduce the reconstruction errors caused by random noise in the captured patterns.

9.1.3 Design Methodologies for Micro-Scale Measurements

Design methodologies for SL system using image focus fusion for micro-scale measurements were developed to effectively increase the depth-of-field of the microscope lenses. A novel calibration approach is also proposed which includes pattern sequence design, image fusion to get all-in-focus patterns and fitting and selection of calibration models for the entire measurement volume. This novel calibration approach provides the lowest predictive errors for a given calibration data set within the entire measurement volume for SL system using microscope lenses.

9.1.4 Implementation Experiments on SL System Configuration Design for Macro-Scale Measurements

The design methodology proposed in Chapter 3 was used to determine the optimal system configuration of an SL system. Experimental comparison of measurements between using the optimal and a feasible configurations validated that optimal system configuration provided more accurate 3D surface profiles of the certified object measured. A set of objects with different surface complexities was also measured and verified the capability of the designed SL system to handle complex surface profiles.

9.1.5 Implementation Experiments on Pattern Sequence Design for SL Systems for Macro-Scale Measurements

To experimentally validate the proposed methodology in Chapter 4, the optimal pattern sequence was obtained for an SL system. A certified metric object was measured, as well as a set of small complex objects, namely a gear, a propeller, and a scaled model of an engine block. Experimental results comparing the measurements obtained with the pattern sequence designed from the methodology and a frequently used approach demonstrate that the former minimized the random noise in measurement errors.

9.1.6 Implementation Experiments on Design Methodologies for Micro-Scale Measurements

The design methodologies presented in Chapters 3 and 4 were adapted for micro-scale measurements, and applied to a SL system using image focus fusion for measuring micro-scale

objects. A novel calibration approach was proposed for this system, which leverages robust regression methods and model selection metrics to obtain individual calibration models for each 3D component, with the lowest prediction errors for a given calibration data set. Such models were evaluated to be valid over the entire measurement volume, which was greater than the original volume limited by the sallow depth-of-field of the microscope lenses. Experiments conducted demonstrated the effectiveness of the proposed methodologies for designing SL systems for reconstructing the surface profile of a variety of micro-scale objects.

9.2 Future Work

The contributions made in this thesis provide several potential topics for future research. Future research could focus on using the SL models and the ray-tracing approach to determine the viewpoints required to measure the areas with occlusions and/or shadows. Such methodology could also be extended to determine the position of multiple number of cameras to provide more measurement points.

Regarding the pattern sequence, future work could focus on developing adaptive fringe patterns, i.e., pattern strategies that would be iteratively adapted to better measure the surface of the target object. In such an approach, after a minimal set of phase-shifted patterns is projected, the measured object profile would be used to design a new set of patterns that would maximize the measurement accuracy for that specific object. Another alternative in the area of pattern design is to investigate the use of frequency multiplexing to combine a set of fringe patterns into a single pattern for real-time applications measuring moving objects. This would increase the acquisition speed as the number of patterns is reduced.

Future work regarding SL system for micro-scale measurements could focus on alternative calibration models. For instance, the camera and the projector could be modelled separately so that the extensive calibration procedure could be modular and will not require a full recalibration if one of the hardware components is replace. Another option to evaluate is the feasibility of using a multi-variate regression model, i.e., one model that predicts simultaneously all the 3D coordinates for each pixel-to-pixel correspondence.

Appendix A
List of My Publications

Journal Publications

V. E. Marin, W. H. W. Chang, and G. Nejat, "Generic design methodology for the development of three-dimensional structured-light sensory systems for measuring complex objects," *Optical Engineering,* vol. 53, p. 112210, 2014.

V. E. Marin and G. Nejat, "Determining optimal pattern sequences for three-dimensional structured light sensory systems," *Applied Optics,* vol. 55, pp. 3203-3213, Apr 2016.

Conference Proceedings

V. Marin; W. Chang; E. Nuger & G. Nejat. "Design of a 3D sensing system for surface profiling of 3D parts in manufacturing applications," *CIRP sponsored International Conference on Virtual Machining Process Technology*, Montreal, QC, Canada, May, 2012.

V. Marin, W. Chang and G. Nejat, "A Methodology for Designing 3D Structured-Light Sensory Systems," *CIRP sponsored International Conference on Virtual Machining Process Technology*, Hamilton, ON, Canada, May 2013.

V. Marin, W. Chang and G. Nejat, "A Multi-Objective Design Methodology for 3D Structured-Light Sensors," *CIRP sponsored International Conference on Virtual Machining Process Technology*, Calgary, AB, Canada, May 2014.

V. Marin and G. Nejat, "Designing projection patterns for 3D structured-light sensors," *ASME International Design Engineering Technical Conferences and Computers and Information in Engineering Conference*, Boston, MA, USA, August 2015, paper DETC2005-47760.

References

1. Blais, F., *Review of 20 years of range sensor development.* Journal of Electronic Imaging, 2004. **13**(1): p. 231-243.

2. Sansoni, G., M. Trebeschi, and F. Docchio, *State-of-The-Art and Applications of 3D Imaging Sensors in Industry, Cultural Heritage, Medicine, and Criminal Investigation.* Sensors, 2009. **9**(1): p. 568-601.

3. Huang, P.S., C. Zhang, and F.-P. Chiang, *High-speed 3-D shape measurement based on digital fringe projection.* 2003. **42**(1): p. 163-168.

4. Xu, J., et al., *Rapid 3D surface profile measurement of industrial parts using two-level structured light patterns.* Optics and Lasers in Engineering, 2011. **49**(7): p. 907-914.

5. Sansoni, G. and F. Docchio, *Three-dimensional optical measurements and reverse engineering for automotive applications.* Robotics and Computer-Integrated Manufacturing, 2004. **20**(5): p. 359-367.

6. Yin, Z.Q., et al., *3D detection and reconstruction of worn parts for flexible remanufacture.* Advanced Materials Research, 2012. **468-471**: p. 83-86.

7. Caulier, Y., *Inspection of complex surfaces by means of structured light patterns.* Optics Express, 2010. **18**(7): p. 6642-6660.

8. Tsai, M.-J. and C.-C. Hung, *Development of a high-precision surface metrology system using structured light projection.* Measurement, 2005. **38**(3): p. 236-247.

9. Lin, C.-S., et al., *Measurement method of three-dimensional profiles of small lens with gratings projection and a flexible compensation system.* Expert Systems with Applications, 2011. **38**(5): p. 6232-6238.

10. Clancy, N.T., et al., *Spectrally encoded fiber-based structured lighting probe for intraoperative 3D imaging.* Biomedical Optics Express, 2011. **2**(11): p. 3119-3128.

11. Csaba, G., L. Somlyai, and Z. Vamossy. *Mobile robot navigation in unknown environment using structured light*. in *3rd IEEE International Symposium on Logistics and Industrial Informatics (LINDI)*. 2011. Budapest, Hungary.

12. Chen, L. and Y. Chang, *High accuracy confocal full-field 3-D surface profilometry for micro lenses using a digital fringe projection strategy.* Key Engineering Materials, 2008. **364-366**: p. 113-116.

13. Zhang, S. and P.S. Huang, *High-resolution, real-time three-dimensional shape measurement.* Optical Engineering, 2006. **45**(12): p. 123601.

14. May, S., et al., *Three-dimensional mapping with time-of-flight cameras.* Journal of Field Robotics, 2009. **26**(11-12): p. 934-965.

15. Samper, D., et al., *A stereo-vision system to automate the manufacture of a semitrailer chassis.* The International Journal of Advanced Manufacturing Technology, 2013. **67**(9-12): p. 2283-2292.

16. Son, S., H. Park, and K.H. Lee, *Automated laser scanning system for reverse engineering and inspection.* International Journal of Machine Tools and Manufacture, 2002. **42**(8): p. 889-897.

17. Salvi, J., et al., *A state of the art in structured light patterns for surface profilometry.* Pattern Recognition, 2010. **43**(8): p. 2666-2680.

18. Quan, C., et al., *Microscopic surface contouring by fringe projection method.* Optics & Laser Technology, 2002. **34**(7): p. 547-552.

19. Gühring, J. *Dense 3-D surface acquisition by structured light using off-the-shelf components*. in *Videometrics and Optical Methods for 3D Shape Measurement*. 2001. San Jose, CA, USA.

20. Nayar, S.K. and M. Gupta. *Diffuse structured light*. in *2012 IEEE International Conference on Computational Photography (ICCP)*. 2012. Seattle, WA, USA.

21. Liu, Y., P. Lehtonen, and X. Su, *High-accuracy measurement for small scale specular objects based on PMD with illuminated film.* Optics & Laser Technology, 2012. **44**(2): p. 459-462.

22. Vargas, J., et al., *Three-dimensional measurement of microchips using structured light techniques.* Optical Engineering, 2008. **47**(5): p. 053602.

23. Wiora, G. *High-resolution measurement of phase-shift amplitude and numeric object phase calculation*. in *Proc. SPIE 4117, Vision Geometry IX*. 2000.

24. Jia, X., et al., *Model and error analysis for coded structured light measurement system.* Optical Engineering, 2010. **49**(12): p. 123603.

25. Gun, K.W. and L.Y. Jeong, *Current Status and Research into Overcoming Limitations of Capsule Endoscopy.* Clinical Endoscopy, 2016. **49**(1): p. 8-15.

26. Neumann, P.P., et al., in *Proceedings of the 13th International Conference in Intelligent Autonomous Systems*, E. Menegatti, et al., Editors. 2016, Springer International Publishing. p. 1533-1548.

27. Karpinsky, N. and S. Zhang, *High-resolution, real-time 3D imaging with fringe analysis.* Journal of Real-Time Image Processing, 2012. **7**(1): p. 55-66.

28. Sansoni, G., et al., *Three-dimensional imaging based on Gray-code light projection: characterization of the measuring algorithm and development of a measuring system for industrial applications.* Applied Optics, 1997. **36**(19): p. 4463-4472.

29. Pages, J., J. Salvi, and J. Forest. *A new optimised De Bruijn coding strategy for structured light patterns*. in *Proceedings of the 17th International Conference on Pattern Recognition*. 2004.

30. Albitar, C., P. Graebling, and C. Doignon. *Design of a Monochromatic Pattern for a Robust Structured Light Coding*. in *IEEE International Conference on Image Processing*. 2007.

31. Pribanić, T., S. Mrvoš, and J. Salvi, *Efficient multiple phase shift patterns for dense 3D acquisition in structured light scanning.* Image and Vision Computing, 2010. **28**(8): p. 1255-1266.

32. Huang, P.S., S. Zhang, and F.P. Chiang, *Trapezoidal phase-shifting method for three-dimensional shape measurement.* Optical Engineering, 2005. **44**(12): p. 123601.

33. Tajima, J. and M. Iwakawa. *3-D data acquisition by Rainbow Range Finder*. in *10th International Conference on Pattern Recognition*. 1990. Atlantic City, NJ, USA.

34. Guo, L., X. Su, and J. Li, *Improved Fourier transform profilometry for the automatic measurement of 3D object shapes.* Optical Engineering, 1990. **29**(12): p. 1439-1444.

35. Chen, L.-C., H.-W. Ho, and X.-L. Nguyen, *Fourier transform profilometry (FTP) using an innovative band-pass filter for accurate 3-D surface reconstruction.* Optics and Lasers in Engineering, 2010. **48**(2): p. 182-190.

36. Legarda-Sáenz, R., T. Bothe, and W.P. Jüptner, *Accurate procedure for the calibration of a structured light system.* Optical Engineering, 2004. **43**(2): p. 464-471.

37. Sitnik, R., J. Woznicki, and M. Kujawinska, *Digital fringe projection system for large-volume 360-deg shape measurement.* Optical Engineering, 2002. **41**(2): p. 443-449.

38. Yang, Z. and Y.F. Wang, *Error analysis of 3D shape construction from structured lighting.* Pattern Recognition, 1996. **29**(2): p. 189-206.

39. Peng, T. and S.K. Gupta, *Model and Algorithms for Point Cloud Construction Using Digital Projection Patterns.* Journal of Computing and Information Science in Engineering, 2007. **7**(4): p. 372-381.

40. Peng, T., *Algorithms and models for 3D shape measurement using fringe projections*, in *Department of Mechanical Engineering*. 2006, University of Maryland: Maryland, D.C., U.S.A.

41. Gupta, M., et al., *A Practical Approach to 3D Scanning in the Presence of Interreflections, Subsurface Scattering and Defocus.* International Journal of Computer Vision, 2013. **102**(1-3): p. 33-55.

42. Zhang, S. and P.S. Huang, *Novel method for structured light system calibration.* Optical Engineering, 2006. **45**(8): p. 083601.

43. Mobedi, B. and G. Nejat, *3D Active Sensing in Time-Critical Urban Search and Rescue Missions.* IEEE/ASME Transactions on Mechatronics, 2012. **17**(6): p. 1111-1119.

44. Jia, X., G. Yue, and F. Mei, *The Mathematical Model and Applications of Coded Structured Light System for Object Detecting.* Journal of Computers, 2009. **4**(1): p. 53-60.

45. Wang, Y. and S. Zhang, *Optimal fringe angle selection for digital fringe projection technique.* Applied Optics, 2013. **52**(29): p. 7094-7098.

46. Zhang, C., H. Zhao, and L. Zhang, *Fringe order error in multifrequency fringe projection phase unwrapping: reason and correction.* Applied Optics, 2015. **54**(32): p. 9390-9399.

47. Zhang, S. *Digital multiple wavelength phase shifting algorithm*. in *Proc. SPIE 7432, Optical Inspection and Metrology for Non-Optics Industries*. 2009.

48. Huntley, J.M. and H.O. Saldner, *Shape measurement by temporal phase unwrapping: comparison of unwrapping algorithms.* Measurement Science and Technology, 1997. **8**(9): p. 986.

49. Zhang, S., *Phase unwrapping error reduction framework for a multiple-wavelength phase-shifting algorithm.* Optical Engineering, 2009. **48**(10): p. 105601.

50. Yalla, V.G. and L.G. Hassebrook. *Very high resolution 3D surface scanning using multi-frequency phase measuring profilometry*. in *Spaceborne Sensors II*. 2005. Orlando, FL, USA.

51. Li, J., L.G. Hassebrook, and C. Guan, *Optimized two-frequency phase-measuring-profilometry light-sensor temporal-noise sensitivity.* Journal of the Optical Society of America A, 2003. **20**(1): p. 106-115.

52. Wang, Y. and S. Zhang, *Novel phase-coding method for absolute phase retrieval.* Optics Letter, 2012. **37**(11): p. 2067-2069.

53. Zhang, S. and P.S. Huang, *Phase error compensation for a 3-D shape measurement system based on the phase-shifting method.* Optical Engineering, 2007. **46**(6): p. 063601.

54. Wang, Y., et al., *Maximum SNR pattern strategy for phase shifting methods in structured light illumination.* Journal of the Optical Society of America A, 2010. **27**(9): p. 1962-1971.

55. Liu, Y. and X. Su, *High precision phase measuring profilometry based on stereo microscope.* Optik - International Journal for Light and Electron Optics, 2014. **125**(19): p. 5861-5863.

56. Kettel, J., C. Müller, and H. Reinecke. *Three-dimensional reconstruction of specular reflecting technical surfaces using structured light microscopy*. in *Proc. SPIE 9276, Optical Metrology and Inspection for Industrial Applications III*. 2014.

57. Quan, C., et al., *Shape measurement of small objects using LCD fringe projection with phase shifting.* Optics Communications, 2001. **189**(1-3): p. 21-29.

58. Quan, C., et al., *Shape measurement by use of liquid-crystal display fringe projection with two-step phase shifting.* Applied Optics, 2003. **42**(13): p. 2329-2335.

59. Van der Jeught, S., J.A.M. Soons, and J.J.J. Dirckx, *Real-time microscopic phase-shifting profilometry.* Applied Optics, 2015. **54**(15): p. 4953-4959.

60. Yin, Y., et al., *Fringe projection 3D microscopy with the general imaging model.* Optics Express, 2015. **23**(5): p. 6846-6857.

61. Zhang, Z., *A flexible new technique for camera calibration.* IEEE Transactions on Pattern Analysis and Machine Intelligence, 2000. **22**(11): p. 1330-1334.

62. Li, B. and S. Zhang, *Flexible calibration method for microscopic structured light system using telecentric lens.* Optics Express, 2015. **23**(20): p. 25795-25803.

63. Chen, J., et al. *Microscopic fringe projection system and measuring method*. in *Eighth International Symposium on Precision Engineering Measurement and Instrumentation*. 2013.

64. Orghidan, R., et al., *Structured light self-calibration with vanishing points.* Machine vision and applications, 2014. **25**(2): p. 489-500.

65. Forsyth, D.A. and J. Ponce, *Computer Vision: A Modern Approach*. 2012: Prentice Hall Professional Technical Reference. 4-6.

66. Olague, G. and R. Mohr, *Optimal camera placement for accurate reconstruction.* Pattern Recognition, 2002. **35**(4): p. 927-944.

67. Bräuer-Burchardt, C. *Correcting lens distortion in 3D measuring systems using fringe projection*. in *Proc. SPIE 5962, Optical Design and Engineering II*. 2005.

68. Wu, X. and J. Kofman. *Lens distortion calibration by explicit straight-line to distorted-line geometric mapping*. in *Proc. SPIE 5603, Machine Vision and its Optomechatronic Applications*. 2004.

69. Ma, L., Y. Chen, and K.L. Moore, *Rational radial distortion models of camera lenses with analytical solution for distortion correction.* International Journal of Information Acquisition, 2004. **1**(02): p. 135-147.

70. Lenz, R.K. and R.Y. Tsai, *Techniques for calibration of the scale factor and image center for high accuracy 3-D machine vision metrology.* IEEE Transactions on Pattern Analysis and Machine Intelligence, 1988. **10**(5): p. 713-720.

71. Mao, X., W. Chen, and X. Su, *Improved Fourier-transform profilometry.* Applied Optics, 2007. **46**(5): p. 664-668.

72. Du, H. and Z. Wang, *Three-dimensional shape measurement with an arbitrarily arranged fringe projection profilometry system.* Optics Letter, 2007. **32**(16): p. 2438-2440.

73. Salvi, J., J. Pagès, and J. Batlle, *Pattern codification strategies in structured light systems.* Pattern Recognition, 2004. **37**(4): p. 827-849.

74. Marler, R.T. and J.S. Arora, *Survey of multi-objective optimization methods for engineering.* Structural and Multidisciplinary Optimization, 2004. **26**(6): p. 369-395.

75. Custódio, A.L., et al., *Direct Multisearch for Multiobjective Optimization.* SIAM Journal on Optimization, 2011. **21**(3): p. 1109-1140.

76. Dougherty, J., R. Kohavi, and M. Sahami. *Supervised and Unsupervised Discretization of Continuous Features*. in *Machine learning: Proceedings of the Twelfth International Conference*: Morgan Kaufmann.

77. Milligan, G. and M. Cooper, *An examination of procedures for determining the number of clusters in a data set.* Psychometrika, 1985. **50**(2): p. 159-179.

78. Halkidi, M., Y. Batistakis, and M. Vazirgiannis, *On Clustering Validation Techniques.* Journal of Intelligent Information Systems, 2001. **17**: p. 107-145.

79. Boissenin, M., et al., *Computer vision methods for optical microscopes.* Image and Vision Computing, 2007. **25**(7): p. 1107-1116.

80. Chang, W.-H., *Design, Development, and Calibration of a 3D Sensory System for Surface Profiling of 3D Micro-Scale Parts*, in *Mechanical and Industrial Engineering*. 2014, University of Toronto: Toronto, Canada.

81. Luitjens, P., *Automation and Calibration of a Micro Scale Structured Light System*, in *Mechanical and Industrial Engineering*. 2015, University of Toronto: Toronto, Canada.

82. Ray, S.F., *Applied Photographic Optics: Lenses and Optical Systems for Photography, Film, Video, Electronic and Digital Imaging*. 3rd ed. 2002: Focal Press.

83. Pertuz, S., et al., *Generation of All-in-Focus Images by Noise-Robust Selective Fusion of Limited Depth-of-Field Images.* IEEE Transactions on Image Processing, 2013. **22**(3): p. 1242-1251.

84. Wassermann, L., *All of Statistics. A Concise Course in Statistical Inference*. 2004: New York: Springer.

85. Montgomery, D.C., E.A. Peck, and G.G. Vining, *Introduction to Linear Regression Analysis*. 2001, New York, USA: John Wiley & Sons, Inc.

86. Street, J.O., R.J. Carroll, and D. Ruppert, *A note on computing robust regression estimates via iteratively reweighted least squares.* The American Statistician, 1988. **42**(2): p. 152-154.

87. Alpaydin, E., *Introduction to machine learning*. 2014: MIT press.

88. Bell, T. and S. Zhang, *Toward superfast three-dimensional optical metrology with digital micromirror device platforms.* Optical Engineering, 2014. **53**(11): p. 112206.

89. Edmund Optics, Inc. *25 x 25mm, 0.125mm Spacing, Opal Distortion Target*. 2014. Retrieved from: http://www.edmundoptics.com/test-targets/distortion-test-targets/fixed-frequency-grid-distortion-targets/59209/.

90. Atherton, T.J. and D.J. Kerbyson, *Size invariant circle detection.* Image and Vision Computing, 1999. **17**(11): p. 795-803.